

EFFICIENT NUMERICAL ANALYSIS AND DESIGN OF REFLECTARRAY
ANTENNAS

A THESIS SUBMITTED TO
THE GRADUATE SCHOOL OF NATURAL AND APPLIED SCIENCES
OF
MIDDLE EAST TECHNICAL UNIVERSITY

BY
ERDİNÇ ERÇİL

IN PARTIAL FULFILLMENT OF THE REQUIREMENTS
FOR
THE DEGREE OF DOCTOR OF PHILOSOPHY
IN
ELECTRICAL AND ELECTRONICS ENGINEERING

JANUARY 2015

Approval of the Thesis:

**EFFICIENT NUMERICAL ANALYSIS AND DESIGN OF REFLECTARRAY
ANTENNAS**

submitted by **ERDİNÇ ERÇİL** in partial fulfillment of the requirements for the degree of **Doctor of Philosophy in Electrical and Electronics Engineering Department, Middle East Technical University** by,

Prof. Dr. Gülbin Dural Ünver _____
Dean, Graduate School of **Natural and Applied Sciences**

Prof. Dr. Gönül Turhan Sayan _____
Head of Department, **Electrical and Electronics Engineering**

Prof. Dr. Özlem Aydın Çivi _____
Supervisor, **Electrical and Electronics Engineering Dept., METU**

Assoc. Prof. Lale Alatan _____
Co-supervisor, **Electrical and Electronics Engineering Dept., METU**

Examining Committee Members:

Prof. Dr. Mustafa Kuzuoğlu _____
Electrical and Electronics Engineering Dept., METU

Prof. Dr. Özlem Aydın Çivi _____
Electrical and Electronics Engineering Dept., METU

Prof. Dr. Seyit Sencer Koç _____
Electrical and Electronics Engineering Dept., METU

Assoc. Prof. Vakur Ertürk _____
Electrical and Electronics Engineering Dept., Bilkent University

Assoc. Prof. Özgür Salih Ergül _____
Electrical and Electronics Engineering Dept., METU

Date: 26.01.2015

I hereby declare that all information in this document has been obtained and presented in accordance with academic rules and ethical conduct. I also declare that, as required by these rules and conduct, I have fully cited and referenced all material and results that are not original to this work.

Name, Last name: Erdiñ ERÇİL

Signature :

ABSTRACT

EFFICIENT NUMERICAL ANALYSIS AND DESIGN OF REFLECTARRAY ANTENNAS

Erçil, Erdinç

PhD., Department of Electrical and Electronics Engineering
Supervisor: Prof. Dr. Özlem Aydın Çivi
Co-Supervisor: Assoc. Prof. Lale Alatan

January 2015, 136 pages

The accurate numerical analysis of electrically large reflectarray antennas has been a challenging task since their advent because it becomes impractical to employ the generalized numerical electromagnetic tools for their numerical analysis. Therefore the classical approach is to resort to approximate methods. However, approximate methods trade off accuracy against memory and speed. In this thesis study; an approximate analysis technique is established such that it is more accurate than the present approximate analysis techniques and more efficient than the full wave analysis schemes in terms of memory requirement and speed. The technique relies on using characteristic modes as macro basis functions and reusing the dominant characteristic mode of the resonant element for all elements in the reflectarray. This utilization leads to obtaining a reduced matrix system where the number of unknowns is drastically decreased. As far as the far field is concerned, accurate results even with a single characteristic mode are achieved. The accuracy is attained owing to preservation of mutual coupling information via the original MoM impedance matrix. The solution is further accelerated by tabulating the entries of the reduced matrix as a function of interacting patch sizes and their relative displacements. It is observed that for sufficiently separated patches, the reduced matrix entry is almost a separable function of the two dimensional displacement

between patches and patch sizes associated with the matrix entry. Tabulation is efficiently performed by exploiting this fact. Achieved acceleration is sufficient to use this analysis method in the design of reflectarrays. For a 1000 element array, the tabulation process takes 28 min on a platform with 3.3 GHz CPU clock speed. With the lookup table at hand, the solution time, which is important for the design iterations, is 0.38 seconds. The speed provided by the method makes it possible to employ gradient based optimization algorithms such as Steepest Descent or Conjugate Gradient Method, both of which are successfully applied to two design problems in the scope of the study.

Keywords: Reflectarray antenna, efficient numerical solution, characteristic modes, method of moments, optimization.

ÖZ

YANSITMALI DİZİ ANTENLERİN VERİMLİ NÜMERİK ANALİZ VE TASARIMI

Erçil, Erdiç

Doktora, Elektrik ve Elektronik Mühendisliği Bölümü

Tez Yöneticisi: Prof. Dr. Özlem Aydın Çivi

Ortak Tez Yöneticisi: Doç. Dr. Lale Alatan

Ocak 2015, 136 sayfa

Elektriksel olarak büyük yansıtmalı dizi antenlerin yüksek doğruluk ile analiz edilmeleri bu tip antenlerin ortaya çıkmasından itibaren zor bir iş olmuştur. Çünkü elektriksel olarak büyük yansıtmalı dizilerin analizi için genel hesaplamalı elektromanyetik tekniklerinin kullanımı pratik olmamaktadır. Bu nedenle klasik yaklaşım, yaklaşık yöntemlere başvurmaktır. Ancak mevcut yaklaşık yöntemler ancak doğruluktan ödün vermek suretiyle hız ve hafıza gereksinimi açısından avantaj sağlamaktadır. Bu tez çalışmasında, var olan yaklaşık yöntemlerden daha yüksek doğruluk sunan ancak çözüm hızı ve hafıza ihtiyacı açısından tam dalga tekniklerden çok daha verimli olan bir yaklaşık analiz tekniği geliştirilmiştir. Geliştirilen teknik, karakteristik modların makro taban fonksiyonu olarak kullanımına ve resonant elemanın baskın karakteristik modunun dizideki tüm elemanlar için yeniden kullanılabilirliğine dayanmaktadır. Bu yaklaşım, bilinmeyen sayısının önemli ölçüde azaltıldığı küçültülmüş bir matris denklemine ulaşmayı sağlamaktadır. Dizinin uzak alanı dikkate alındığında, sadece tek bir karakteristik modun bile oldukça doğru sonuçlar verdiği görülmüştür. Bu doğruluğun kaynağı, original MoM matrisindeki elemanlar arası etkileşim bilgisinin korunmasıdır. Çözüm süresi; küçültülmüş matrisin terimlerini, etkileşen elemanların boyutları ve iki boyutlu deplasmanlarına bağlı bir fonksiyon olarak tablollaştırarak daha da azaltılmıştır. Yeterince uzak iki

eleman için ilgili matris teriminin, elemanların boyutlarının ve deplasmanlarının hemen hemen ayrılabilir bir fonksiyonu olduğu görülmüştür. Tablolaştırma, bu durum sayesinde verimli bir şekilde yapılabilmektedir. Elde edilen hızlanma, bu analiz tekniğini tasarımda kullanmak için yeterli düzeydedir. 3.3 GHz saat hızı ile çalışan bir bilgisayar üzerinde, 1000 elemanlı bir dizi için tablolaştırma 28 dakika sürmektedir. Tablolar mevcut iken, tasarım döngüleri için esas önem taşıyan çözüm süresi 0.38 saniye olmaktadır. Yöntemin sağladığı hız, En Hızlı Düşüş ve Konjuge Gradyen gibi optimizasyon algoritmalarını uygulamayı olanaklı hale getirmektedir ve bu sayede her iki optimizasyon yöntemi tez kapsamında uygulanabilmiştir.

Anahtar kelimeler: Yansıtılmalı dizi anten, verimli nümerik çözüm, karakteristik modlar, momentler metodu, optimizasyon.

To my beloved wife

ACKNOWLEDGMENTS

The author would like to express his sincere appreciation to his supervisor, Prof. Dr. Özlem Aydın Çivi and co-supervisor Assoc. Prof. Lale Alatan for their support, guidance, confidence and friendly encouragement.

The author is grateful to Prof. Dr. Sencer Koç and Assoc Prof. Vakur Ertürk for their guidance and advices throughout the thesis monitoring period.

The author wishes to thank to Dr. Aytaç Alparslan and Dr. Pınar Karabulut Toker for granting the MATLAB code for Spatial Green's Function calculation.

The author would like to acknowledge his gratitude to his friends and colleagues Mr. Mehmet Erim İnal, Mr. Akın Dalkılıç, Mr. Egemen Yıldırım and Dr. Can Barış Top for their friendly support. The author appreciates Mr. Doğanay Doğan's and Dr. Alper Kürşat Öztürk's technical assistance and fruitful discussions. Mr. Sinan Köksoy's help on vocabulary and grammar is also appreciated.

The author would like to thank "Department of Science Fellowships and Grant Programs" of The Scientific and Technological Research Council of Turkey (TUBITAK) for supporting this work financially.

The author would like to express his deepest gratitude to his parents and his siblings.

Finally, the author feels grateful to his wife Işıl for her infinite patience and understanding. Without her support and tolerance, this work would never end up successful.

TABLE OF CONTENTS

ABSTRACT.....	v
ÖZ.....	vii
ACKNOWLEDGMENTS	x
TABLE OF CONTENTS.....	xi
LIST OF TABLES	xiv
LIST OF FIGURES	xv
LIST OF ABBREVIATIONS	xxi
CHAPTERS	
1 INTRODUCTION	1
1.1 Motivation	9
1.2 Original Contributions of the Study	10
1.3 Organization of the Thesis	12
2 DEVELOPMENT OF THE EFFICIENT COMPUTATION METHOD	15
2.1 MoM Analysis Approach for Reflectarrays	16
2.1.1 The Mixed Potential Formulation	18
2.1.2 Application of Method of Moments.....	19
2.1.3 Validation of MATLAB Codes.....	31
2.2 Characteristic Modes and Reusability of Characteristic Modes	32
2.2.1 Characteristic Mode Concept.....	32
2.2.2 Characteristic Modes as Macro Basis Functions	37
2.3 An Efficient Method to Construct the Reduced Matrix	54
2.3.1 Investigations on Discarding Distant Interactions	54

2.3.2	Tabulation of Reduced Matrix Entries	58
2.3.3	Computational Load	63
2.3.4	A Large Reflectarray Problem Solved by Proposed Method	67
2.3.5	Extension to Two Independent CMs	70
3	APPLICATION OF THE FAST ANALYSIS METHOD FOR VARIOUS ELEMENT TYPES	75
3.1	Square Patch with Outer Ring	75
3.1.1	Reusability of CMs	77
3.1.2	Separability	81
3.2	Reflectarray Element for Rotational Phase Variation Technique	83
3.2.1	Reusability of CMs	87
3.2.2	Separability	89
3.3	Conclusions	93
4	UTILIZATION OF THE EFFICIENT ANALYSIS METHOD IN DESIGN PROBLEMS	95
4.1	Preliminary Computations	98
4.1.1	Incident Field at Element Centers	98
4.1.2	The Far Field Due To Ground Scattering	99
4.1.3	The Far Field Patterns of Candidate Elements	101
4.2	Reflectarray Design as an Optimization Problem	103
4.2.1	Newton Minimization	107
4.2.2	The Method of Steepest Descent	108
4.2.3	The Conjugate Gradient Method	108
4.2.4	Application of the Optimization Methods to Reflectarray Design	109
4.3	Verification of the Designs	120
4.3.1	Separable Pattern	120

4.3.2	Non-Separable Pattern	121
4.4	Conclusions	123
5	CONCLUSIONS.....	125
	REFERENCES.....	129
	CURRICULUM VITAE	134

LIST OF TABLES

Table 2-1 Coordinates and weights of quadrature points in simplex coordinates.	26
Table 2-2 Explanations of variables for computation of singular integrals	27
Table 2-3 Properties of RWG data structure.	30
Table 2-4 Electric and magnetic field expressions for first and second type incidences.	44
Table 2-5 Computation times of tabulations for 1000 element array.	65
Table 2-6 Computation times spent for reflectarrays with different number of elements.....	66
Table 3-1 The coordinates of the points of interest in Figure 3-21.....	91
Table 4-1 Definition of variables in (4-10).	105

LIST OF FIGURES

Figure 1-1 A generic reflectarray.....	2
Figure 1-2 Infinite Array Approach.....	6
Figure 1-3 Typical phase design curve of the infinite array approach.....	6
Figure 1-4 Mask pattern of reflectarray to be used as sub-reflector [20].....	7
Figure 1-5 A photo of a reflectarray [21].....	7
Figure 1-6 Isolated Element Approach.....	8
Figure 1-7 Surrounded Element Approach.....	8
Figure 2-1 Reflectarray problem: a) Problem definition, b) Fields in absence of patch, c) fields scattered by patch.....	18
Figure 2-2 Explanation of parameters in (2-7).....	20
Figure 2-3 Basic triangle in simplex coordinates.....	25
Figure 2-4 Geometry for computation of singular integrals.....	27
Figure 2-5 An example of a structured mesh.....	29
Figure 2-6 An example of an unstructured mesh.....	30
Figure 2-7 Comparison of patterns for the reflectarray designed for sectoral beam.....	31
Figure 2-8 Comparison of patterns for the reflectarray designed for scanned beam.....	32
Figure 2-9 Mesh used for the rectangular patch.....	34
Figure 2-10 Modal significance of characteristic modes.....	35
Figure 2-11 First three characteristic modes for the rectangular patch.....	35
Figure 2-12 Fourth most significant mode for the rectangular patch.....	36
Figure 2-13 The first two significant modes for the square patch.....	36
Figure 2-14 Characteristic modes for circle, triangle, bow tie and star [32], horizontal modes left, vertical modes right.....	37
Figure 2-15 Mesh scaling.....	40
Figure 2-16 An illustration to define the reflectarray geometry.....	42
Figure 2-17 Layout of the reflectarray under concern.....	42
Figure 2-18 Desired and synthesized patterns.....	43
Figure 2-19 Definition of the first and the second type incidences.....	43

Figure 2-20 Error in current w.r.t. number of modes and incidence angle for 1 st type incidence.....	45
Figure 2-21 Error in current w.r.t. number of modes and incidence angle for 2 nd type incidence.....	45
Figure 2-22 Comparison of the amplitude of far fields at $\varphi=0$, computed by 1 and 10 characteristic modes (35 degrees, 1 st type incidence, φ polarization).	46
Figure 2-23 Comparison of the amplitude of far fields at $\varphi=90$, computed by 1 and 10 characteristic modes (35 degrees, 2 nd type incidence, θ polarization).	47
Figure 2-24 Comparison of the phase of far fields at $\varphi=0$, computed by 1 and 10 characteristic modes (35 degrees, 1 st type incidence, φ polarization).	47
Figure 2-25 Comparison of the phase of far fields at $\varphi=90$, computed by 1 and 10 characteristic modes (35 degrees, 2 nd type incidence, θ polarization).	48
Figure 2-26 Variation of error in current w.r.t. reference patch size and incidence angle (1 st type incidence).....	49
Figure 2-27 Variation of error in current w.r.t. reference patch size and incidence angle (2 nd type incidence).....	50
Figure 2-28 Real and imaginary parts of the input impedance of isolated patch.....	50
Figure 2-29 Variation of error in current w.r.t. incidence angle when the dominant mode of resonant patch is used as an MBF for all patches.	51
Figure 2-30 Comparison of far fields obtained by conventional MoM and reduced matrix solution with same CM for all patches (1 st type incidence, φ polarization)...	51
Figure 2-31 Comparison of far fields obtained by conventional MoM and reduced matrix solution with same CM for all patches (2 nd type incidence, θ polarization). ..	52
Figure 2-32 Comparison of the far fields of the reflectarray antenna computed by conventional MoM and proposed method, $\varphi = 0^\circ$ plane, φ polarization.	53
Figure 2-33 Comparison of the far fields of the reflectarray antenna computed by conventional MoM and proposed method, $\varphi = 90^\circ$ plane, θ polarization.....	53
Figure 2-34 Log magnitude of 90th row of reduced matrix, properly arranged according to geometric positions of corresponding patches.	55
Figure 2-35 Explanation of different neighborhood types.	56
Figure 2-36 Effect of ignoring distant interactions on amplitude of β	56
Figure 2-37 Effect of ignoring distant interactions on phase of β	57

Figure 2-38 Effect of ignoring distant interactions on the far field of reflectarray, $\varphi = 0^\circ$ plane.	57
Figure 2-39 Definition of variables in (2-53).....	59
Figure 2-40 Amplitude of function f at various instances of m and n (a): $m=4, n=5$, (b): $m=2, n=9$, (c): $m=3, n=7$, (d): $m=5, n=2$	60
Figure 2-41 Phase (degrees) of function f at various instances of m and n (a): $m=4, n=5$, (b): $m=2, n=9$, (c): $m=3, n=7$, (d): $m=5, n=2$	60
Figure 2-42 Amplitude of function f at various instances of s_i and s_j (a): $s_i=9\text{mm}$, $s_j=3\text{mm}$, (b): $s_i=8\text{mm}$, $s_j=12\text{mm}$, (c): $s_i=6\text{mm}$, $s_j=14\text{mm}$, (d): $s_i=10\text{mm}$, $s_j=10\text{mm}$	61
Figure 2-43 Phase (degrees, unwrapped) of function f at various instances of s_i and s_j (a): $s_i=9\text{mm}$, $s_j=3\text{mm}$, (b): $s_i=8\text{mm}$, $s_j=12\text{mm}$, (c): $s_i=6\text{mm}$, $s_j=14\text{mm}$, (d): $s_i=10\text{mm}$, $s_j=10\text{mm}$	62
Figure 2-44 Phase and amplitude characteristic of $J1TZ11J1$ w.r.t. patch size.	64
Figure 2-45 30×30 reflectarray.....	68
Figure 2-46 Azimuth pattern ($\varphi = 0^\circ$) of the 30×30 reflectarray computed by HFSS and the proposed method.	68
Figure 2-47 Elevation pattern ($\varphi = 90^\circ$) of the 30×30 reflectarray computed by HFSS and the proposed method.....	69
Figure 2-48 Azimuth pattern ($\varphi = 0^\circ$) of the 30×30 reflectarray computed by HFSS and the two infinite array approaches.	70
Figure 2-49 Elevation pattern ($\varphi = 90^\circ$) of the 30×30 reflectarray computed by HFSS and the two infinite array approaches.....	70
Figure 2-50 Amplitude of terms in Z_{ij} (a): $J1TZ_{ij}J1$, (b): $J1TZ_{ij}J2$, (c): $J2TZ_{ij}J1$, (d): $J2TZ_{ij}J2$	72
Figure 2-51 Amplitude of the 179 th column of the 320×320 Z matrix.	73
Figure 2-52 Amplitude of the 180 th column of the 320×320 Z matrix.	74
Figure 3-1 Square patch with outer ring [45].....	76
Figure 3-2 The phase characteristic of the proposed element with respect to $L1$ and frequency [45].	76
Figure 3-3 Dominant characteristic mode of the square ring.....	77
Figure 3-4 Experimental reflectarray with varying sized wideband elements.....	79

Figure 3-5 Variation of error in current with incidence angle when CMs for the separate metallizations of the wideband patch.	80
Figure 3-6 Comparison of the amplitude of the φ polarized far fields at $\varphi=0^\circ$, computed by Conventional MoM and using fundamental characteristic modes of separate metallizations (40 degrees, 1 st type incidence).	80
Figure 3-7 Comparison of the amplitude of the θ polarized far fields at $\varphi=90^\circ$, computed by Conventional MoM and using fundamental characteristic modes of separate metallizations (20 degrees, 2 nd type incidence).	81
Figure 3-8 Amplitudes of reduced matrix entries for $d_x=40$ mm, $d_y=100$ mm, (a): $J1TZijJ1$, (b): $J1TZijJ2$, (c): $J2TZijJ2$	82
Figure 3-9 Amplitudes of reduced matrix entries for $d_x=80$ mm, $d_y=40$ mm, (a): $J1TZijJ1$, (b): $J1TZijJ2$, (c): $J2TZijJ2$	82
Figure 3-10 Amplitudes of reduced matrix entries for $L_1=8$ mm for source element and $L_1=8$ mm for observation element, (a): $J1TZijJ1$, (b): $J1TZijJ2$, (c): $J2TZijJ2$	82
Figure 3-11 Amplitudes of reduced matrix entries for $L_1=4$ mm for source element and $L_1=4$ mm for observation element, (a): $J1TZijJ1$, (b): $J1TZijJ2$, (c): $J2TZijJ2$	83
Figure 3-12 Split – ring resonator.	84
Figure 3-13 Parameters of the split – ring resonator.	85
Figure 3-14 Phase of the right hand circular polarized component of the reflected field for the split ring resonator.	86
Figure 3-15 Magnitude of the right hand and left hand circularly polarized components of the reflected field for the split ring resonator.	86
Figure 3-16 Variation of error in current with incidence angle (single mode).	87
Figure 3-17 Variation of error in current with incidence angle (4 modes).	88
Figure 3-18 Amplitude of x polarized E field on the H plane.	88
Figure 3-19 Amplitude of y polarized E field on the H plane.	89
Figure 3-20 Parameters that influence the reduced matrix entries.	90
Figure 3-21 Representative picture showing the available tabulations and useful points in approximating the reduced matrix term for an arbitrary $(R1, \theta1, \gamma1)$	91
Figure 3-22 Amplitude of $J1TZijJ1$ for $R=10.8$ mm, (a): Calculated by the actual impedance matrix Zij , (b): Approximated by (3-8).	92

Figure 3-23 Amplitude of $J3TZijJ4$ for $R=10.8$ mm, (a): Calculated by the actual impedance matrix Zij , (b): Approximated by (3-8).....	93
Figure 4-1 Radiation boundary around the feed antenna.....	96
Figure 4-2 Amplitude of y polarized E field on a 540 mm long line, 360 mm away from the feed antenna.....	97
Figure 4-3 Phase of y polarized E field on a 540 mm long line, 360 mm away from the feed antenna.....	97
Figure 4-4 Equivalent electric and magnetic currents.....	99
Figure 4-5 Log amplitude of the φ polarized electric field at $R=10^4$ m, at $\varphi = 0^\circ$.	100
Figure 4-6 Phase of the φ polarized electric field at $R=10^4$ m, at $\varphi = 0^\circ$	100
Figure 4-7 Comparisons of the normalized far field patterns of 17 mm patch and 2 mm patch, each carrying the dominant mode current, $J1$. Observation plane: $\varphi = 0^\circ$, polarization: φ	102
Figure 4-8 Azimuth-over-elevation grid.....	103
Figure 4-9 Desired azimuth pattern and the azimuth far field result of the design made by infinite array approach.....	113
Figure 4-10 Desired elevation pattern and the elevation far field result of the design made by infinite array approach.....	113
Figure 4-11 Desired azimuth pattern and the azimuth far field result of the design after steepest descent optimization with line search.....	114
Figure 4-12 Desired elevation pattern and the elevation far field result of the design after steepest descent optimization with line search.....	114
Figure 4-13 Variation of cost function with iterations, normalized to initial cost function.....	115
Figure 4-14 3-dimensional view of the optimized reflectarray pattern.....	115
Figure 4-15 Difference of optimized and initial patch sizes in mm.....	116
Figure 4-16 Variation of cost function with iterations, normalized to initial cost function.....	117
Figure 4-17 Variation of cost function with iterations, normalized to initial cost function.....	117
Figure 4-18 Desired pattern for the non-separable pattern synthesis.....	118

Figure 4-19 Variation of cost function with iterations, normalized to initial cost function.....	119
Figure 4-20 Optimized pattern after 100 iterations.....	119
Figure 4-21 Comparison of the HFSS solution with the pattern synthesized during optimization in H plane.....	120
Figure 4-22 Comparison of the HFSS solution with the pattern synthesized during optimization in E plane.....	121
Figure 4-23 HFSS result of the reflectarray optimized to yield the non-separable pattern.....	122
Figure 4-24 Comparison of the HFSS solution with the pattern synthesized during optimization in H plane.....	122
Figure 4-25 Comparison of the HFSS solution with the pattern synthesized during optimization in E plane.....	123

LIST OF ABBREVIATIONS

AIM:	Adaptive Integral Method
ACA:	Adaptive Cross Approximation
CM:	Characteristic Mode
CBFM:	Characteristic Basis Function Method
CPU:	Central Processing Unit
FDTD:	Finite Difference Time Domain
FEM:	Finite Element Method
HFSS:	High Frequency Structure Simulator
LHCP:	Left Hand Circular Polarization
MBF:	Macro Basis Function
MDA:	Matrix Decomposition Algorithm
MEMS:	Micro Electro Mechanical Switch
MLFMA:	Multilevel Fast Multipole Algorithm
MoM:	Method of Moments
MPIE:	Mixed Potential Integral Equation
PCB:	Printed Circuit Board
PEC:	Perfect Electric Conductor
RHCP:	Right Hand Circular Polarization
RWG:	Rao-Wilton-Glisson
SFX:	Synthetic Functions Expansion
SM-AIM:	Sparse Matrix Adaptive Integral Methods

CHAPTER 1

INTRODUCTION

Reflectarray antennas are structures similar to reflectors with regard to their radiation mechanism. They are composed of a feed antenna and a planar printed circuit board with discrete antenna elements etched on (Figure 1-1). The feed antenna illuminates the antenna elements and the antenna elements are usually arranged to reflect the incident field such that the aperture plane is an equi-phase surface. Reflectarrays are preferred in many applications where lightweight is required and the disadvantages associated with conventional reflector antennas need to be avoided. These disadvantages are mainly cost, requirement of surface smoothness in manufacturing process; and the volume occupied. On the other hand, the reflectarray is manufactured by one or more dielectric substrates [1] and is usually of planar geometry. Similar to reflector antennas, the reflectarrays are illuminated by a small feed antenna. The desired far field pattern is realized by adjusting the aperture field distribution via configuring the reflection coefficient of the antenna elements. As an advantage over the reflector antenna, beamshaping with a reflectarray can be done using relatively simple and well defined array antenna techniques while for conventional reflector antennas it requires shaping of the surface, which is not as easy in terms of design and manufacturing. Furthermore, some reflectarrays have the capability of reconfigurability, which enables steering or re-shaping the beam electronically. Owing to the infrastructure for reconfigurability, the manufacturing tolerances are also relaxed. Yet, the reflectarrays are not advantageous for all aspects. For instance, reflectarrays present limited bandwidth for two main reasons: The array elements are usually narrowband and the planar structure of the reflectarray prevents having frequency independent collimation of the rays emanating from the feed [2], as opposed to the case with a parabolic reflector. Usually, the element geometries or terminations are optimized to yield a desired aperture phase distribution at a specific frequency. As the frequency is varied, the field distribution over the array aperture

diverges from the desired aperture field distribution because of the change in reflection coefficient of the elements and the electrical distance between the feed antenna and elements. On the other hand, techniques exist to enhance the bandwidth of reflectarray antennas. Using thick dielectrics or stacking up two or more layers of dielectric and metallization are proven to be useful for enhancement of the bandwidth of the element [3]. A straightforward solution to the electrical distance problem is to load the elements with true time delay stubs, but these stubs are often required to provide many multiples of wavelength delay and therefore become very long. Another possible solution is to compromise on the fully planar geometry and mimic the shape of a parabolic reflector with a number of flat panels [4] in order to reduce the frequency sensitivity of the total electrical distance traversed by the rays from the feed to the reflectarray aperture plane.

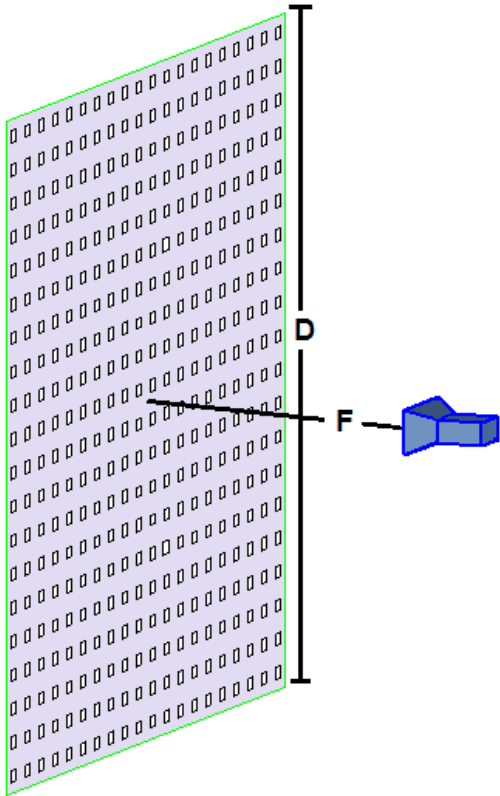


Figure 1-1 A generic reflectarray.

Reflectarrays could be categorized into two as reconfigurable and non-reconfigurable ones. Reconfigurable reflectarrays have a means of electronically controlled phase shifting mechanism at each element to achieve the phase requirements of different beams that might be demanded from the antenna. Varactor diodes are employed as

reactive elements in [5]. Another technique to achieve reconfigurability is to use MEMS phase shifters [6], [7]. In reconfigurable reflectarrays, element geometry is fixed throughout the array and this uniformity is in favor of assuming periodic boundary conditions for element analysis. On the other hand, non-reconfigurable reflectarrays are more affordable because they do not bear any electronic control. However, their downside is serving with a fixed radiation pattern. The pattern is realized by arranging the reflection response of the elements with various techniques. Most common techniques are; terminating the elements with different length stubs [8], using different size elements [9], and rotating the element [10]. Stub loading has the disadvantage of increased cross-polarization level due to orienting the stub orthogonal to the current direction over the patch because of layout concerns. Reflectarrays realized by element rotation are limited to circular polarized radiation [10].

This dissertation mainly focuses on the accurate and efficient analysis of reflectarrays with variable element sizes. This reflectarray type is preferred in practice due to ease in manufacturing and low cross polarization level when compared to the stub loaded reflectarrays [9]. The work on this type of reflectarrays in the literature is basically focused on their analysis and design. Accurate analysis of reflectarrays can be obtained through the use of numerical techniques like Method of Moments (MoM), Finite Element Method (FEM) and Finite Difference Time Domain Method (FDTD). Even large reflectarrays can be analyzed both accurately and efficiently by combining MoM with fast algorithms such as Multi-level Fast Multipole Algorithm (MLFMA) [12], Adaptive Integral Method (AIM) [12], Matrix Decomposition Algorithm (MDA) [13] or Adaptive Cross Approximation (ACA) [14]. Specifically, in [15], full wave solution of large reflectarrays is considered by utilizing Synthetic Functions Expansion (SFX) [16] and Sparse Matrix Adaptive Integral Methods (SM-AIM) [17]. SM-AIM method is reported to use 290 Mbytes RAM and 4 minutes of CPU time for the solution of a 20×20 reflectarray antenna while SFX requires 300 Mbytes and 29 minutes. In [18], fast analysis of reflectarrays is accomplished via combining MLFMA and CBFM. A reflectarray with dimensions of $16\lambda_0$ by $16\lambda_0$ is reported to be analyzed in approximately 20 minutes by using an

i7 quad core processor and 6 Gbytes RAM. However, due to large number of design parameters and the electrical size of the reflectarray problem, none of the above listed analysis techniques can practically lead the designer to a successful design when no a priori knowledge on element parameters is available. When the design of reflectarrays is considered, a link between the size (or the orientation) of the elements and the phase of the associated reflection coefficient is required to be able to choose the appropriate element geometry that will generate the desired far field pattern. This link can be approximately provided by the infinite array approach [9] (also referred as local periodicity approach) or alternatively, the isolated element approach [22]. In infinite array approach, each element in the array is assumed to be within an infinite array of its duplicates (Figure 1-2). This assumption allows establishing the relation between the size of the element and the phase of the reflection coefficient by analyzing unit cells with various element sizes. The size of each element is chosen from a phase design curve, (an example of which is given in Figure 1-3) such that each element reflects the incident field with the phase mandated by the array pattern synthesis procedure. Since this method assumes local periodicity, it bears approximate information regarding the actual mutual coupling among the elements. The method is approximate in two aspects. First, the elements near the edges and corners, whose neighbors are either missing or very few on one or more sides, are also assumed to be within a periodic environment. Second, the geometry variation is not always smooth due to aperture phase requirements of the desired antenna pattern. In [19], it is stated that the accuracy of the local periodicity approach relies on smooth variation of the size of the array elements. However, the realization of reflectarrays with arbitrarily shaped beams or reflectarrays that serve as sub-reflectors of multiple reflector systems [20], [21] might necessitate rapid change of phase and therefore element dimensions over the array aperture. Even for reflectarrays that radiate a pencil beam, due to limited phase span provided by the variations in element geometry, there exist sudden transitions from a small element to a large element corresponding to periods of 360 degrees as seen in Figure 1-4 and Figure 1-5. Furthermore, many practical reflectarrays are not large enough to ignore the effect of edge elements. Thus, in many occasions it becomes necessary to fine-tune the geometry of elements through iterative use of an accurate numerical analysis

method, which is a computationally expensive task. Actually, this may not be practical for large reflectarrays with the existing computational technology.

The isolated element approach, as opposed to the infinite array approach, neglects the mutual coupling and considers each element in the array as an isolated one (Figure 1-6). This approach is divided into two sub-approaches. In the first one, the phase of the reflected field is used [22] and it is assumed that its amplitude does not depend on the element geometry. In the second one, the dependence of the amplitude of the reflected field on the element geometry is also taken into account [23]. These approaches are successful when the coupling between elements is actually small enough to be neglected. Nevertheless, this condition is not general and therefore these approaches are no better than the infinite array approach in terms of far field accuracy.

In summary, none of the above three approaches can truly model the mutual coupling in the actual array. These approaches of course do not claim to perfectly predict the eventual pattern, but it is clear that the element dimensions must be tweaked and full wave simulation at each tweaking step is necessary. Changing the size of a single element influences current distribution not only on the element under concern, but on many surrounding elements as well. Therefore there is not a simple way of choosing the best increment (or decrement) in element size when fine-tuning the reflectarray.

To overcome the shortcomings of the local periodicity approach and to make a more accurate analysis, the surrounded element approach is proposed in [24]. In this approach, a virtual sub-array is formed by considering an element and a few of its surrounding neighbor elements (Figure 1-7). This sub-array is analyzed through the use of full wave analysis methods and this procedure is repeated for all elements in the array. As a result, the solution of a large sized problem (full array) is decomposed into the repeated solution of smaller sized problems (sub-arrays). This approximate analysis approach cannot be utilized to guide the design of reflectarrays, since the characterization of an element requires the size information of the neighboring elements as well.

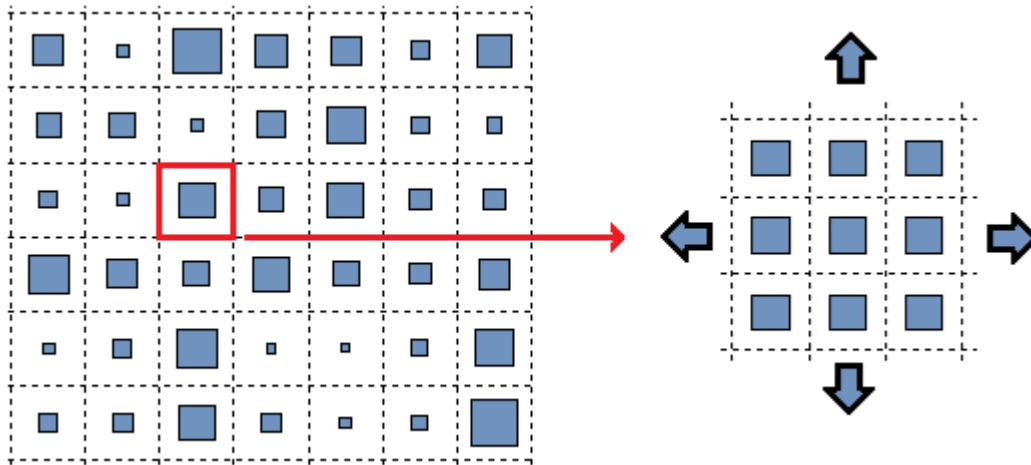


Figure 1-2 Infinite Array Approach.

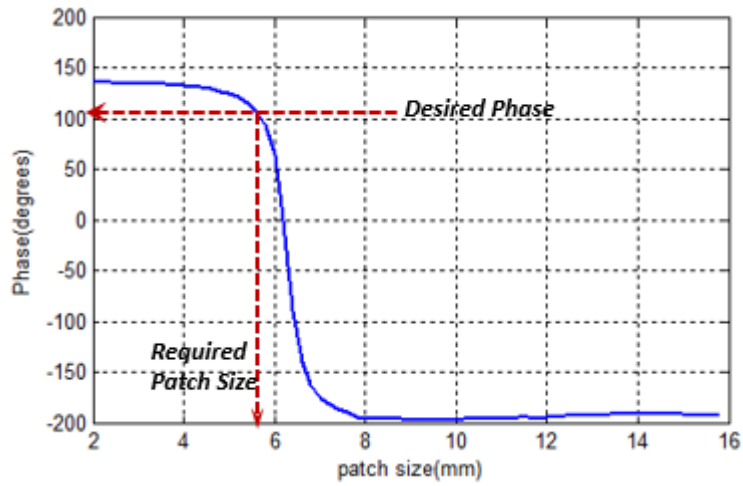


Figure 1-3 Typical phase design curve of the infinite array approach.

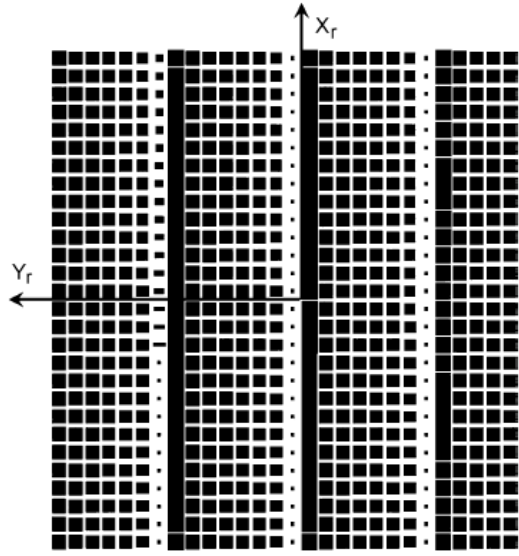


Figure 1-4 Mask pattern of reflectarray to be used as sub-reflector [20].

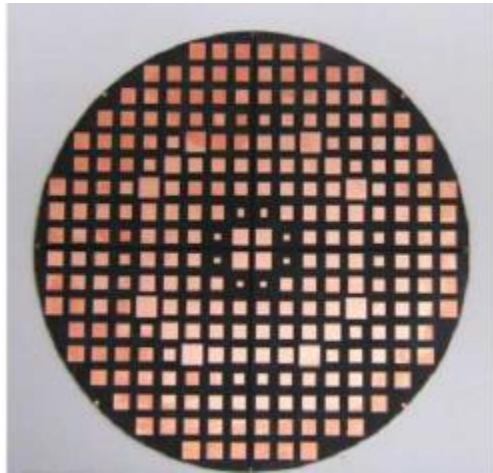


Figure 1-5 A photo of a reflectarray [21].



Figure 1-6 Isolated Element Approach.

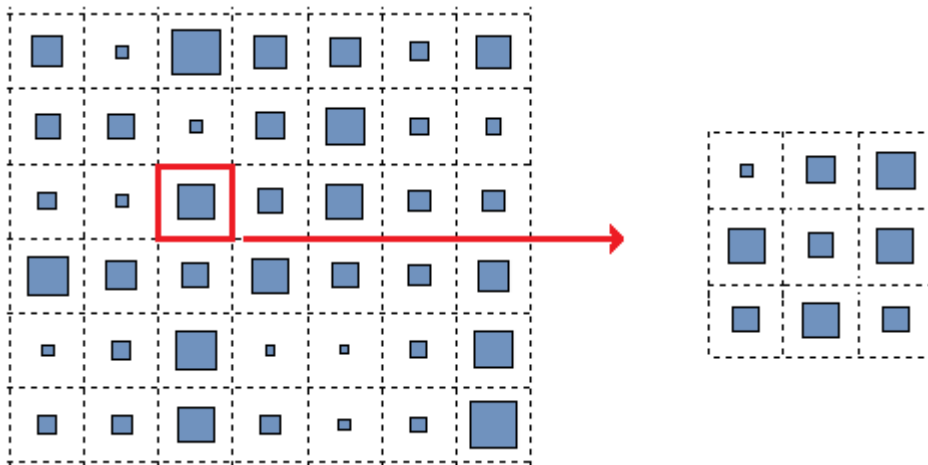


Figure 1-7 Surrounded Element Approach.

As a fast analysis technique, infinite array approach is again applicable. This technique involves tabulating the reflection phase as a function of incidence angle and element geometry (size or rotation etc.) for both parallel and perpendicular polarizations and computing the parallel and perpendicular components of the incident field on the reflectarray. As the effect of incidence angles is not usually taken into account in the design phase, a better accuracy as compared to design phase is obtained by this technique. However, the technique still depends on the local periodicity in terms of variation of the element geometry and incidence angle over the array. One principal motivation behind this approach is certainly the absence of a tool for analyzing practical reflectarrays populated with elements as many as thousands. Nevertheless, by observing the level of agreement between measurement

or full wave analysis results and approximate analysis results in many of the reflectarray design studies ([9], [22], [25], [26], [27] and [28]), it can be concluded that the accuracy of these approximate analysis methods needs to be improved.

1.1 Motivation

The method of moments [29] is an accurate tool for analyzing reflectarrays. However, most practical reflectarrays are composed of hundreds and even thousands of elements, which brings in the well-known problems of MoM with increasing unknowns. Nonetheless, the infinite array or local periodicity approach offers a very smart and efficient technique for the analysis and design of variable geometry reflectarrays, but this approach may not provide reliable results because of the assumed approximations. On the other hand, it is well experienced by the computational electromagnetics researchers that better accuracy almost always comes with its cost. With this challenge at hand, the target of this thesis is to develop an efficient analysis technique which is relatively accurate and efficient compared to the existing methods in the literature. When this is achieved, it becomes practical to use the analysis tool to optimize and design a reflectarray. The technique should yield an acceptable accuracy for the array pattern and it needs to be very fast (on the order of a few seconds) so as to be used in optimization algorithms. The efficiency of a numerical technique can be improved by reducing the size of the problem. In surrounded element approach [24], this is achieved by neglecting the mutual coupling from the elements that are not within the close vicinity of the target element. However, the analysis results in this study show that depending on the size of the elements a farther element may exhibit a larger mutual coupling compared to a closer element. Therefore it is concluded that the mutual coupling from each element should be considered in order not to sacrifice accuracy. Consequently, the size of the problem needs to be reduced by decreasing the number of unknowns on each element. For this purpose, various types of macro basis function approaches like Characteristic Basis Function Method (CBFM) [30] and Synthetic Function Expansion (SFX) [16] are proposed in the literature. On the other hand, characteristic modes obtained from the eigensolution of the MoM matrix [31] and [32] are very

good candidates to be used as entire domain basis functions on each element since the actual current distribution on an antenna element is the superposition of its characteristic modes. Using characteristic modes as entire domain basis functions has already been proposed in [33] for the efficient analysis of large antenna arrays. In this approach, first an isolated array element is analyzed by using sub-domain basis functions and the characteristic modes of the element are found numerically. Then a number of characteristic modes are used on each element to solve for the current distribution on the entire array. Since the number of modes used for each element is much smaller than the number of sub-domain basis functions on each element, a significant amount of reduction in the size of the overall MoM matrix is achieved. In [33], the method is applied to the analysis of large arrays composed of identical elements. This study does not make any projection about the application of the method for arrays with dissimilar element dimensions. Furthermore, it is still required to compute the conventional MoM matrix, to obtain the reduced form.

1.2 Original Contributions of the Study

This study is originated from usage of characteristic modes as Macro Basis Functions (MBFs) and elaborated by the steps described below. As opposed to [33], when the analyses of reflectarrays with non-uniform element sizes are considered, it seems that the characteristic modes for elements with different sizes should be calculated. However, it is recognized that the characteristic modes calculated for one element can be used for other elements with different sizes as long as the shape of the element and the organization of RWG basis functions on each element remain same. This is shown by examining the error in the approximate current distribution for excitation scenarios where the incidence type and angle are varying. Consequently, the first contribution of this study is to demonstrate the reusability of the characteristic modes for a sufficiently wide range of element sizes and incidence angles in a reflectarray problem. Next, it is observed that the dominant characteristic mode alone is sufficient to predict the far field pattern of the reflectarray accurate enough for an approximate analysis approach. Utilization of this observation results in a reduced (but not sparse) MoM matrix equation where the number of unknowns

is equal to the number of elements. The solution of the reduced matrix system yields the complex coefficients for the dominant characteristic mode on each element. Thus an approximate current distribution that takes into account the mutual couplings between all elements can be found. The entries of the reduced MoM matrix represent the interaction between the dominant modes of two elements. This interaction is a function of the sizes of the elements and two dimensional displacements between the elements. During the analyses conducted, it is recognized that the dependence of the interaction on the element sizes and on the displacement are separable from each other such that the entries of the reduced matrix can be expressed as a product of two functions, one in terms of sizes, and the other in terms of displacement for the elements which are not very close to each other. In the light of this observation, the entries of the reduced MoM matrix are efficiently tabulated as functions of displacement between interacting elements and sizes of interacting elements. Since the reduced MoM matrix can be very quickly filled by table look-up, a drastic reduction in the solution time is accomplished which paves way to implementation of various optimization methods for the design problem. The improvement obtained in the MoM solution of the entire array for different combinations of element sizes is the second important contribution of this dissertation because this efficient, approximate but accurate analysis approach enables a better - design for reflectarrays with non-uniform element sizes. The method requires neither the computation nor the storage of the conventional MoM matrix, which results in a significant relaxation of the memory requirements.

In the context of the dissertation, optimization algorithms that depend on directional search, such as The Method of Steepest Descent and the Non-linear Conjugate Gradient Method are implemented for the optimization of a 400 element reflectarray. Two different desired patterns are considered for optimization: First, a pattern that is separable in azimuth and elevation angles is synthesized where the cost function is defined as the sum of the pattern error, which is the difference between the desired and synthesized pattern in principal planes. Next, a non – separable pattern is synthesized where the cost function is defined as the sum of the pattern error in the entire half sphere in front of the reflectarray. Both optimization problems resulted in

a satisfactory convergence to the desired pattern. Furthermore, the patterns observed in the optimization result are verified by the analysis of reflectarrays obtained by the optimization, using ANSYS HFSS [34].

Although originally proposed for reflectarrays comprised of variable-size square patches, the method is extended to reflectarrays of different element types. An element that involves two separate pieces of conductors and behaves quite different than a resonant patch, is considered. The method is adapted for this element type by considering the characteristic modes of the distinct parts. An entirely different reflectarray element whose phase control mechanism is the rotation of the element, the split – ring resonator, is also investigated for application of the proposed method. The method is adapted for this element and shown to be feasible for it as well.

1.3 Organization of the Thesis

Chapter 2 of this thesis is dedicated to the development of the proposed fast analysis technique. The basic tools that are used throughout the thesis are described. In this chapter, reflectarrays of variable-size square patches are focused. The concepts of the usage of characteristic modes as macro basis functions and reusability of the characteristic modes for differently sized patches are also discussed. The work towards accelerating the construction of the reduced matrix is elaborated in this chapter and the proposed method is established. The accuracy of the proposed method is compared to that of the infinite array approach. Furthermore, the method is extended for using two characteristic modes.

In Chapter 3, the versatility of the proposed fast analysis approach is demonstrated through two different types of reflectarray elements. The first one is a wideband patch that does not exhibit a resonance behavior and the second one is a split ring resonator that is often used for circularly polarized reflectarrays. The modifications that are necessary for adaptation of the method are discussed and applied in this chapter.

In Chapter 4, the fast analysis approach is used for the design with the aid of the optimization methods such as the Method of Steepest Descent and the Non-linear Conjugate Gradient Method. As an initial point for the optimization, either the design offered by the infinite array approach or a uniform array with resonant patches is assumed. Two different optimization problems are studied and both resulted in designs with far field patterns that have good agreement with the desired antenna patterns.

Finally, Chapter 5 presents the conclusions of the thesis and possible extensions that could be researched.

The fundamental electromagnetic simulation method in this thesis is method of moments [11] with layered media Green's function [36]. All substrates are assumed lossless and metals are assumed perfect electric conductors with zero thickness. The time convention throughout the thesis is $e^{j\omega t}$. Free space wavelength is symbolized as λ_0 .

CHAPTER 2

DEVELOPMENT OF THE EFFICIENT COMPUTATION METHOD

This chapter is dedicated to the development of the efficient numerical analysis method that builds the foundation of the dissertation. The method of moments is the most basic tool that is employed and in-house codes are developed in MATLAB to implement it. By applying the MoM for mixed potential form of the Electric Field Integral Equation (EFIE), reference solutions for considered reflectarrays are found. Having the MoM computation facility, not only it becomes possible to obtain the reference solution for current density of an arbitrary reflectarray, but characteristic modes of a given structure can be found as well. Then, usage of a truncated set of characteristic modes as macro basis functions for reflectarrays and evaluation of various concepts becomes possible by comparing with reference solutions. By analyzing the error in the far field pattern with respect to the number of characteristic modes used on each element, it is concluded that even by considering only the dominant mode, satisfactory accuracy can be achieved. Therefore, it is proposed to use a single characteristic mode vector as a macro basis function for all elements in the array. By the transformation obtained by this macro basis function approach, a drastic reduction of the impedance matrix size can be achieved. Reusing the same characteristic mode for all different sized elements is also investigated, and it is observed that this proves successful in terms of far field estimation. The success of this concept is due to preservation of coupling between elements via maintaining the information provided by the original impedance matrix of MoM. Although the matrix size is reduced significantly, the computation of the reduced matrix is still a burden, because it requires the computation of the original impedance matrix. To alleviate this burden, the feasibility of tabulating the reduced matrix terms, which depends on the block mutual impedance matrix of two elements, is examined. It is clear that there are too many cases that vary the mutual impedance matrix for a large array, considering the combinations of size and displacement possibilities. However,

it is observed that for sufficiently separated patches, the reduced matrix term is almost a separable function of the two dimensional displacement between patches and patch sizes associated with the matrix term. For close neighboring patches, on the other hand, the number of possible combinations is of manageable count. With the separability, it becomes sufficient to characterize the effect of displacement and the effect of the sizes of interacting two distant patches. The details of the above explained concepts are given in the forthcoming parts.

2.1 MoM Analysis Approach for Reflectarrays

The method of moments [29] with closed form stratified media Green's function [36] is an efficient method for the analysis of printed microstrip structures, because it only requires discretization of the metallization and modeling the problem as a surface integral equation. When finiteness of the ground plane is desired to be considered, volume integral equation formulation may be employed, but this approach requires introducing basis functions on the substrate and ground metallization as well as the signal metallization. The drawback in the former of these two approaches is taking the substrate and the ground plane erroneously as infinite. On the other hand, for large arrays, finiteness of the ground plane and substrate is usually not a big problem and often ignored for simplicity and efficiency.

The method of moments depends on expressing an unknown quantity in terms of some basis functions either defined on the entire domain, or in sufficiently small regions of the domain. The basis function used in this study is Rao-Wilton-Glisson [37] basis function, which is of subdomain type. Electric Field Integral Equation is solved to find the current distribution on patches. The Green's functions for vector and scalar potentials are numerically computed by the three-level method described in [36]. This method expresses the Green's function as a sum of exponentials with complex exponents. Singularity of the Green's function is handled by classical singularity subtraction technique. All metals are assumed PEC and no loss is taken into account throughout the thesis. MATLAB is used as code development environment.

A reflectarray problem typically involves a feed antenna or a plane wave that is incident on the reflectarray (Figure 2-1-a). In either case, the incident field for the MoM analysis with layered media Green's function is the sum of the field incident from the source, \bar{E}_0^{inc} , (plane wave or feed antenna) in the absence of the dielectric coated ground plane and the field reflected from the dielectric coated ground plane, \bar{E}^{ref} (Figure 2-1-b). When the patches exist over the substrate, due to \bar{E}_0^{inc} and \bar{E}^{ref} , a current density is induced on the patches such that the tangential electric field vanishes over them (Figure 2-1-c). This current density generates \bar{E}^{sc} at the right side of the reflectarray. Therefore, total electric field at the right hand side of the reflectarray is calculated as in (2-1):

$$\bar{E}^{total} = \bar{E}_0^{inc} + \bar{E}^{ref} + \bar{E}^{sc} \quad (2-1)$$

The incident field for MoM calculations is:

$$\bar{E}^{inc} = \bar{E}_0^{inc} + \bar{E}^{ref} \quad (2-2)$$

\bar{E}^{inc} in (2-2) is to be used in the electric field integral equation that will be derived later. The patch current, \bar{J}_p , is the solution of the electric field integral equation. The radiation due to \bar{J}_p alone does not give the far field of the reflectarray. Another significant contribution to the far field is the scattering from the ground plane in the absence of the patches [38]. This can be appreciated instantly if a hypothetical problem where no metallization exists over the substrate is considered. In this problem, \bar{J}_p would be zero, but a finite radiation at the far zone would be observed. Therefore, the scattering from the ground plane should be taken into account for the overall far field of the reflectarray. This calculation can be approximately done by using physical optics considering the actual size of the reflectarray PCB, following the approach in [39]. On the other hand, when calculating \bar{E}^{inc} , substrate and the ground plane are considered as infinitely large. The primary incident field, \bar{E}_0^{inc} , is first decomposed into its parallel and perpendicular polarized components for each observation point on the substrate. Then, the parallel and perpendicular components of the reflected field are found by using the respective angle dependent reflection coefficient at each observation point. The reflection coefficients are found by using

the Fresnel reflection coefficients [40] and calculating the result of the power series due to infinite back and forth bouncing at the vacuum-substrate and ground plane-substrate interfaces. When \bar{J}_p is found by solving EFIE, its radiation is calculated by the method of stationary phase [41], as if the ground plane and substrate are infinite. Even though this overall approach brings in an approximated inclusion of radiation from the ground, comparisons with solutions of Finite Element Method solvers reveal that the approximation is accurate enough.

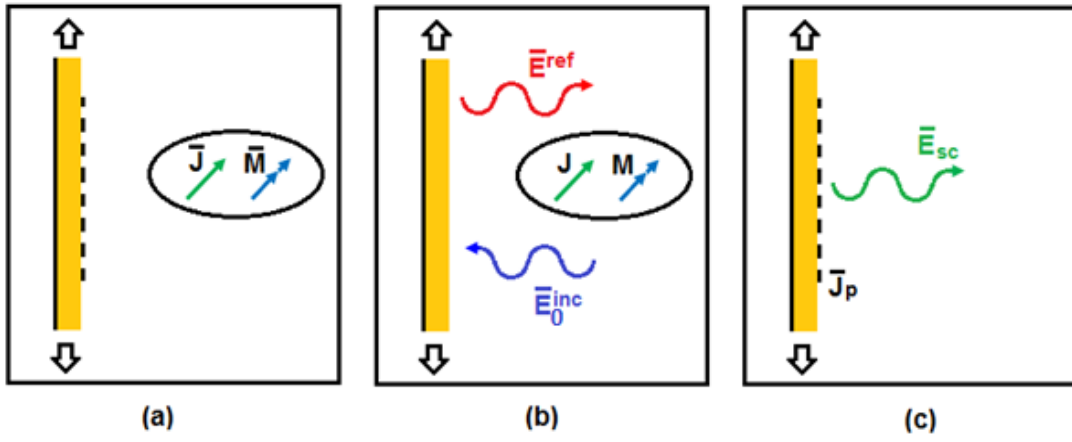


Figure 2-1 Reflectarray problem: a) Problem definition, b) Fields in absence of patch, c) fields scattered by patch.

2.1.1 The Mixed Potential Formulation

It is well known that if Lorentz Gauge is assumed, electric field can be expressed as:

$$\bar{E} = -j\omega\bar{A} - \nabla\varphi \quad (2-3)$$

With a given current distribution \bar{J}_s and charge distribution q_s over a surface S , the vector and scalar potentials can be written down in terms of the sources and Green's functions as:

$$\bar{A}(\bar{r}) = \int_S \bar{J}_s(\bar{r}') \bar{G}^A(\bar{r}, \bar{r}') ds', \quad \varphi(\bar{r}) = \int_S q_s(\bar{r}') G^\varphi(\bar{r}, \bar{r}') ds' \quad (2-4)$$

In (2-4), $\bar{\bar{G}}^A(\bar{r}, \bar{r}')$ and $G^\varphi(\bar{r}, \bar{r}')$ stand for the Green's functions for vector and scalar potentials. The charge density and current density are related by the continuity equation as:

$$q = -\frac{\bar{\nabla} \cdot \bar{J}_s}{j\omega} \quad (2-5)$$

Equation (2-5) can be inserted in (2-4) and therefore both vector and scalar potentials can be expressed in terms of current density. When Green's Functions for vector and scalar potentials and current density are known, (2-5), (2-4) and (2-3) can be used to obtain the electric field. Nevertheless, in scattering problems it is required to find out the current density when the incident field is known. For scattering problems, an incident electric field, \bar{E}^{inc} , exists and it induces currents that generate a scattered field, \bar{E}^{sc} . The total tangential electric field, which is the sum of \bar{E}^{inc} and \bar{E}^{sc} , vanishes on perfectly conducting surfaces:

$$\begin{aligned} \{\bar{E}^{inc}(\bar{r}) + \bar{E}^{sc}(\bar{r})\}_{tan} &= 0 \\ \Rightarrow \hat{n} \times \left\{ -j\omega \int_S \bar{J}_s(\bar{r}') \bar{\bar{G}}^A(\bar{r}, \bar{r}') ds' + \nabla \int_S \frac{\bar{\nabla}' \cdot \bar{J}_s(\bar{r}')}{j\omega} G^\varphi(\bar{r}, \bar{r}') ds' \right\} & \quad (2-6) \\ &= \hat{n} \times \bar{E}^{inc}(\bar{r}), \quad r \text{ is on } S \end{aligned}$$

The right hand side of the equation is known, but the current density, $\bar{J}_s(\bar{r}')$ is unknown. Method of moments is to be applied to solve for the current density.

2.1.2 Application of Method of Moments

Due to their superior properties in modeling an arbitrary current density, Rao – Wilton – Glisson type basis functions are used throughout the thesis. The RWG basis associated with the n^{th} edge and the triangle couple (T_n^+ & T_n^-) is defined as ([37]):

$$\bar{f}_n(\bar{r}) = \begin{cases} \frac{l_n \bar{\rho}_n^+}{2A_n^+}, & r \in T_n^+ \\ \frac{l_n \bar{\rho}_n^-}{2A_n^-}, & r \in T_n^- \\ 0, & \text{otherwise} \end{cases} \quad (2-7)$$

$$\bar{\rho}_n^+ = \bar{r} - \bar{r}_o^+, \quad \bar{\rho}_n^- = \bar{r}_o^- - \bar{r}$$

where, A_n^+ and A_n^- represent the area of T_n^+ (the positive triangle) and T_n^- (the negative triangle) respectively. Vector $\bar{\rho}_n^+$ extends from the free vertex, \bar{r}_o^+ , of T_n^+ to any point, \bar{r} , in T_n^+ ; whereas $\bar{\rho}_n^-$ extends from any point, \bar{r} , in T_n^- to the free vertex, \bar{r}_o^- , of T_n^- . The length of the common edge of T_n^+ and T_n^- is l_n . Figure 2-2 depicts a better visualization of these parameters.

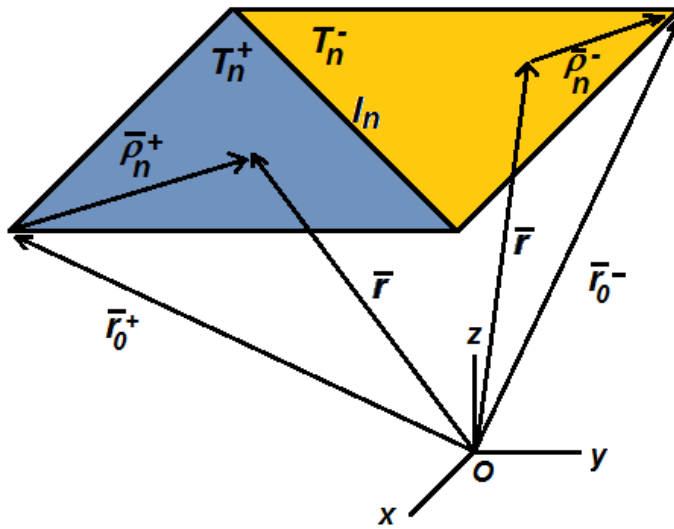


Figure 2-2 Explanation of parameters in (2-7).

When RWG bases are used, the unknown current is expressed in terms of \bar{f}_n s. The surface divergence of \bar{f}_n , which is proportional to the surface charge density via (2-5), is computed as in (2-8).

$$\bar{\nabla}_s \cdot \bar{f}_n(\bar{r}) = \begin{cases} \frac{l_n}{2A_n^+}, & r \in T_n^+ \\ -\frac{l_n}{2A_n^-}, & r \in T_n^- \\ 0, & \text{otherwise} \end{cases} \quad (2-8)$$

Unknown current density, \bar{J}_s , and the associated charge density, q_s , can be expressed as a weighted sum of \bar{f}_n s and q_n s as in (2-9).

$$\bar{J}_s = \sum_{n=1}^N \alpha_n \bar{f}_n, \quad q_s = \sum_{n=1}^N \alpha_n q_n = \sum_{n=1}^N -\alpha_n \frac{\bar{\nabla}_s \cdot \bar{f}_n(\bar{r})}{j\omega} \quad (2-9)$$

Using (2-9) in expressing the scattered field,

$$\begin{aligned} \bar{E}^{sc}(\bar{r}) = & -j\omega \int_S G^A(\bar{r}, \bar{r}') \sum_{n=1}^N \alpha_n \bar{f}_n(\bar{r}') ds' \\ & + \nabla \int_S G^\varphi(\bar{r}, \bar{r}') \sum_{n=1}^N \alpha_n q_n(\bar{r}') ds' \end{aligned} \quad (2-10)$$

As the tangential electric field vanishes over PEC surfaces, when Galerkin's testing scheme is applied, following relation is obtained.

$$\langle \{\bar{E}^{sc}(\bar{r})\}_{tan}, \bar{f}_m(\bar{r}) \rangle = \langle \{-\bar{E}^{inc}(\bar{r})\}_{tan}, \bar{f}_m(\bar{r}) \rangle \quad (2-11)$$

In the specific content of this work, \bar{E} field can be directly used (without taking the tangential part), because the test function is tangential itself. Thus, (2-11) becomes,

$$\begin{aligned} & \left\langle -j\omega \int_S \bar{G}^A(\bar{r}, \bar{r}') \sum_{n=1}^N \alpha_n \bar{f}_n(\bar{r}') ds' \right. \\ & \left. + \nabla \int_S G^\varphi(\bar{r}, \bar{r}') \sum_{n=1}^N \alpha_n q_n(\bar{r}') ds' \right\rangle, \bar{f}_m(\bar{r}) \rangle \\ & = \langle \{-\bar{E}^{inc}(\bar{r})\}_{tan}, \bar{f}_m(\bar{r}) \rangle \end{aligned} \quad (2-12)$$

Due to the divergence conforming property of RWG basis functions, the gradient term can be transferred onto the testing function by using the following identity [37]:

$$\langle \nabla \varphi, \bar{f}_m \rangle = \int_S \nabla \varphi \cdot \bar{f}_m ds = \int_S -\varphi \nabla_s \cdot \bar{f}_m ds \quad (2-13)$$

As the integrals associated with the inner products are restricted to the domain of \bar{f}_m ,

$$\begin{aligned}
& \langle \nabla \left\{ \int_S G^\varphi(\bar{r}, \bar{r}') \sum_{n=1}^N \alpha_n \bar{q}_n(\bar{r}') ds' \right\}, \bar{f}_m(\bar{r}) \rangle \\
&= - \int_{T_m} \left\{ \int_S G^\varphi(\bar{r}, \bar{r}') \sum_{n=1}^N \alpha_n q_n(\bar{r}') ds' \right\} \nabla_s \cdot \bar{f}_m ds \\
&= -l_m \left[\frac{1}{2A_m^+} \int_{T_m^+} ds \int_S G^\varphi(\bar{r}, \bar{r}') \sum_{n=1}^N \alpha_n q_n(\bar{r}') ds' \right. \\
&\quad \left. - \frac{1}{2A_m^-} \int_{T_m^-} ds \int_S G^\varphi(\bar{r}, \bar{r}') \sum_{n=1}^N \alpha_n q_n(\bar{r}') ds' \right] \tag{2-14} \\
&\cong -l_m \left[\int_S G^\varphi(\bar{r}_m^{c+}, \bar{r}') \sum_{n=1}^N \alpha_n q_n(\bar{r}') ds' \right. \\
&\quad \left. - \int_S G^\varphi(\bar{r}_m^{c-}, \bar{r}') \sum_{n=1}^N \alpha_n q_n(\bar{r}') ds' \right]
\end{aligned}$$

where \bar{r}_m^{c+} and \bar{r}_m^{c-} represent the coordinates of the center of mass of the positive and negative parts of the m^{th} RWG basis, respectively. In (2-14), the integrals on the unprimed variable is approximated by the areas of the domains T_m^+ and T_m^- times the value of the integrand at the centers of T_m^+ and T_m^- .

Approximation in (2-14) can be made for the vector potential and the incident field as well:

$$\begin{aligned}
& \left\langle \int_S \bar{G}^A(\bar{r}, \bar{r}') \sum_{n=1}^N \alpha_n \bar{f}_n(\bar{r}') ds', \bar{f}_m(\bar{r}) \right\rangle \\
&= l_m \left[\frac{1}{2A_m^+} \int_{T_m^+} \int_S \bar{G}^A(\bar{r}, \bar{r}') \sum_{n=1}^N \alpha_n f_n(\bar{r}') ds' \cdot \bar{\rho}_m^+ ds \right. \\
&\quad \left. + \frac{1}{2A_m^-} \int_{T_m^-} \int_S \bar{G}^A(\bar{r}, \bar{r}') \sum_{n=1}^N \alpha_n f_n(\bar{r}') ds' \cdot \bar{\rho}_m^- ds \right] \tag{2-15}
\end{aligned}$$

$$\cong -\frac{l_m}{2} \left[\int_S \bar{G}^A(\bar{r}_m^{c+}, \bar{r}') \sum_{n=1}^N \alpha_n f_n(\bar{r}') ds' \cdot \bar{\rho}_m^{c+} + \int_S \bar{G}^A(\bar{r}_m^{c-}, \bar{r}') \sum_{n=1}^N \alpha_n f_n(\bar{r}') ds' \cdot \bar{\rho}_m^{c-} \right]$$

In (2-15), $\bar{\rho}_m^{c+}$ is the vector from the corner of T_m^+ to the center of mass of T_m^+ while $\bar{\rho}_m^{c-}$ is the vector from the center of mass of T_m^- to the corner of T_m^- .

$$\begin{aligned} & \langle \bar{E}^{inc}(\bar{r}), \bar{f}_m(\bar{r}) \rangle \\ &= l_m \left[\frac{1}{2A_m^+} \int_{T_m^+} \bar{E}^{inc}(\bar{r}) \cdot \bar{\rho}_m^+ ds + \frac{1}{2A_m^-} \int_{T_m^-} \bar{E}^{inc}(\bar{r}) \cdot \bar{\rho}_m^- ds \right] \\ &\cong -\frac{l_m}{2} [\bar{E}^{inc}(\bar{r}_m^{c+}) \cdot \bar{\rho}_m^{c+} + \bar{E}^{inc}(\bar{r}_m^{c-}) \cdot \bar{\rho}_m^{c-}] \end{aligned} \quad (2-16)$$

When equations (2-14), (2-15), and (2-16) are used in (2-12), and the procedure is repeated for all \bar{f}_m s, (2-17) is obtained:

$$\bar{Z} \bar{\alpha} = \bar{V} \quad (2-17)$$

In (2-17), $\bar{\alpha}$ is the vector of unknown RWG basis coefficients, \bar{V} is the voltage vector as shown in (2-18) and \bar{Z} is the impedance matrix. Entries of \bar{V} and \bar{Z} are explained in (2-19) and (2-20).

$$\begin{aligned} \bar{\alpha} &= [\alpha_1 \quad \alpha_2 \quad \dots \alpha_N]^T, \\ \bar{V} &= [V_1 \quad V_2 \quad \dots V_N]^T \end{aligned} \quad (2-18)$$

$$\begin{aligned}
Z_{mn} = j\omega l_m \left\{ \int_{T_n} \bar{G}^A(\bar{r}_m^{c+}, \bar{r}') f_n(\bar{r}') ds' \cdot \bar{\rho}_m^{c+} \right. \\
+ \int_{T_n} \bar{G}^A(\bar{r}_m^{c-}, \bar{r}') f_n(\bar{r}') ds' \cdot \bar{\rho}_m^{c-} \left. \right\} \\
- l_m \left\{ \int_{T_n} G^\varphi(\bar{r}_m^{c+}, \bar{r}') q_n(\bar{r}') ds' \right. \\
\left. - \int_{T_n} G^\varphi(\bar{r}_m^{c-}, \bar{r}') q_n(\bar{r}') ds' \right\}
\end{aligned} \tag{2-19}$$

$$V_m = \frac{l_m}{2} [\bar{E}^{inc}(\bar{r}_m^{c+}) \cdot \bar{\rho}_m^{c+} + \bar{E}^{inc}(\bar{r}_m^{c-}) \cdot \bar{\rho}_m^{c-}] \tag{2-20}$$

2.1.2.1 Computation of Integrals

2.1.2.1.1 Computation of Non-singular Integrals

For nonsingular integrals and the nonsingular parts of singular integrals, the integrals are approximated by Gaussian quadrature. In the context of this study, 3 point quadrature yields sufficiently accurate results. To make triangular quadrature, first the quadrature points are evaluated with simplex transformation [42]. In simplex coordinates, the triangle over the integration is computed is an isosceles triangle with corners ([0 0], [1 0], [0 1]).

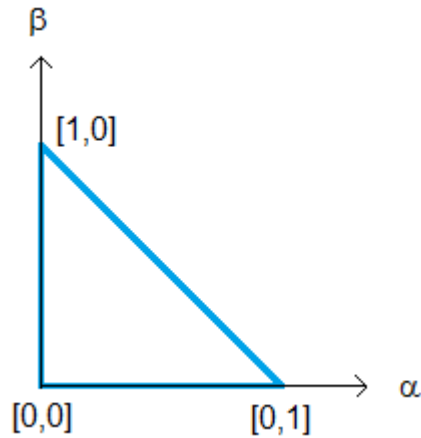


Figure 2-3 Basic triangle in simplex coordinates.

There exists a one to one mapping between any point in the original triangle in x-y domain with a point in the basic triangle in simplex coordinates. A given point (α_0, β_0) in simplex coordinates can be mapped to the x-y domain as:

$$\begin{aligned} x_0 &= (1 - \alpha - \beta)x_1 + \alpha x_2 + \beta x_3 \\ y_0 &= (1 - \alpha - \beta)y_1 + \alpha y_2 + \beta y_3 \end{aligned} \quad (2-21)$$

where x_i and y_i ($i = 1,2,3$) represent the coordinates of the vertices of the triangle in x-y domain. (x_0, y_0) is the point in x-y domain that corresponds to the point (α_0, β_0) in the simplex coordinates. The integral in original domain T can be written in terms of the integral in simplex coordinates with the aid of the Jacobian matrix, $J(\alpha, \beta)$, which is equal to twice the area, A of the original triangle.

$$\begin{aligned} \iint_T f(x, y) dx dy &= \iint_T f(\alpha, \beta) |J(\alpha, \beta)| d\alpha d\beta \\ &= 2A \int_0^1 d\alpha \int_0^{1-\alpha} f(\alpha, \beta) d\beta \end{aligned} \quad (2-22)$$

The integral in simplex coordinates is approximated by the 3 point Gaussian quadrature as:

$$\int_0^1 d\alpha \int_0^{1-\alpha} f(\alpha, \beta) d\beta \cong \sum_{j=1}^3 w_j f(\alpha_j, \beta_j) \quad (2-23)$$

where w_j , α_j , and β_j are given as in Table 2-1.

Table 2-1 Coordinates and weights of quadrature points in simplex coordinates.

	α	β	W
$j = 1$	1/6	1/6	1/3
$j = 2$	2/3	1/6	1/3
$j = 3$	1/6	2/3	1/3

The sampling positions of the function f in x-y coordinates can be found with the help of (2-21), by inserting α_j and β_j for all j . Thus:

$$\begin{bmatrix} x_1^q & y_1^q \\ x_2^q & y_2^q \\ x_3^q & y_3^q \end{bmatrix} = \begin{bmatrix} 2/3 & 1/6 & 1/6 \\ 1/6 & 2/3 & 1/6 \\ 1/6 & 1/6 & 2/3 \end{bmatrix} \begin{bmatrix} x_1 & y_1 \\ x_2 & y_2 \\ x_3 & y_3 \end{bmatrix} \quad (2-24)$$

where x_i^q & y_i^q ($i = 1,2,3$) stand for the coordinates of quadrature (sampling) points of the triangle in the original domain and x_i & y_i ($i = 1,2,3$) stand for the coordinates of the vertices of the triangle in original domain.

2.1.2.1.2 Computation of Singular Integrals

There are various methods in the literature for computation of the singular integrals with RWG basis, where the most preferred one is given in [43]. When the general method of [43] is applied to the problem under consideration, it turns into the geometry shown in Figure 2-4.

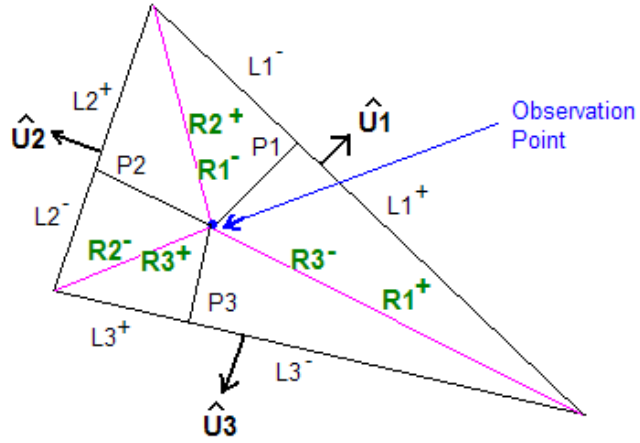


Figure 2-4 Geometry for computation of singular integrals.

The variables in Figure 2-15 are explained in Table 2-2.

Table 2-2 Explanations of variables for computation of singular integrals

R_i^-, R_i^+	Distances between the observation point and the end points of i^{th} edge. +/- designation is w.r.t. right hand rule.
L_i^-, L_i^+	Distances between the projection of the observation point to the i^{th} edge and the end points of the i^{th} edge. +/- designation is w.r.t. right hand rule.
\hat{U}_i	Unit normal vectors orthogonal to i^{th} edge.
P_i	Length of projection from the observation point to the i^{th} edge.

Two different types of singular integrals must be handled for this problem:

$$I_1 = \int_T \frac{e^{jkR}}{R} ds, \quad \bar{I}_2 = \int_T \vec{\rho} \frac{e^{jkR}}{R} ds \quad (2-25)$$

Before directly trying to evaluate the integrals in (3-21), it is convenient to split the integrals into singular and nonsingular parts:

$$\begin{aligned}
I_1 &= \int_T \frac{e^{jkR}}{R} ds \cong \int_R \frac{1 - jkR}{R} ds = \int_R \frac{1}{R} ds + \int_R \frac{-jkR}{R} ds \\
\bar{I}_2 &= \int_T \bar{\rho} \frac{e^{jkR}}{R} ds \cong \int_R \bar{\rho} \frac{1 - jkR}{R} ds = \int_R \bar{\rho} \frac{1}{R} ds + \int_R -jk\bar{\rho} ds
\end{aligned} \tag{2-26}$$

where

$$\begin{aligned}
I_1^{singular} &= \int_R \frac{1}{R} ds, \quad \bar{I}_2^{singular} = \int_R \bar{\rho} \frac{1}{R} ds \\
I_1^{non-singular} &= \int_R \frac{-jkR}{R} ds, \quad \bar{I}_2^{non-singular} = \int_R -jk\bar{\rho} ds
\end{aligned} \tag{2-27}$$

The non-singular parts of I_1 & \bar{I}_2 can be evaluated with the rules explained in Section 2.1.2.1.1. According to [43], evaluation of the singular parts of I_1 can be carried out as follows:

$$I_1^{singular} = \sum_{j=1}^3 P_j \ln \left[\frac{L_j^+ + R_j^+}{L_j^- + R_j^-} \right] \tag{2-28}$$

For evaluation of $I_2^{singular}$ some intermediate values must first be computed:

$$\bar{I}_2^0 = \frac{1}{2} \sum_{j=1}^3 \hat{U}_j \left\{ P_j^2 \ln \left[\frac{L_j^+ + R_j^+}{L_j^- + R_j^-} \right] + L_j^+ R_j^+ - L_j^- R_j^- \right\} \tag{2-29}$$

Then, $\bar{I}_2^{singular}$ can be calculated as:

$$\bar{I}_2^{singular} = \bar{\rho}_0 I_1^{singular} + \bar{I}_2^0 \tag{2-30}$$

where $\bar{\rho}_0$ is value of $\bar{\rho}$ at the observation point. The observation point is chosen as the center of mass of the triangle.

2.1.2.2 Domain Discretization

Discretization of the solution domain is actually a diverse topic, but it is considered up to specific properties and assumptions of this study. As the metallizations under concern are of planar geometry, two dimensional and co-planar RWG bases are sufficient. Furthermore, owing to regularity of the practical patch shapes, structured mesh is preferred over unstructured mesh because owing to invariances in geometry, number of impedance computations can be minimized. An example of structured mesh is shown in Figure 2-5. For a rectangular domain, if the number of triangles is N along one dimension and M along the other, the total number of RWG bases is given by,

$$\text{Total number of RWG basis functions} = 3MN - M - N \quad (2-31)$$

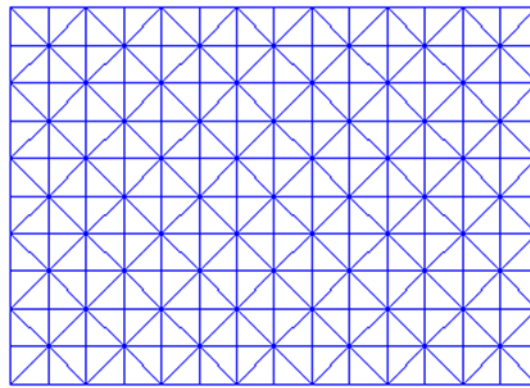


Figure 2-5 An example of a structured mesh.

On the other hand, unstructured mesh could be better in representing curved objects like a split ring. When those types of objects are analyzed, unstructured mesh is preferred. An example of an unstructured mesh is shown in Figure 2-6.

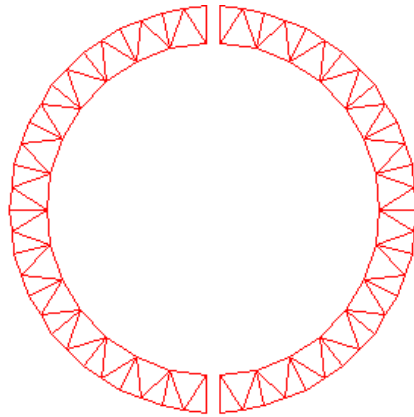


Figure 2-6 An example of an unstructured mesh.

The RWG mesh in method of moments computations is a data structure with the properties listed in Table 2-3. The explanations can be better understood by inspecting Figure 2-2.

Table 2-3 Properties of RWG data structure.

Property name	Explanation
<i>Corner1</i>	coordinates of the free vertex of the positive triangle
<i>Corner2</i>	coordinates of the free vertex of the negative triangle
<i>Common_edge_end1</i>	coordinates of the 1 st point of the common edge
<i>Common_edge_end2</i>	coordinates of the 2 nd point of the common edge
<i>Rho_plus</i>	$\bar{\rho}$ vector of the positive triangle
<i>Rho_minus</i>	$\bar{\rho}$ vector of the negative triangle
<i>R_plus</i>	coordinates of center of mass of the positive triangle
<i>R_minus</i>	coordinates of center of mass of the negative triangle
<i>L</i>	Length of the common edge of the positive and the negative triangles

2.1.3 Validation of MATLAB Codes

In order to make sure that MATLAB codes are correctly written, some sample designs are made and designed reflectarrays are solved with a MoM based commercial software Ansoft Designer.

Following examples show the degree of similarity of the far fields of the reflectarrays found by MoM codes in this work and Ansoft Designer. The pattern in Figure 2-7 belongs to a reflectarray of collinear 18 elements designed for a sectoral beam. Figure 2-8 depicts the results for another collinear 18 element array designed for a scanned beam (to -20 degrees from boresight). The patterns are due to patch currents only and normalized to their peak values. Figures show that Ansoft Designer and this work are in very well agreement.

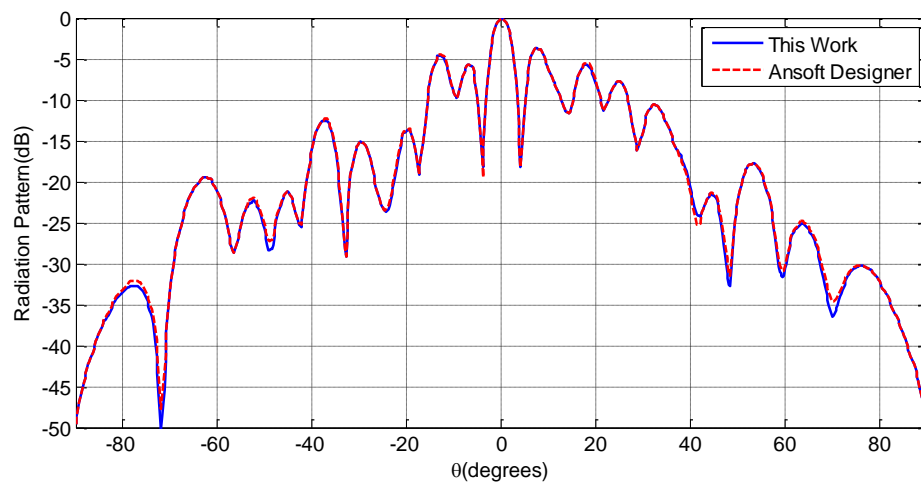


Figure 2-7 Comparison of patterns for the reflectarray designed for sectoral beam.

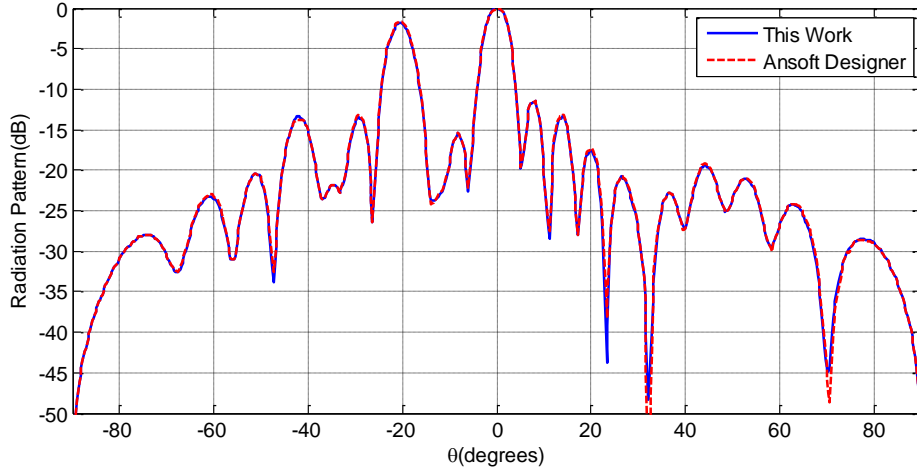


Figure 2-8 Comparison of patterns for the reflectarray designed for scanned beam.

2.2 Characteristic Modes and Reusability of Characteristic Modes

2.2.1 Characteristic Mode Concept

The theory of characteristic modes was established by Harrington & Mautz in 1971 [31]. Details of that study will be summarized here for the sake of completeness.

In general, impedance matrix ($\bar{\bar{Z}}$) obtained by method of moments is symmetric. The real ($\bar{\bar{R}}$) and imaginary parts ($\bar{\bar{X}}$) of the impedance matrix indicated in (2-32) are also symmetric.

$$\bar{\bar{Z}} = \bar{\bar{R}} + j\bar{\bar{X}} \quad (2-32)$$

Eigenvalue equation in (2-33) can be written:

$$\bar{\bar{Z}}\bar{J}_n = v_n\bar{\bar{M}}\bar{J}_n \quad (2-33)$$

In (2-33), v_n are the eigenvalues and \bar{J}_n are the eigenvectors. $\bar{\bar{M}}$ will always diagonalize $\bar{\bar{Z}}$, provided that it is symmetric. However, only if it is chosen to be equal to $\bar{\bar{R}}$, orthogonality of the radiation patterns is achieved. With this specific case, (2-33) turns into:

$$(\bar{R} + j\bar{X})\bar{J}_n = v_n\bar{R}\bar{J}_n \quad (2-34)$$

If v_n is defined as:

$$v_n = 1 + j\lambda_n \quad (2-35)$$

Generalized eigenvalue equation at (2-36) is obtained.

$$\bar{X}\bar{J}_n = \lambda_n\bar{R}\bar{J}_n \quad (2-36)$$

\bar{J}_n s that satisfy (2-36) are the characteristic modes and λ_n and \bar{J}_n are real. Characteristic modes are orthogonal in the following senses:

$$\langle \bar{J}_n, \bar{R}\bar{J}_m \rangle = 0, \quad \langle \bar{J}_n, \bar{X}\bar{J}_m \rangle = 0, \quad \langle \bar{J}_n, \bar{Z}\bar{J}_m \rangle = 0 \quad (2-37)$$

Since the characteristic modes form a complete set, the current on the conductor can be expressed in terms of the characteristic modes.

$$\bar{J} = \sum_n^N \frac{V_n^i \bar{J}_n}{1 + j\lambda_n}, \quad V_n = \iint_S \bar{J}_n \cdot \bar{E}^i ds \quad (2-38)$$

$$\text{Modal Significance} = \frac{1}{1 + j\lambda_n} \quad (2-39)$$

The term in (2-39) represents the modal significance as it scales the mode current. A simple example is investigated to show the concept. A rectangular patch with $0.53\lambda_0$ width and $0.36\lambda_0$ length is considered at 10 GHz. The patch is assumed to be etched over a substrate with relative permittivity 4.2 and height 1.59 mm. The patch is discretized using 268 RWG basis functions as shown in Figure 2-9.

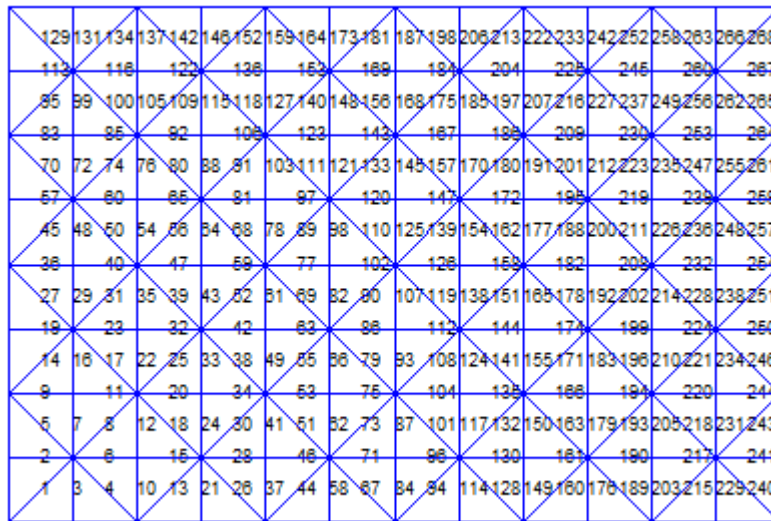


Figure 2-9 Mesh used for the rectangular patch.

The modes are calculated by solving (2-36) and they are sorted with respect to the modal significance defined in (2-39). Modal significance value is plotted logarithmically in Figure 2-10. Unfortunately modal significance does not alone tell how strongly a mode will be excited. Actual modal excitation coefficients can be found by solving (2-38), which tells that they are determined by correlation of the characteristic mode with the incident field as well.

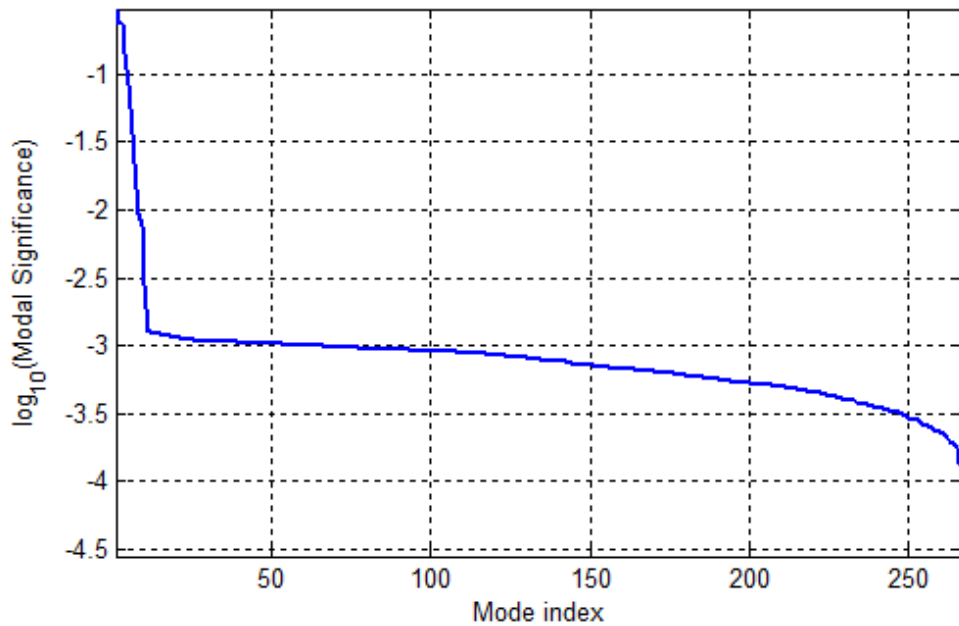


Figure 2-10 Modal significance of characteristic modes.

Figure 2-11 shows the first three most significant modes for the rectangular patch described above. Vectorial representations are superimposed upon color-weighted plots. The current for these modes are almost purely unidirectional. For the fourth mode (Figure 2-12) however, both x-directed and y-directed currents exist.

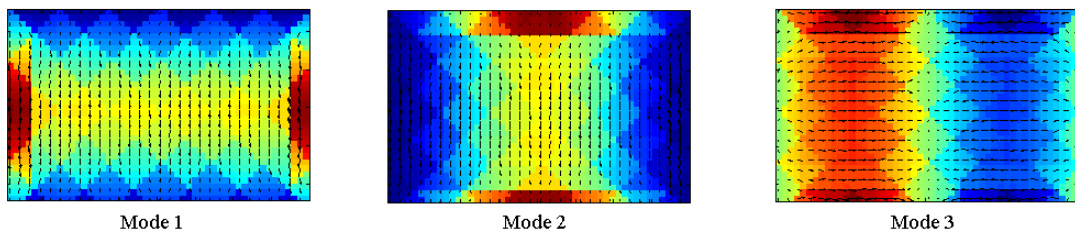


Figure 2-11 First three characteristic modes for the rectangular patch.

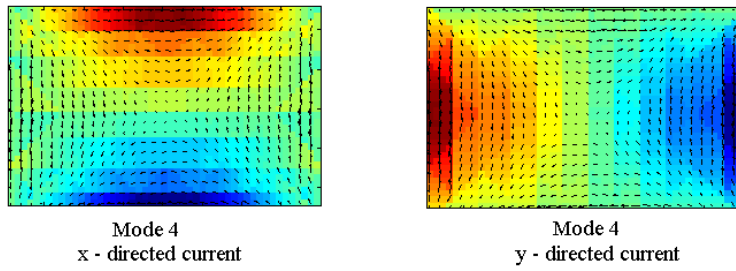


Figure 2-12 Fourth most significant mode for the rectangular patch.

Another example that is examined is a square patch, which is widely used in reflectarrays. Patch width and height is $0.23\lambda_0$, frequency and substrate parameters are the same as above. As both dimensions of the patch is same, the first two modes are degenerate, i.e. have the same eigenvalue. They are plotted in Figure 2-13.

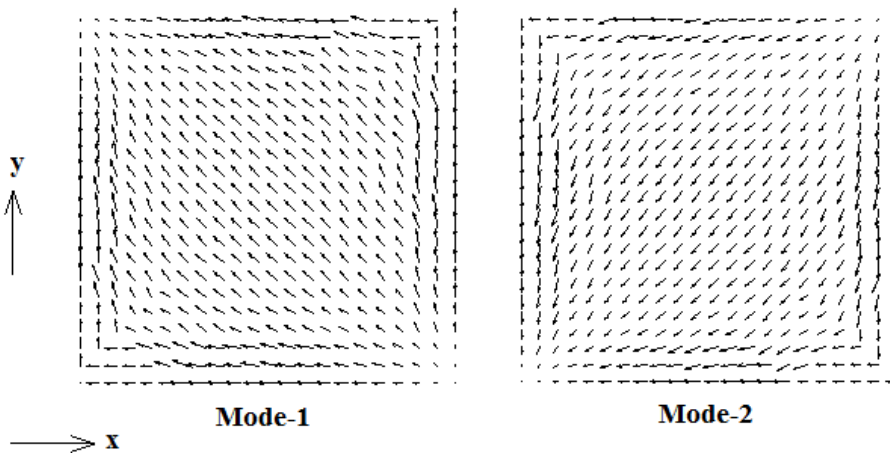


Figure 2-13 The first two significant modes for the square patch.

When this patch is illuminated by a normally incident plane wave polarized along y direction, the first two modes are almost equally excited (due to quasi-symmetric structure of the impedance matrix). Other modes are hardly excited, i.e. less than 100 dB below the first two modes. Despite these examples study the characteristic modes of a rectangular patch, characteristic modes can be calculated for arbitrary shapes. In [32], characteristic modes for various planar geometries are calculated and they are repeated here in Figure 2-14.

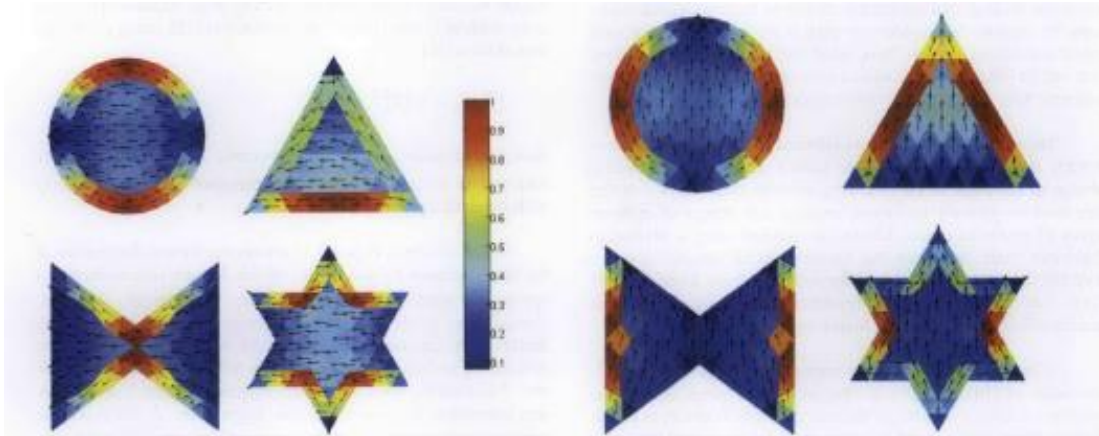


Figure 2-14 Characteristic modes for circle, triangle, bow tie and star [32], horizontal modes left, vertical modes right.

2.2.2 Characteristic Modes as Macro Basis Functions

Characteristic modes obtained from the eigen-solution of the MoM matrix, are very good candidates to be used as entire domain basis functions on each element since the actual current distribution on an antenna element is the superposition of its characteristic modes. Using characteristic modes as entire domain basis functions has already been proposed in [33] for the efficient analysis of large microstrip antenna arrays. In [33], the bi-static radar cross section of an array of printed patches is computed by using a truncated set of characteristic modes and accurate results are obtained. A similar strategy is pursued and examined in this study. However, this study departs from [33] by some critical aspects: First, the arrays under consideration are comprised of elements with a variety of sizes. Second, the possibility of using a single mode on each element is taken into consideration and it is shown that this approach yields accurate results with regard to the error in the far field. Finally, using a global characteristic mode for all elements in the array is investigated. The results obtained by example problems with different patch shapes and substrate properties show that it is actually convenient to use a single global CM for all differently sized elements, as far as the far field is concerned. In the forthcoming subsections the effects of using a truncated set of CMs on the accuracy of the method are demonstrated through numerical examples.

2.2.2.1 Using A Truncated Set of CMs

The formulation regarding the use of characteristic modes as macro basis functions is demonstrated through the MoM analysis of an isolated patch printed in a multi-layer medium. By applying Galerkin's MoM procedure with N RWG basis functions, the following matrix equation can be obtained:

$$\bar{\bar{Z}}_0 \bar{\alpha}_0 = \bar{V}_0 \quad (2-40)$$

where Z_{0ij} represent the weighted electric field at the i^{th} testing function due to the j^{th} basis function and V_{0i} is the weighted incident field at the location of i^{th} testing function. Vector $\bar{\alpha}_0$ corresponds to the unknown coefficients of the RWG basis functions. After constructing the $\bar{\bar{Z}}_0$ matrix, (2-36) is considered to study the characteristic modes (CM) of the printed patch.

The total number of modes is equal to N . Each eigenvector \bar{J}_n consists of the coefficients of the RWG basis functions for the corresponding mode. Since every CM extends throughout the surface of the element, they can be regarded as entire domain basis functions. Hence the unknown current can be expanded in terms of CMs instead of RWG basis functions. When CMs are used as basis functions and Galerkin's procedure is applied the following matrix equation is obtained:

$$\tilde{Z}_0 \bar{\beta}_0 = \tilde{V}_0 \quad (2-41)$$

where $\bar{\beta}_0$ is the unknown coefficient vector for characteristic modes. The relations between $\bar{\bar{Z}}_0$ and \tilde{Z}_0 , \bar{V}_0 and \tilde{V}_0 can be written by defining an eigencurrent matrix, $\bar{\bar{I}}_0$, such that each column of $\bar{\bar{I}}_0$ is the eigenvector \bar{J}_n . These relations are as follows:

$$\bar{\alpha}_0 = \bar{\bar{I}}_0 \bar{\beta}_0, \tilde{Z}_0 = \bar{\bar{I}}_0^H \bar{\bar{Z}}_0 \bar{\bar{I}}_0, \tilde{V}_0 = \bar{\bar{I}}_0^H \bar{V}_0 \quad (2-42)$$

It is clear that the sizes of the matrix equations in (2-40) and (2-42) remain same if all the characteristic modes are considered. However, when M ($M < N$) characteristic modes are used as basis functions, then the size of matrix $\bar{\bar{I}}_0$ becomes $N \times M$ and consequently the size of the matrix equation in (3) reduces to $M \times M$.

When this reduced order approximation is utilized for the analysis of an antenna

array with P **identical** elements, first an isolated element is analyzed to construct the \bar{I}_0 matrix, then (2-43) is solved to find the coefficients of the characteristic modes on each element ($M \times P$ unknowns).

$$\tilde{Z}\bar{\beta} = \tilde{V} \quad (2-43)$$

where \tilde{Z} , $\bar{\beta}$ and \tilde{V} are defined as in (2-44):

$$\bar{\alpha} = \bar{I}\bar{\beta}, \tilde{Z} = \bar{I}^H Z \bar{I}, \tilde{V} = \bar{I}^H \bar{V} \quad (2-44)$$

Although obvious, it is worth reminding that $\bar{\beta}$ is the solution of the reduced matrix system and it designates the coefficients that weight the characteristic modes on each element. For the array case, \bar{I} is a block diagonal matrix as:

$$\bar{I} = \begin{bmatrix} [\bar{I}_0]_{N \times M} & [\bar{0}]_{N \times M} & \cdot & [\bar{0}]_{N \times N} \\ \cdot & [\bar{I}_0]_{N \times M} & \cdot & \cdot \\ \cdot & \cdot & \cdot & \cdot \\ [\bar{0}]_{N \times M} & \cdot & \cdot & [\bar{I}_0]_{N \times M} \end{bmatrix}_{NP \times NP} \quad (2-45)$$

\bar{Z} should be organized so that each $N \times N$ block is a submatrix containing the interaction terms of two different patches, Z^{ij} or a patch with itself:

$$\bar{Z} = \begin{bmatrix} [\bar{Z}_{11}]_{N \times N} & [\bar{Z}^{12}]_{N \times N} & \cdot & [\bar{Z}^{1P}]_{N \times N} \\ \cdot & [\bar{Z}_{22}]_{N \times N} & \cdot & \cdot \\ \cdot & \cdot & \cdot & \cdot \\ [\bar{Z}^{P1}]_{N \times N} & \cdot & \cdot & [\bar{Z}_{PP}]_{N \times N} \end{bmatrix}_{NP \times NP} \quad (2-46)$$

On the other hand, when an array with non-identical elements, like a reflectarray consisting of a fixed shaped patch of different sizes, is considered, the CM analysis of the isolated patch should be repeated for each different element. In that case, \bar{I} becomes a matrix as given in (2-47), where it is assumed that the current on each element is expanded with a different number of basis functions (N_p). This would require carrying out the CM computation for all differently sized elements.

$$\bar{I} = \begin{bmatrix} [\bar{I}_1]_{N_1 \times M} & [\bar{0}]_{N_1 \times M} & \cdot & [\bar{0}]_{N_1 \times M} \\ \cdot & [\bar{I}_2]_{N_2 \times M} & \cdot & \cdot \\ \cdot & \cdot & \cdot & \cdot \\ [\bar{0}]_{N_P \times M} & \cdot & \cdot & [\bar{I}_P]_{N_P \times M} \end{bmatrix}_{\{\sum_{n=1}^P N_p\} \times MP} \quad (2-47)$$

2.2.2.2 Reusability of CMs

In order to avoid the repetition of eigenmode analysis, the possibility of using the same set of CMs for all the elements is explored. In this study, it is observed that the current distribution of a specific characteristic mode remains almost same as the size of the element changes. The eigenvectors of the two different size patches turn out to be almost equal to each other within a scaling constant if same number of basis functions is used on each patch with the same mesh structure. Therefore, the RWG mesh of one of the patches is chosen to be the scaled replica of the mesh applied to the other patch, as shown in Figure 2-15. Consequently, the eigenvectors computed for one patch could be utilized for the other patches as well. This is demonstrated through a MoM analysis of an example reflectarray of varying sized patches in a layered medium.

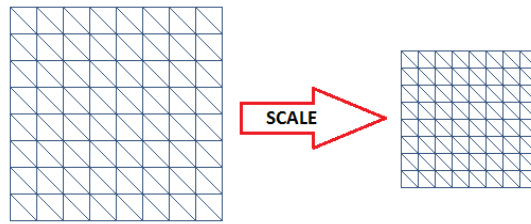


Figure 2-15 Mesh scaling

When same number of basis functions is used on all patches, \bar{I} takes the form:

$$\bar{I} = \begin{bmatrix} [\bar{I}_1]_{N \times M} & [\bar{0}]_{N \times M} & \cdot & [\bar{0}]_{N \times M} \\ \cdot & [\bar{I}_2]_{N \times M} & \cdot & \cdot \\ \cdot & \cdot & \cdot & \cdot \\ [\bar{0}]_{N \times M} & \cdot & \cdot & [\bar{I}_P]_{N \times M} \end{bmatrix}_{NP \times MP} \quad (2-48)$$

Furthermore, when the same set of CMs is used for all patches, I takes the form in:

$$\bar{\bar{I}} = \begin{bmatrix} [\bar{I}_0]_{N \times M} & [\bar{0}]_{N \times M} & \cdot & [\bar{0}]_{N \times M} \\ \cdot & [\bar{I}_0]_{N \times M} & \cdot & \cdot \\ \cdot & \cdot & \cdot & \cdot \\ [\bar{0}]_{N \times M} & \cdot & \cdot & [\bar{I}_0]_{N \times M} \end{bmatrix}_{NP \times MP} \quad (2-49)$$

where \bar{I}_0 represents the eigenmode matrix for a reference patch.

The usage of characteristic modes as MBFs is demonstrated with the analysis of an example reflectarray of varying sized patches in a layered medium. The reflectarray is designed such that it radiates a cosecant squared shaped beam in H-plane and a pencil shaped beam in E-plane when illuminated by a horn antenna with aperture dimensions $1.3\lambda_0 \times 0.58\lambda_0$ at a distance of $6.7\lambda_0$. The reflectarray is 16 elements wide and 10 elements high. The geometry of the reflectarray antenna can be viewed in Figure 2-16. The element spacing is assumed to be $0.6\lambda_0$ (18 mm) in both directions, frequency of operation is 10 GHz. The substrate has a relative permittivity of 4.2 and a thickness of 1.59 mm. First of all, the desired pattern is synthesized by a phase only synthesis technique [44], regarding the amplitude distribution on the reflectarray, generated by the feed antenna (Figure 2-18). Then the sizes of the patches are determined by the phase curve provided by the infinite array analysis. A representative layout of the array is depicted in Figure 2-17. The patch sizes vary between 2 mm to 12 mm. Each patch in the array is discretized into 176 RWG basis functions. Total number of unknowns for the conventional MoM approach is $160 \times 176 = 28160$. Resorting to single precision, the amount of memory required to store the classical impedance matrix is 5.9 GBytes (Base 2 definition).

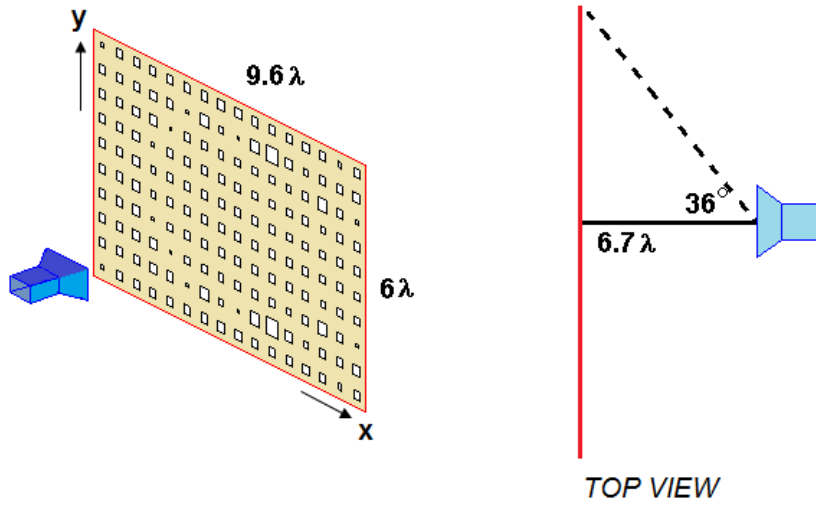


Figure 2-16 An illustration to define the reflectarray geometry.

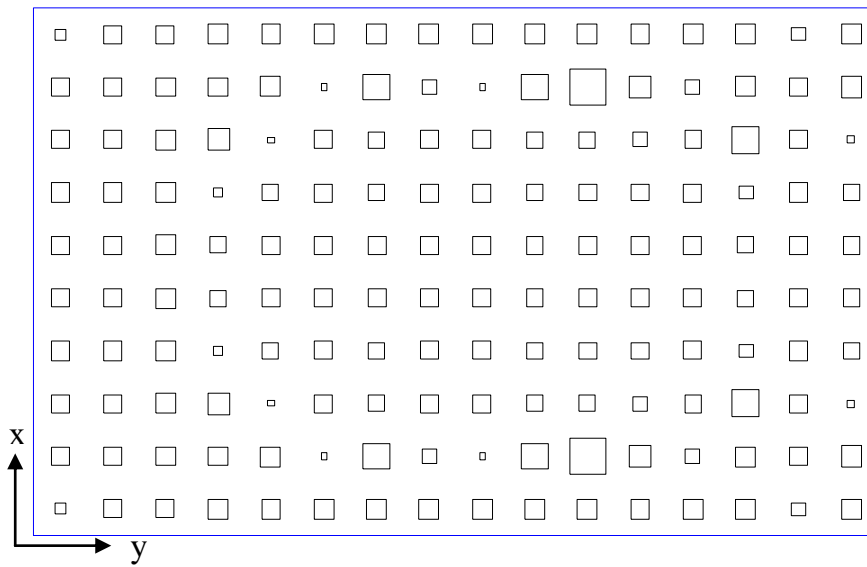


Figure 2-17 Layout of the reflectarray under concern.

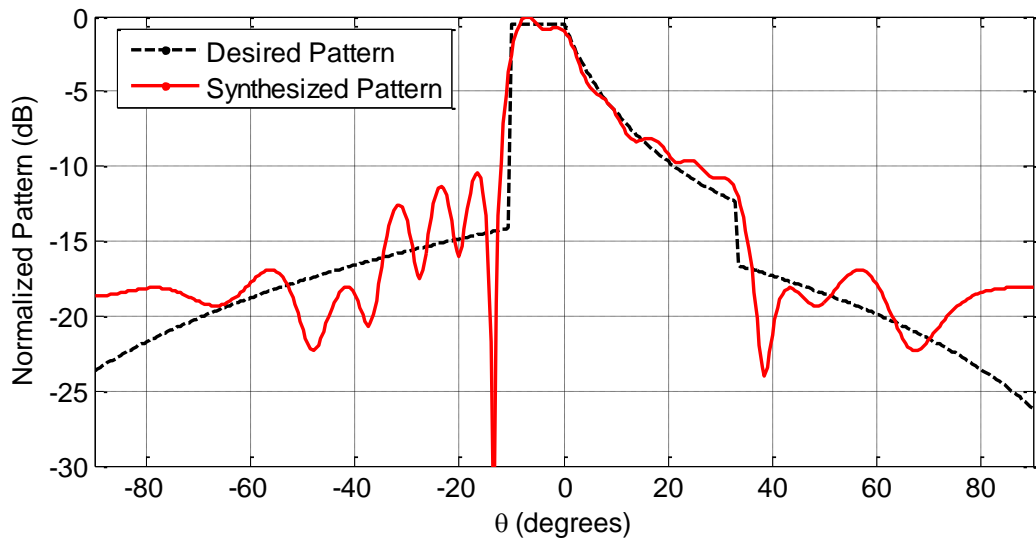


Figure 2-18 Desired and synthesized patterns.

The idea of using characteristic modes as MBFs is tested by various plane wave incidence scenarios, in order not to be misled by particular cases. The array is illuminated by plane waves with two different types of incidence as shown in Figure 2-19. The incidence planes are, $\varphi = 0^\circ$ in the first incidence case and $\varphi = 90^\circ$ in the second incidence case. The electric and magnetic field expressions are given in Table 2-4 for clarity. In both incidence cases, the tangential component of the electric field is along y direction.

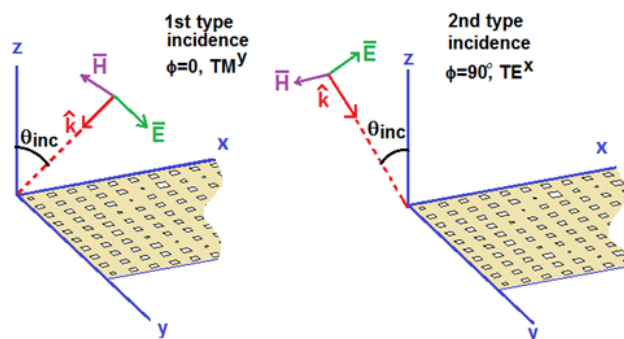


Figure 2-19 Definition of the first and the second type incidences.

Table 2-4 Electric and magnetic field expressions for first and second type incidences.

Incidence type	Electric field	Magnetic field
1 st	$\hat{y}E_0 e^{jk_x x + jk_z z}$	$\{-\cos(\theta_{inc})\hat{x} + \sin(\theta_{inc})\hat{z}\} \frac{E_0}{\eta} e^{jk_x x + jk_z z}$
2 nd	$\{\cos(\theta_{inc})\hat{y} + \sin(\theta_{inc})\hat{z}\} E_0 e^{-jk_y y + jk_z z}$	$\hat{x} \frac{-E_0}{\eta} e^{-jk_y y + jk_z z}$

For both incidence types, the incidence angle, θ_{inc} , is swept between 0 to 35 degrees, an interval that can be assumed a fair spectrum of incidence angles for a practical reflectarray illuminated by a feed antenna. First, the effect of truncating the CM set, i.e., taking $M < N$ is examined by observing the error in the current defined as in (2-50). At this stage, each element has its own CMs, that is to say, (2-48) is valid.

$$Error\ in\ Current = \frac{\sqrt{\sum_{n=1}^{N_{total}} |I_n^{approximate} - I_n^{exact}|^2}}{\sqrt{\sum_{n=1}^{N_{total}} |I_n^{exact}|^2}} \quad (2-50)$$

The effect of number of modes on the error can be observed on Figure 2-20 and Figure 2-21 for first and second type incidences respectively. It should be noted that, as the patch is a square one, there exists two degenerate characteristic modes with the same modal significance as shown in Figure 2-13. Hence, an exception is applied for the case where $M=1$, when observing the error in the current. A dominant mode is postulated by combining these two degenerate modes according to the excitation weights determined by V_n of (2-38) under the 0 degrees incidence conditions, for an isolated patch. Although amplitude of V_n for these degenerate modes should be equal in theory, a small imbalance occurs in practice, due to numerical nature of the solution approach.

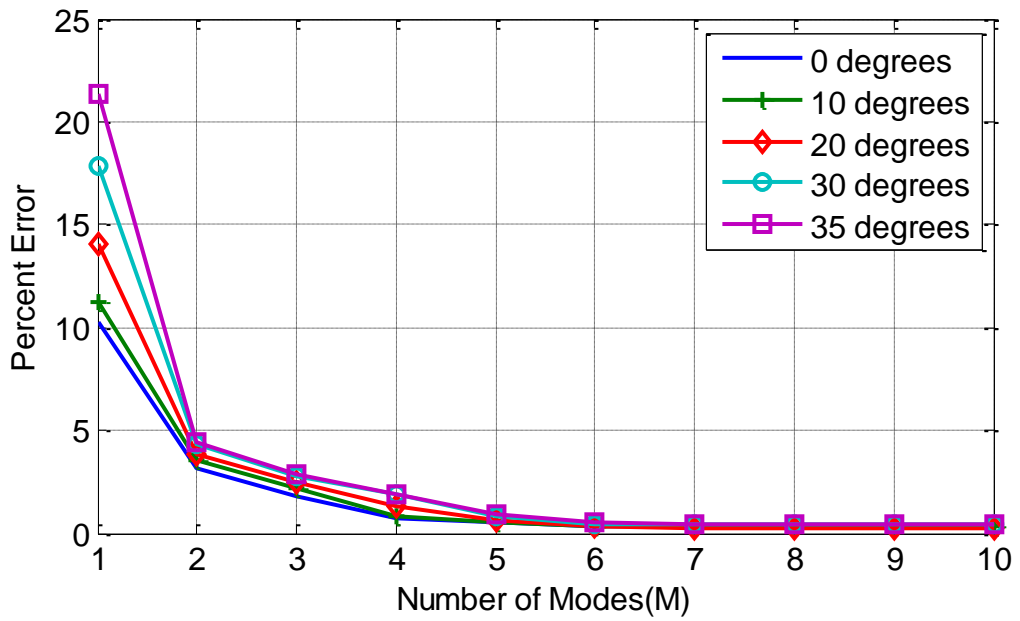


Figure 2-20 Error in current w.r.t. number of modes and incidence angle for 1st type incidence.

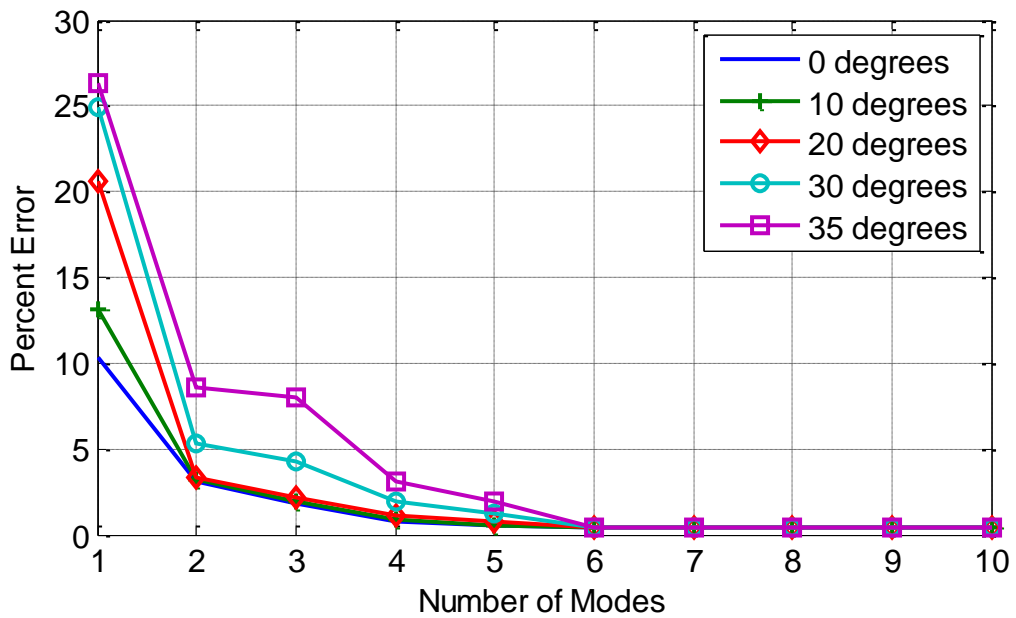


Figure 2-21 Error in current w.r.t. number of modes and incidence angle for 2nd type incidence.

At first glance, Figure 2-20 and Figure 2-21 propose that the number of modes should be chosen at least as 2. The reason of improvement in error for $M=2$ is due to the fact that the excitation coefficients of these modes are allowed to be independent of each other for that case. This enables a better representation of the patch current density when the patch is in an asymmetrical environment in terms of neighboring patches or in terms of excitation. However, when the far field is under concern, the agreement of the approximate solution with the conventional MoM solution is satisfactory even with a single mode. This can be observed in Figure 2-22, Figure 2-23, Figure 2-24, and Figure 2-25 where the far fields corresponding to the largest error (35 degrees incidence) is plotted. In all these figures, conventional MoM and 10 CMs yield almost the same result such that they cannot be distinguished in the graph. The far fields are due to patch currents only, ground scattered field is not included. Therefore, the phase is also of substantial importance since the far field due to patch currents and the far field due to ground scattering are added to find the overall radiation pattern.

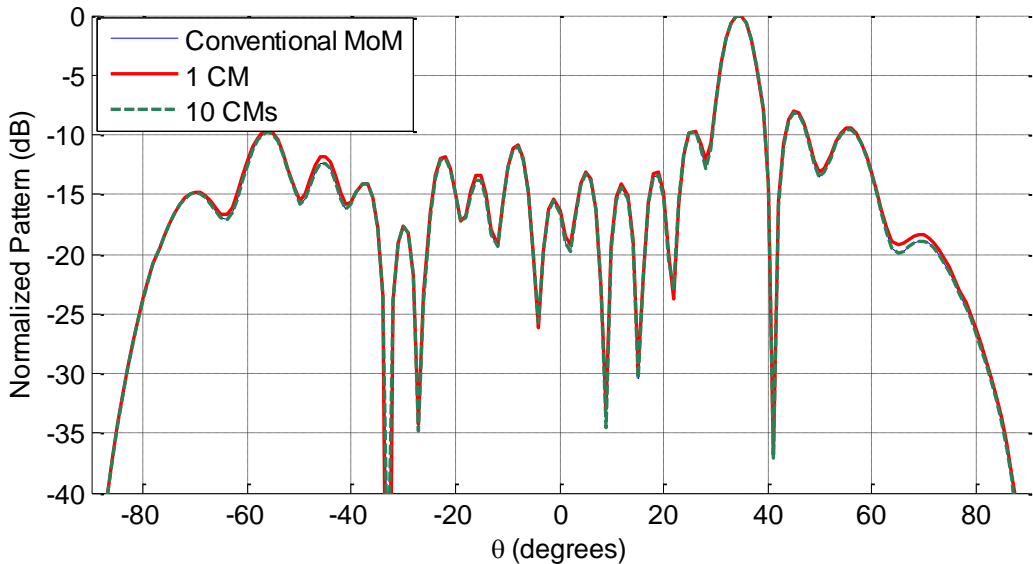


Figure 2-22 Comparison of the amplitude of far fields at $\phi=0$, computed by 1 and 10 characteristic modes (35 degrees, 1st type incidence, ϕ polarization).

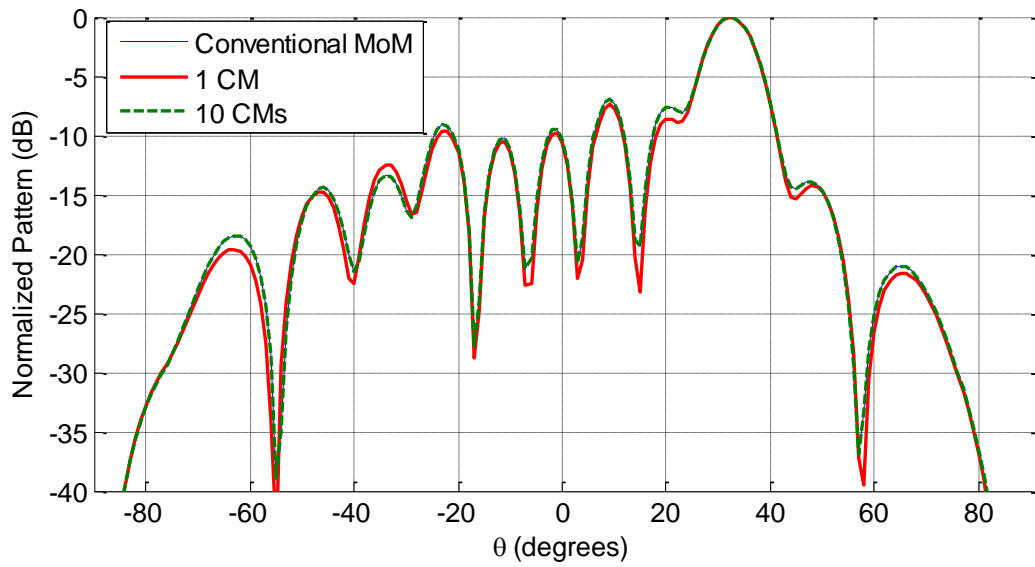


Figure 2-23 Comparison of the amplitude of far fields at $\varphi=90$, computed by 1 and 10 characteristic modes (35 degrees, 2nd type incidence, θ polarization).

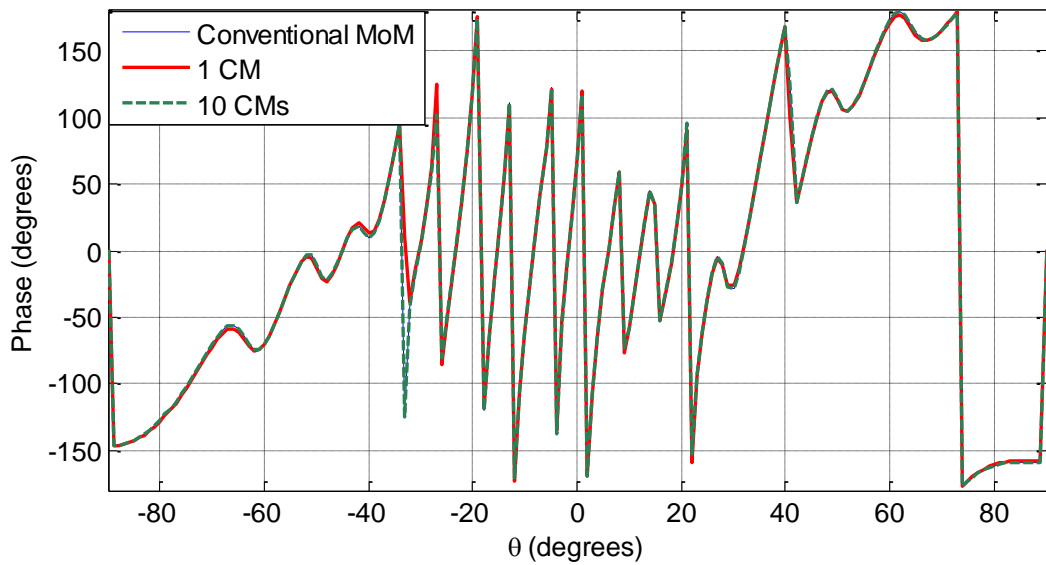


Figure 2-24 Comparison of the phase of far fields at $\varphi=0$, computed by 1 and 10 characteristic modes (35 degrees, 1st type incidence, φ polarization).

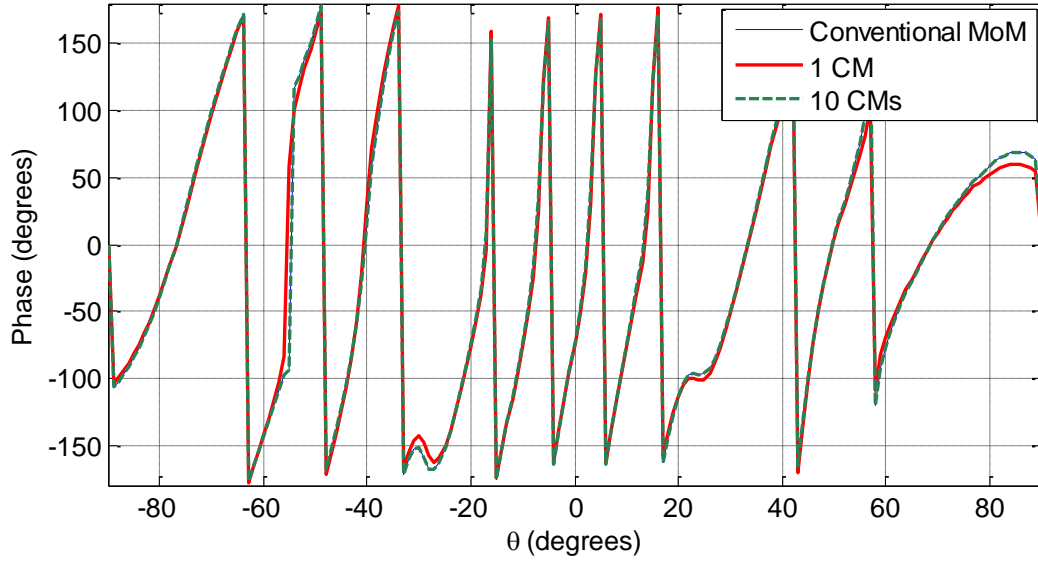


Figure 2-25 Comparison of the phase of far fields at $\varphi=90$, computed by 1 and 10 characteristic modes (35 degrees, 2nd type incidence, θ polarization).

Observing that a single mode is sufficient as far as the far field is concerned, investigations on applying (2-49) is conducted. The same reflectarray is analyzed for evaluating the usage of a global CM for all patches. For this purpose, the dominant characteristic mode of 61 different patches with sizes varying linearly between 4 mm and 10 mm is tried as a global CM. Thus I becomes as given in (2-51) and \tilde{Z} becomes a matrix of size 160×160 . The memory required to store \tilde{Z} is 200 Kbytes.

$$\bar{I} = \begin{bmatrix} [\bar{I}_0]_{N \times 1} & [\bar{0}]_{N \times 1} & \cdot & [\bar{0}]_{N \times 1} \\ \cdot & [\bar{I}_0]_{N \times 1} & \cdot & \cdot \\ \cdot & \cdot & \cdot & \cdot \\ [\bar{0}]_{N \times 1} & \cdot & \cdot & [\bar{I}_0]_{N \times 1} \end{bmatrix}_{NP \times M} \quad (2-51)$$

where $\bar{I}_0 = \bar{J}_1$ which represents the dominant mode of the reference patch. Each term of \tilde{Z} is expressed as in (2-52).

$$\tilde{Z}_{ij} = \bar{J}_1^T \tilde{Z}^{ij} \bar{J}_1 \quad (2-52)$$

The error in current obtained by using the dominant mode of each different size as a reference patch is calculated and presented in Figure 2-26 and Figure 2-27 for the first type and the second type incidences, respectively. It is worth mentioning that the

minimum error is observed for all examined incidence angles, when the reference patch size is 6.2 mm. On the other hand, Figure 2-28 is a plot of the variation of the real and imaginary parts of the input impedance of an isolated patch with respect to size. The plot, obtained from HFSS, shows that exact resonant patch length for this substrate properties ($\epsilon_r=4.2$ and $h=1.59$ mm) and frequency (10 GHz) is computed to be 6.17 mm. Therefore, it is concluded that minimum error is attained when the resonant patch is chosen as the reference patch. Figure 2-29 displays the error in the current as a function of incidence angle for this choice. Even though the resonance is very sensitive to size as seen in Figure 2-28, the error in current is tolerant for miscalculation of the resonant size. Hence, the size of the reference patch need not be calculated precisely.

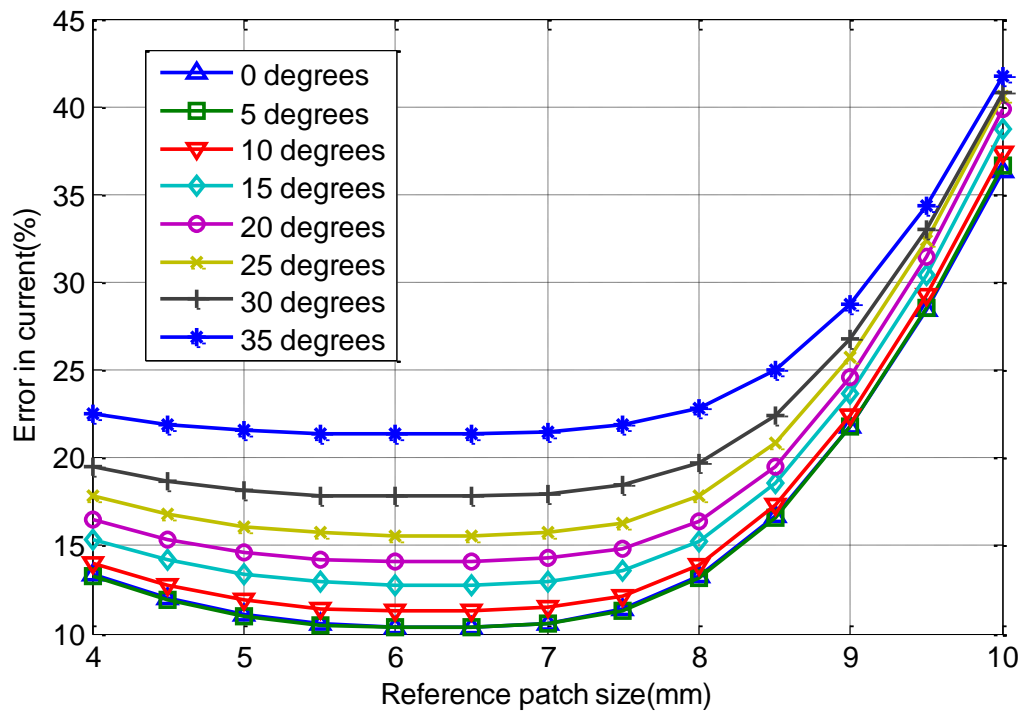


Figure 2-26 Variation of error in current w.r.t. reference patch size and incidence angle (1st type incidence).

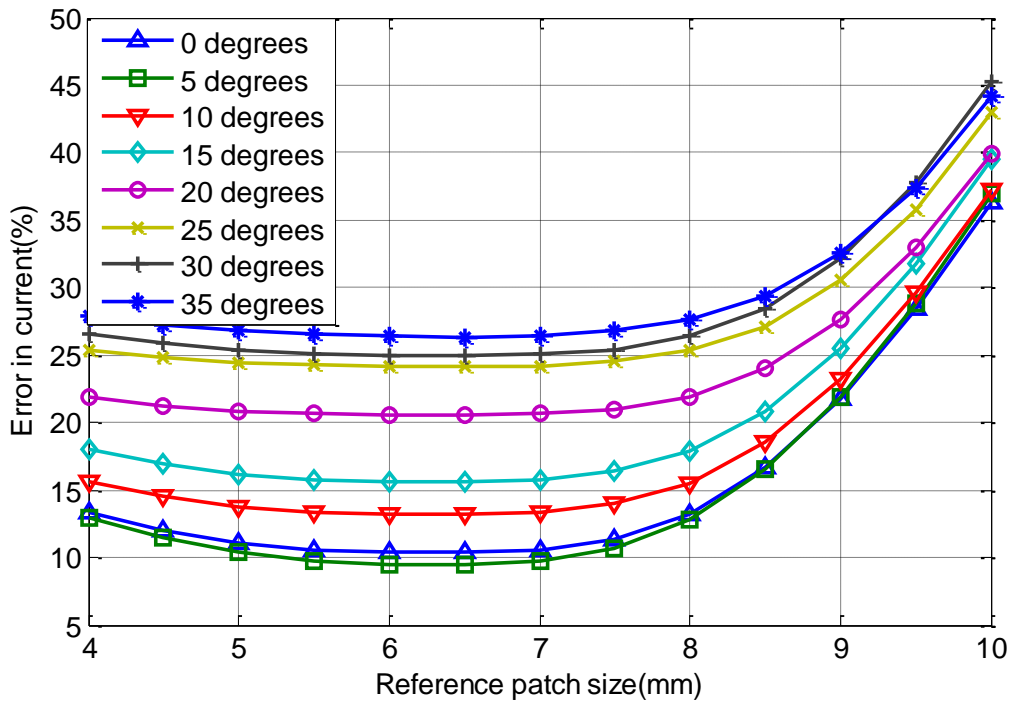


Figure 2-27 Variation of error in current w.r.t. reference patch size and incidence angle (2nd type incidence).

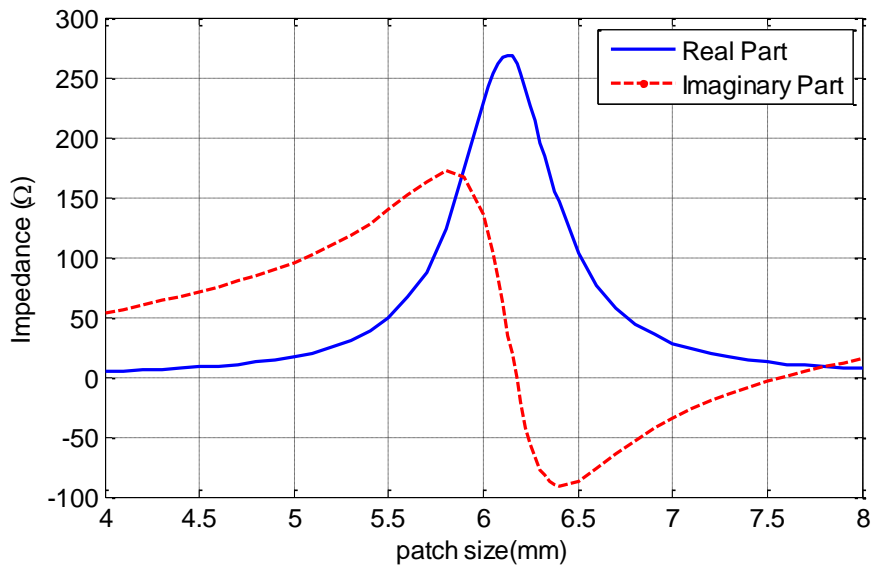


Figure 2-28 Real and imaginary parts of the input impedance of isolated patch.

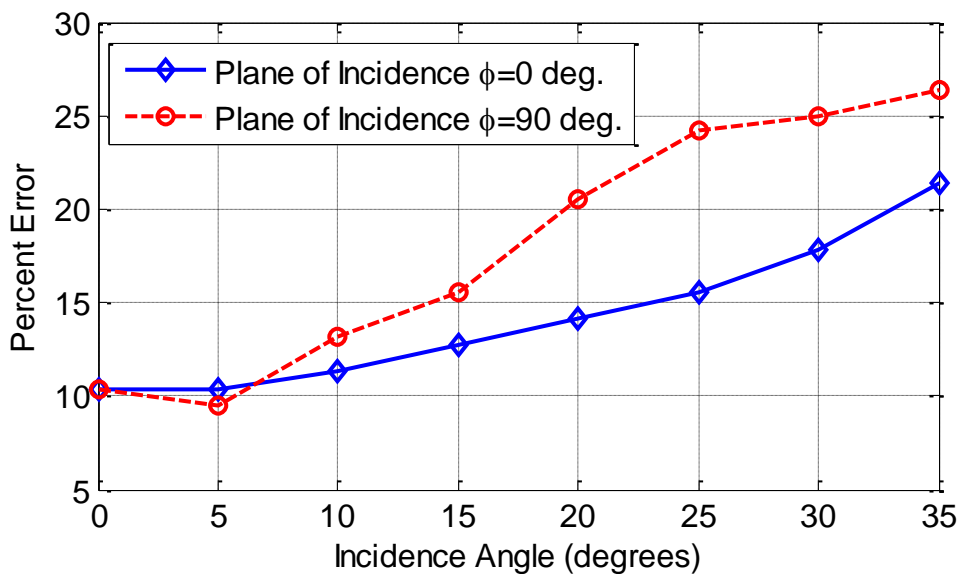


Figure 2-29 Variation of error in current w.r.t. incidence angle when the dominant mode of resonant patch is used as an MBF for all patches.

When the far field is computed by using this approximate current, the results shown in Figure 2-30 and Figure 2-31 are obtained.

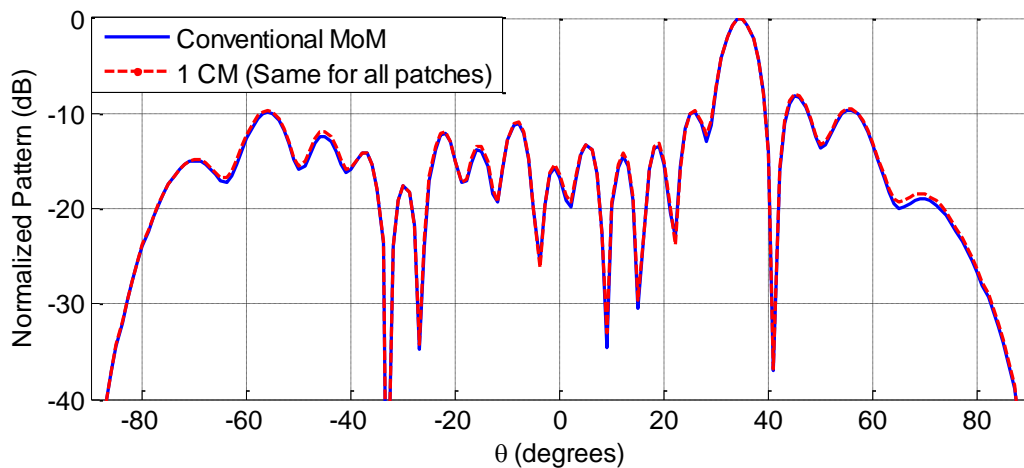


Figure 2-30 Comparison of far fields obtained by conventional MoM and reduced matrix solution with same CM for all patches (1st type incidence, φ polarization).

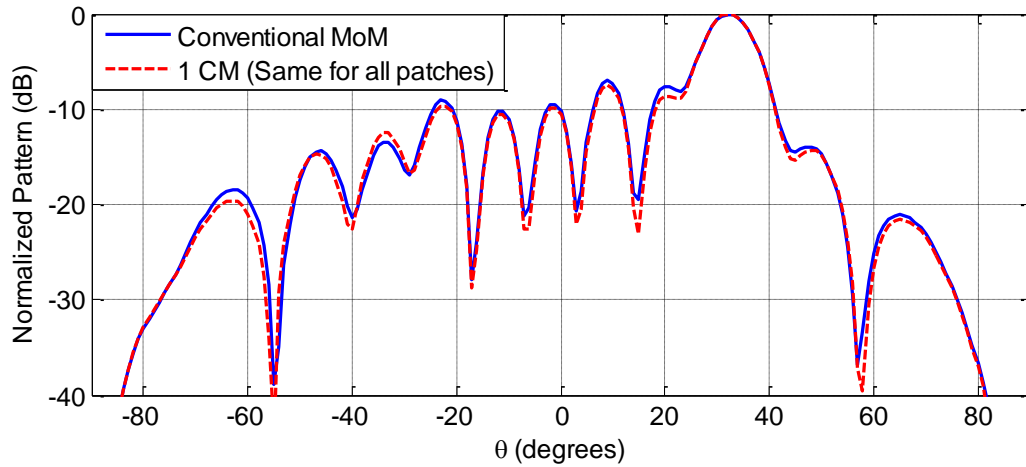


Figure 2-31 Comparison of far fields obtained by conventional MoM and reduced matrix solution with same CM for all patches (2nd type incidence, θ polarization).

Up to this point, it is demonstrated that using the dominant CM of the resonant patch as a MBF for all differently sized elements in a reflectarray, accurate results in terms of far field is obtained. In spite of large local discrepancies that possibly exist between the true current and the approximate current, far fields due to these currents are quite consistent, because of the stationary nature of the far field expressions. Due to brevity concerns, far field planes containing the specular angles are presented here, but other planes are also examined and the level of agreement is similar to that of the presented planes.

Considering the incidence angles in a practical excitation scenario, i.e., illumination by a feed antenna, almost no or very few of the elements are excited with incidence angles larger than 35 degrees. Even with larger incidence angles, graceful degradation is observed in the agreement between exact and approximate far field responses. Therefore it can be inferred that this approach shall also be successful in a practical reflectarray problem. Thus, the reflectarray antenna defined above is analyzed by conventional MoM and the proposed reduced matrix approach. It is assumed that the array and feed antenna are not interacting. The electric and magnetic fields at the aperture of the feed antenna are computed by HFSS and they are used to evaluate the incident field on the array. Far field of the array is computed

by adding the ground reflected field to the field radiated by the patch currents. The far fields in principal planes are given in Figure 2-32 and Figure 2-33.

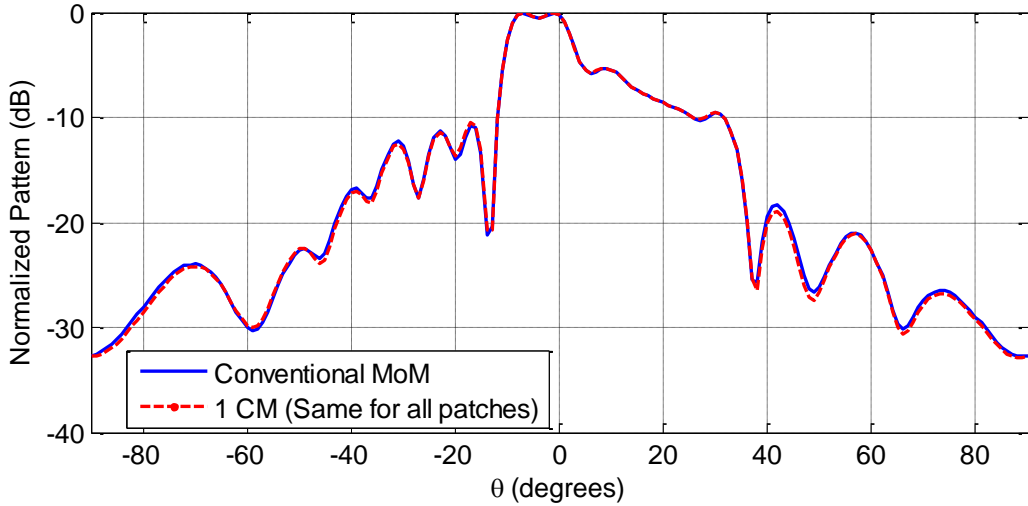


Figure 2-32 Comparison of the far fields of the reflectarray antenna computed by conventional MoM and proposed method, $\varphi = 0^\circ$ plane, φ polarization.

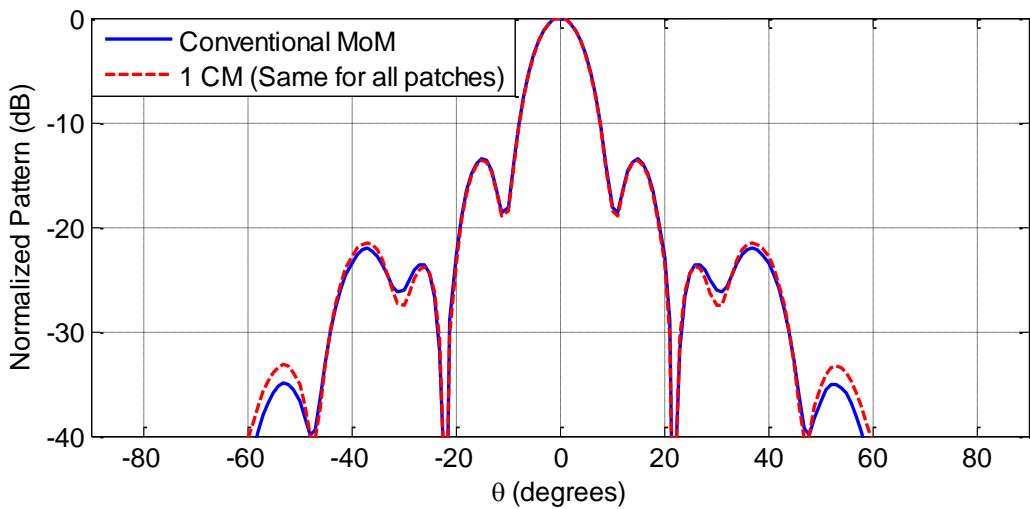


Figure 2-33 Comparison of the far fields of the reflectarray antenna computed by conventional MoM and proposed method, $\varphi = 90^\circ$ plane, θ polarization.

With the proposed method, the number of unknowns is drastically decreased but, it is still required to have the conventional impedance matrix to compute the reduced matrix $\tilde{\mathbf{Z}}$. Unfortunately, for large arrays, a considerable time and memory is required to fill the conventional impedance matrix. In the following parts, an efficient

technique to construct the reduced matrix $\tilde{\mathbf{Z}}$ without computing the $\bar{\mathbf{Z}}$ matrix is established.

2.3 An Efficient Method to Construct the Reduced Matrix

2.3.1 Investigations on Discarding Distant Interactions

If above mentioned MoM based analysis method is used in the design of reflectarrays with varying element sizes, the reduced MoM matrix given in (2-43) needs to be constructed several times for various element size combinations. To reduce the computation time, a tempting idea might be assuming that the matrix entries that correspond to two patches separated by a couple of blocks distance are diminishing. This would simplify the process to a great extent, but the level of coupling for a general substrate and element size combination might not necessarily allow that. For instance, for the 16×10 reflectarray defined in Section 0, the amplitude of the 90th row of the reduced matrix, which corresponds to interactions of all patches with the patch positioned at the 9th column, 10th row of the array is depicted in Figure 2-34. For better visualization, terms are properly arranged according to geometric positions of corresponding patches. If interactions beyond some neighborhood are ignored, many significant terms will be overlooked and a significant error in modal coefficients may occur. Furthermore, the terms do not monotonically decrease with distance because of variation of patch sizes on the array. Therefore, it is required to take all terms into consideration for a general case.

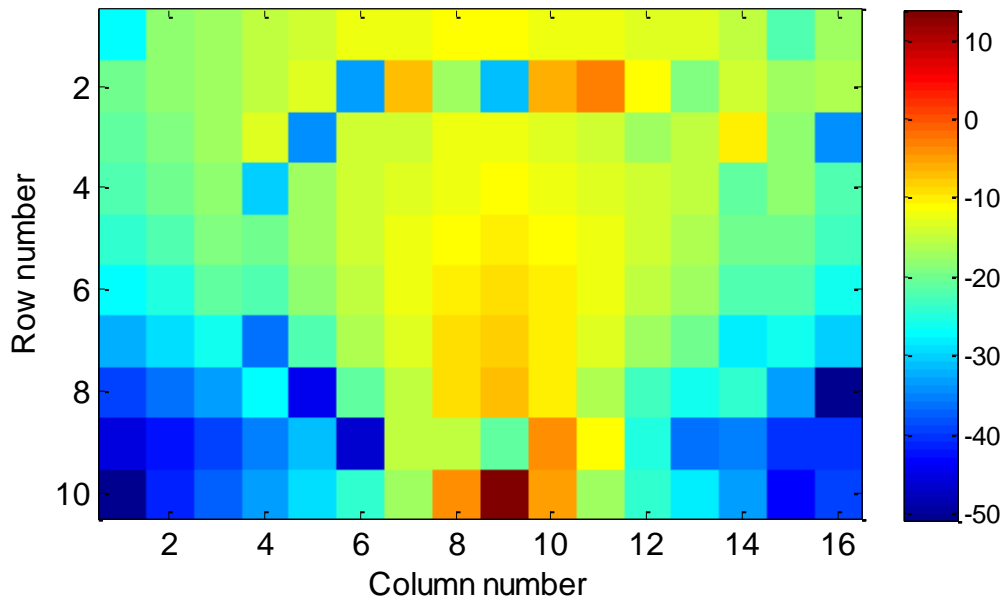


Figure 2-34 Log magnitude of 90th row of reduced matrix, properly arranged according to geometric positions of corresponding patches.

To observe the effect of discarding distant coupling on the current coefficients, two cases are analyzed:

- 1) The reduced matrix entries corresponding to interactions other than interactions between 1st neighbors (and self – interactions) are set to zero.
- 2) The reduced matrix entries corresponding to interactions other than interactions between 1st and 2nd neighbors (and self – interactions) are set to zero.

The definitions for 1st and 2nd neighborhoods are given in Figure 2-35.

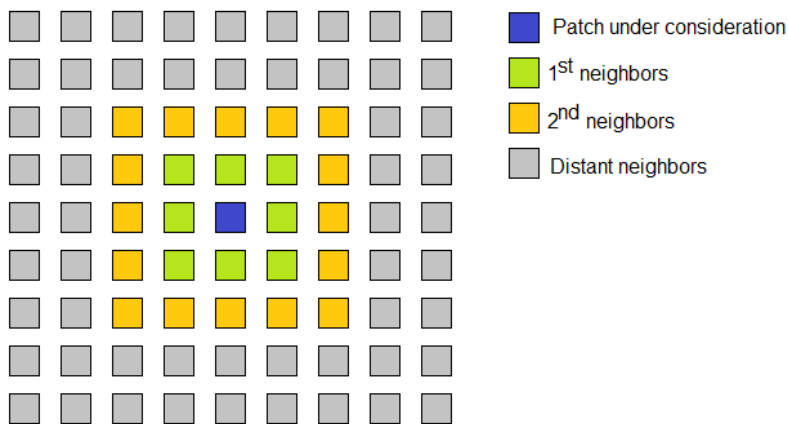


Figure 2-35 Explanation of different neighborhood types.

For these two cases, amplitude and phase of $\bar{\beta}$ defined in (2-43) is plotted and compared with the case where none of the interaction terms are ignored, in Figure 2-36 and Figure 2-37. The effect of ignoring distant terms on the far field pattern of the reflectarray is shown in Figure 2-38.

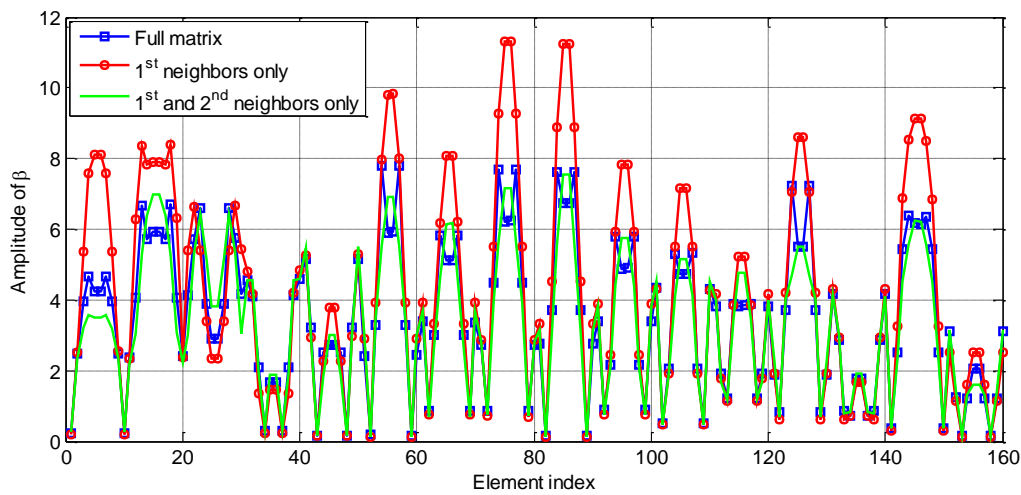


Figure 2-36 Effect of ignoring distant interactions on amplitude of β .

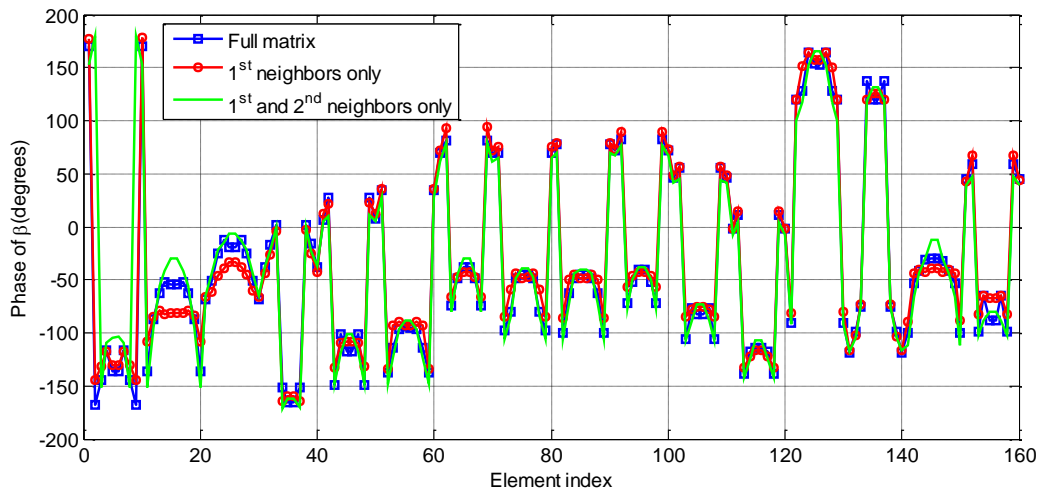


Figure 2-37 Effect of ignoring distant interactions on phase of β .

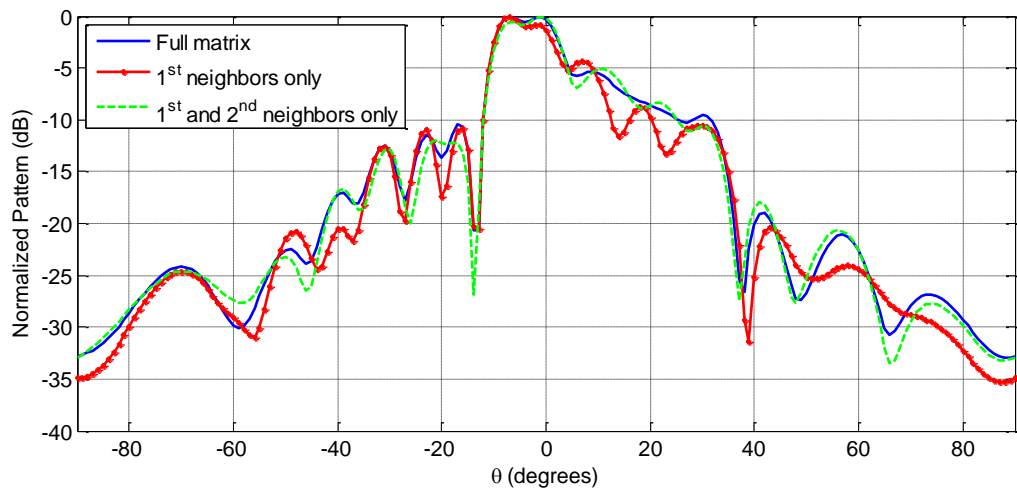


Figure 2-38 Effect of ignoring distant interactions on the far field of reflectarray,
 $\varphi = 0^\circ$ plane.

Although it seems that the inclusion of terms associated with 2nd neighborhoods helps converge to the actual $\bar{\beta}$ and actual far field, in order not to make the already existing approximation even less accurate, it is decided to take all entries of the reduced matrix.

2.3.2 Tabulation of Reduced Matrix Entries

In the design of reflectarrays, it is usually required to make a full wave analysis several times, in order to make sure that the design is performing as required. Depending on the number of elements in the array, the full wave analysis may be repeated many times. Keeping this in mind, it would be nice to have the reduced matrix term given in (2-52) as a closed form function. Unfortunately, this is not possible. On the other hand, it is obvious that \tilde{Z}_{ij} depends only on $\bar{\bar{Z}}^{ij}$ which is a function of:

- Horizontal displacement between i^{th} and j^{th} patches
- Vertical displacement between i^{th} and j^{th} patches
- Size of i^{th} patch
- Size of j^{th} patch.

At this point, the feasibility of tabulating the \tilde{Z}_{ij} for all combinations of the 4 variables defined above can be questioned. Nonetheless, this does not seem feasible for a large array. For instance, if there are 1000 patches in the array and 15 different values of patch sizes, the number of possible combinations is $1000 \times 15 \times 15 = 225000$.

In this study, it is observed that it is possible to circumvent this computational burden, because \tilde{Z}_{ij} for distant terms is almost separable into two functions, one in terms of two dimensional displacement between i^{th} and j^{th} patches, and the other in terms of sizes of i^{th} and j^{th} patches. That is to say,

$$\tilde{Z}_{ij} = \bar{J}_1^T \bar{\bar{Z}}^{ij} \bar{J}_1 = f(s_i, s_j, m, n) \cong g(s_i, s_j) \times h(m, n) \quad (2-53)$$

where $s_i, s_j, m,$ and n are defined in Figure 2-39. This brings in an order reduction in the tabulation, because instead of making as many simulations as the product of number of possible size combinations and number of possible displacement combinations, simulations as many as the sum of these numbers shall be sufficient. The separability can be qualitatively observed from Figure 2-40 and Figure 2-42. In Figure 2-40, amplitude of function f at 4 different instances of m and n is plotted whereas in Figure 2-42, amplitude of function f at 4 different instances of s_i and s_j

is plotted. As the 4 subplots are almost identical in each of these figures, it can be concluded that amplitude of f is almost separable. The phase plot given in Figure 2-41 reveals that when m and n are varied but s_i and s_j are fixed, the phase of the function f has a similar behavior for different m and n couples. Although all subplots do not look similar, the phase of the function f is almost constant for all source and observation patch sizes for a fixed displacement. Similarly, Figure 2-43 shows that when s_i and s_j are varied but m and n are fixed, the phase of the function f has a similar behavior for different s_i and s_j couples. Thus, having the phase of function f almost separable as well, the function f can be considered as separable for practical purposes.

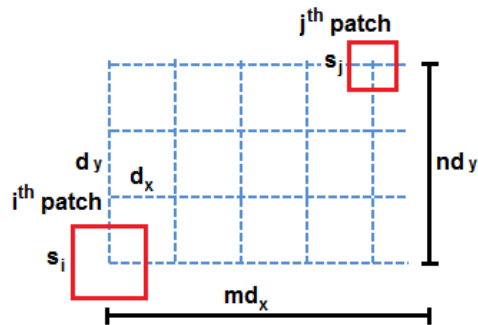


Figure 2-39 Definition of variables in (2-53).

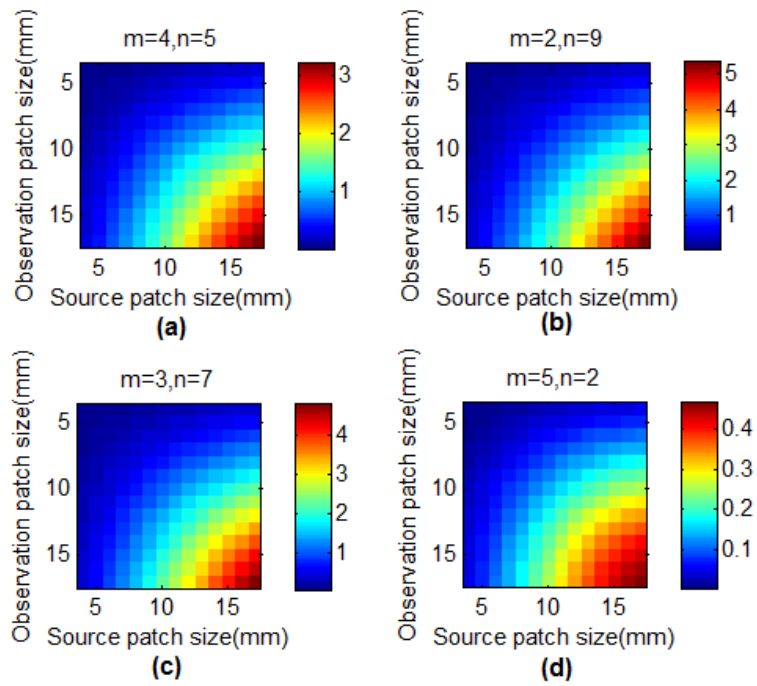


Figure 2-40 Amplitude of function f at various instances of m and n (a): $m=4, n=5$,
 (b): $m=2, n=9$, (c): $m=3, n=7$, (d): $m=5, n=2$.

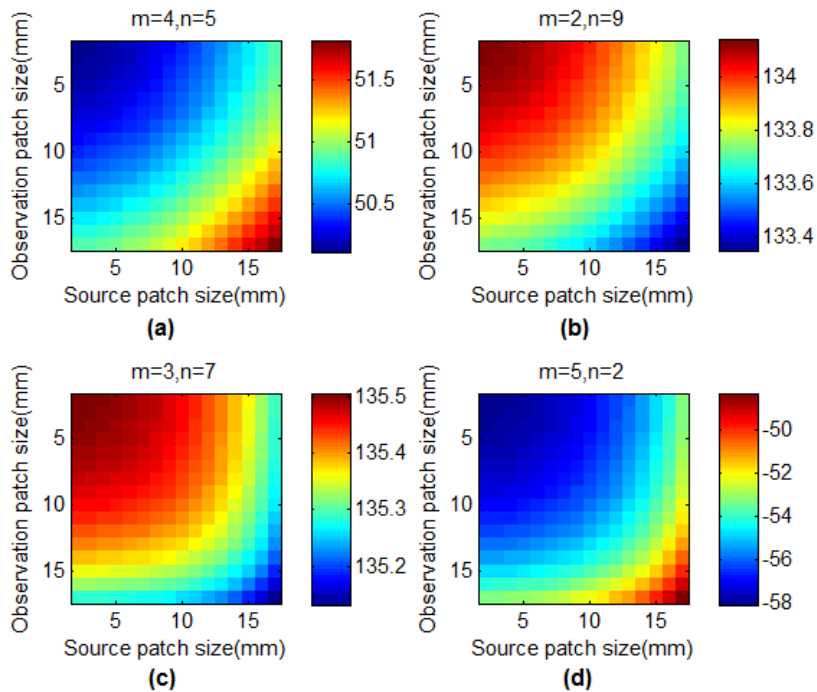


Figure 2-41 Phase (degrees) of function f at various instances of m and n (a):
 $m=4, n=5$, (b): $m=2, n=9$, (c): $m=3, n=7$, (d): $m=5, n=2$.

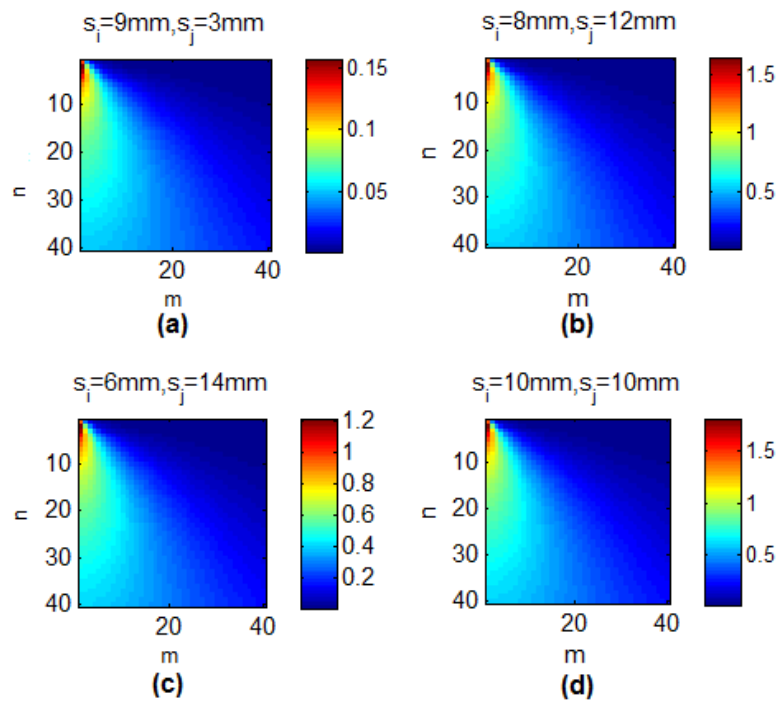


Figure 2-42 Amplitude of function f at various instances of s_i and s_j (a): $s_i=9\text{mm}$, $s_j=3\text{mm}$, (b): $s_i=8\text{mm}$, $s_j=12\text{mm}$, (c): $s_i=6\text{mm}$, $s_j=14\text{mm}$, (d): $s_i=10\text{mm}$ $s_j=10\text{mm}$.

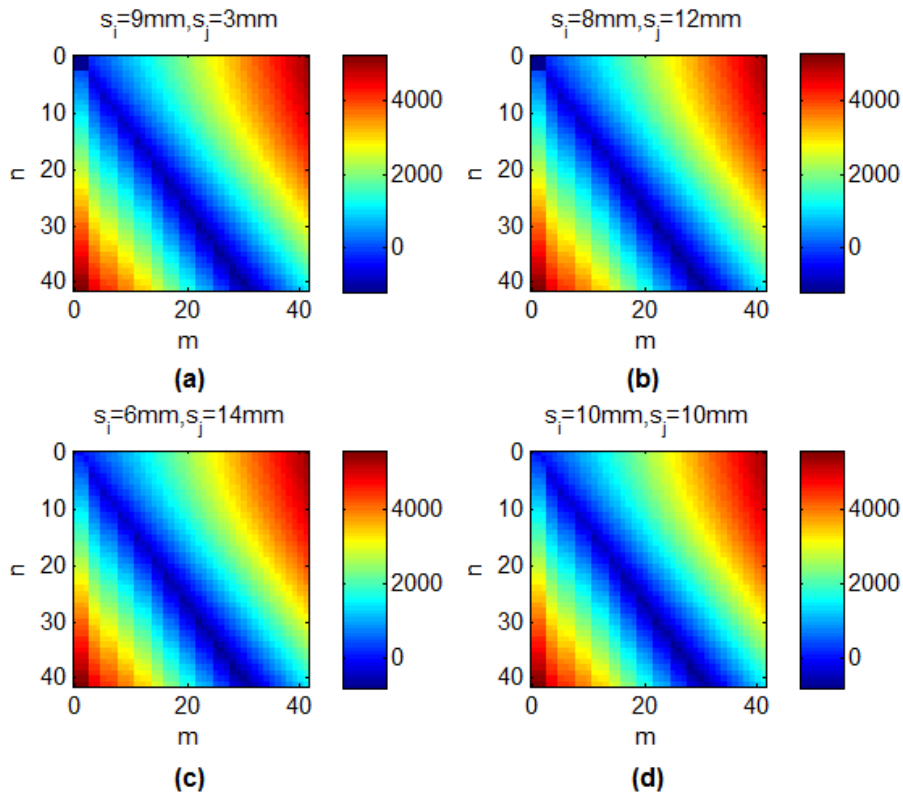


Figure 2-43 Phase (degrees, unwrapped) of function f at various instances of s_i and s_j (a): $s_i=9\text{mm}$, $s_j=3\text{mm}$, (b): $s_i=8\text{mm}$, $s_j=12\text{mm}$, (c): $s_i=6\text{mm}$, $s_j=14\text{mm}$, (d): $s_i=10\text{mm}$ $s_j=10\text{mm}$.

Due to separability, it becomes sufficient to make only two tabulations for distant patches: One for the two dimensional relative displacement for an average sized source and observation patches, $h(m, n)$, one for the sizes of source and observation patches for a fixed displacement, $g(s_i, s_j)$. As exemplified in Figure 2-34 and Figure 2-42, E – plane and H – plane coupling characteristics are quite different. Since the coupling in the E – plane is stronger; the characterization of function g should be performed for two patches displaced along E-plane to obtain better accuracy. Although the behavior of function f is different for E – plane and H – plane, the terms in reduced matrix \tilde{Z} corresponding to H – plane and near H – plane coupling are small enough for the matrix solution to tolerate large errors.

It is observed that the separability observation fails for closely positioned patches. This problem is handled by fully tabulating the function f for the first and second neighborhoods ($|m|, |n| \leq 2$) for all combinations of s_i and s_j . Note that it is sufficient to make this tabulation for 8 cases, due to symmetries.

In summary, it is required to make the following tabulations to have an accurate estimation of the reduced matrix:

1. Tabulation of function f at a sufficient number of discrete samples of s_i and s_j for $|m|, |n| \leq 2$. (Close neighbors)
2. Tabulation of function g at an arbitrary displacement (along E plane) at a sufficient number of discrete samples of s_i and s_j .
3. Tabulation of function h for $|m|, |n| > 2$ for two average size patches.

2.3.3 Computational Load

In this section, the computational complexity of total tabulation process will be discussed. Each phase of tabulation process is studied separately.

i. Tabulation of f for $|m|, |n| \leq 2$:

a) Self terms: This term represents the interaction of the patch with itself. The variation of this term by patch size for the considered substrate and frequency is given in Figure 2-44. Due to the resonance phenomenon that can be inferred from Figure 2-44, this term should be characterized with fine steps of patch size, especially in the resonance region. The step size can be determined by the phase curve of local periodicity approach because the sensitivity of this self-term with respect to size has the same characteristic with the phase curve. The minimum and the maximum patch sizes are also chosen from the phased design curve. For the example considered in this study, patch sizes are varying between 0.2 cm to 1.4 cm, and 121 different patch sizes are used for the tabulation of self-terms. It should be noted that this tabulation is done only once and it is independent of the array size and geometry.

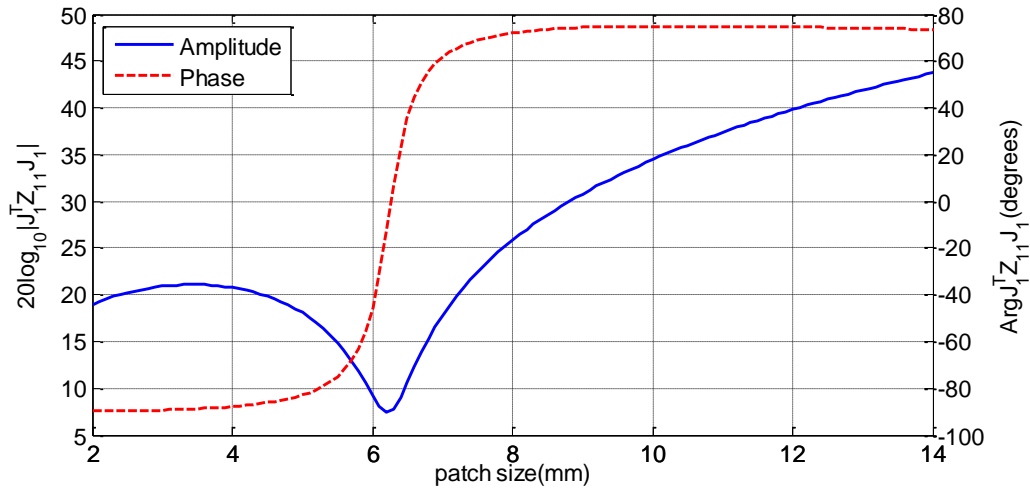


Figure 2-44 Phase and amplitude characteristic of $\bar{J}_1^T \bar{Z}^{11} \bar{J}_1$ w.r.t. patch size.

b) Close neighborhood: This function has a smoother characteristic than self-term. Therefore less number of sample points is sufficient for tabulation. The number of discrete samples for s_i and s_j can be chosen as low as 10-15 and intermediate values can be found by interpolation. If there are N_s size samples, instead of N_s^2 evaluations, $N_s(N_s + 1)/2$ evaluations can be performed by utilizing reciprocity. Note that even though this characterization is required for all first and second neighborhoods, it is sufficient to make this tabulation for 8 cases, due to symmetries. This tabulation phase is independent of the size of the array.

ii. Tabulation of function g : Tabulation of g with respect to s_i and s_j is same as the tabulation of f for close neighborhoods. The difference is that it is performed only once for two patches separated by a fixed distance.

iii. Tabulation of function h : Function h is calculated for all horizontal and vertical displacement combinations with fixed source and observer patch sizes. Although it does not make a significant difference, the fixed patch size is chosen to be the average value of the patch sizes considered for tabulations. The number of simulations in this tabulation phase depends on the array size. If the number of elements in the reflectarray is P , a total of $P-9$ simulations are performed, if no curve fitting on the characteristic is attempted.

To give a solid idea of the durations spent in tabulation phases, a 1000 element array is assumed. The platform is a personal computer with 3.3 GHz clock speed and Intel i5 series processor. The computation tool is developed in MATLAB with single precision arithmetic. For the considered substrate, frequency and element spacing, the tabulation takes the times indicated in Table 2-5. The computation of self-terms takes most of the time. Note that the long computation time to make the tabulation for function h is due to the large number of elements. It is worthwhile to underline the importance of efficiency provided via separability property by comparing the computation time achieved with separability ($0.5 \times (1000 + 66) = 533$ sec) to the computation time that would be required if separability was not exploited ($0.5 \times (1000 \times 66) = 33000$ sec).

Table 2-5 Computation times of tabulations for 1000 element array.

	<i>Number of repetitions</i>	<i>Time to compute</i> \bar{z}^{ij}	<i>Total time</i>
<i>Function f (self terms)</i>	121	7.5 s.	908 s
<i>Function f (close neighborhoods)</i>	$8 \times 11 \times 12 / 2$	0.5 s.	265 s
<i>Function g</i>	$11 \times 12 / 2 = 66$	0.5 s	33 s
<i>Function h</i>	~ 1000	0.5 s	500 s
<i>Total time</i>	1706 s ~ 28 min		

All tabulation steps are prone to parallelization and therefore can be accelerated in proportion to the degree of parallelization. Furthermore, no concern for efficiency is carried in this study to speed up above tabulations. To observe the required computation times for increasing number of array elements, the tabulation for function h is extended for a maximum size of 75 by 75 elements and Table 2-6 is filled experimentally. While filling the table, a single characteristic mode is assumed on all elements and single precision arithmetic is applied. It is seen that, as the number of elements increase, the total analysis time is governed by the matrix inversion process. Yet for reflectarrays with less than 5000 elements, the overall analysis time is less than 13.1 seconds.

Table 2-6 Computation times spent for reflectarrays with different number of elements.

<i>Number of elements</i>	<i>Matrix fill time (s)</i>	<i>Matrix inversion time(s)</i>	<i>Total time(s)</i>
500	0.05	0.08	0.13
1000	0.16	0.22	0.38
1500	0.31	0.6	0.91
2000	0.5	1.25	1.75
2500	0.8	2.1	2.9
3000	1	3.15	4.15
3500	1.45	4.5	5.95
4000	1.86	6.15	8.01
4500	2.28	8.08	10.36
5000	2.83	10.25	13.08

When tabulations are available, to analyze reflectarrays with arbitrary patch sizes, the only tasks to do are to construct the reduced matrix by table look up, to generate the right hand side vector $\tilde{V} = \bar{I}_0^H \bar{V}$, and solve $\tilde{Z}\beta = \tilde{V}$ to find $\bar{\beta}$. To reduce the calculation time of \tilde{V} , an approximation is used. This approximation relies on the fact that patch is always electrically small and centered on the same grid point regardless of its dimension. Therefore, the incident field value at that grid point can be assumed unchanged over the patch. Given the feed antenna, calculating the incident field values only at element centers in advance and taking it constant over the patch provides a good approximation of the actual incident field. Moreover, due to spatially scaled nature of the mesh, \tilde{V} values for different patch sizes can be easily computed by scaling.

The efficiency of the method is best appreciated when it is intended to analyze the effects of changes in the element sizes in the design of a reflectarray. Once the lookup tables are available, the computation time for the construction of the reduced matrix and excitation vector, and the solution of the resulting matrix equation is 0.38 seconds for a 1000 element array. In the following part, it is shown that the

proposed method outperforms a classical method in terms of resource usage and solution time, even for a single analysis.

2.3.4 A Large Reflectarray Problem Solved by Proposed Method

In order to demonstrate the successful application of the method to the analysis of a large reflectarray, the 30 x 30 reflectarray shown in Figure 2-45 is analyzed. This reflectarray is designed such that it has a cosecant squared fan beam along elevation. Substrate properties, frequency and spacing are same as those given in Section 0. The array is illuminated by the same feed antenna, located at $12\lambda_0 = 36$ cm. away from the array. The reference solution is conducted on a super computer with 512 CPUs by using HFSS. To minimize the electrical size of the problem, feed antenna and the reflectarray structure are solved separately. The number of tetrahedral elements used by HFSS is 6.619.984 and the memory used is 179 GBytes. The solution time is around 9 hours. The same array is solved by the proposed method using the tabulations. The tabulation period is slightly lower than that given in Table 2-5, because of the smaller size of this array. Then, it takes 0.33 seconds to obtain the current coefficients of the entire array. The far field patterns in principal planes can be viewed in Figure 2-46 and Figure 2-47. As seen, the two solutions are in good agreement with minor inconsistency in the azimuth sidelobes. The solution obtained by the proposed method would rather be compared by the conventional method of moments, but MATLAB was not available on the mentioned supercomputer at the time of writing.

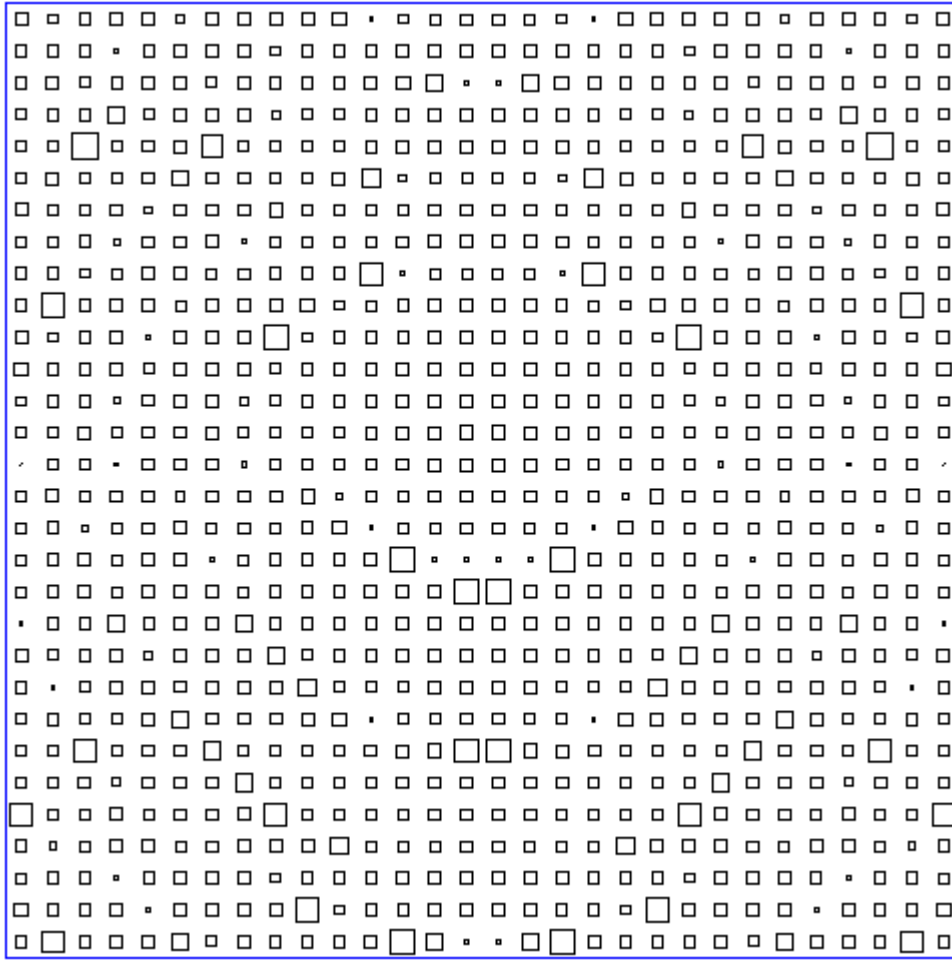


Figure 2-45 30×30 reflectarray.

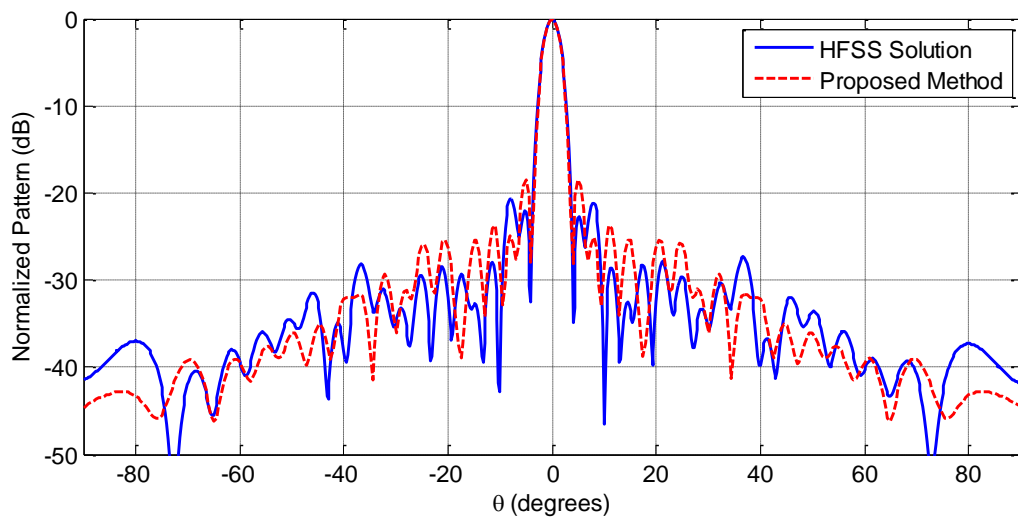


Figure 2-46 Azimuth pattern ($\varphi = 0^\circ$) of the 30×30 reflectarray computed by HFSS and the proposed method.

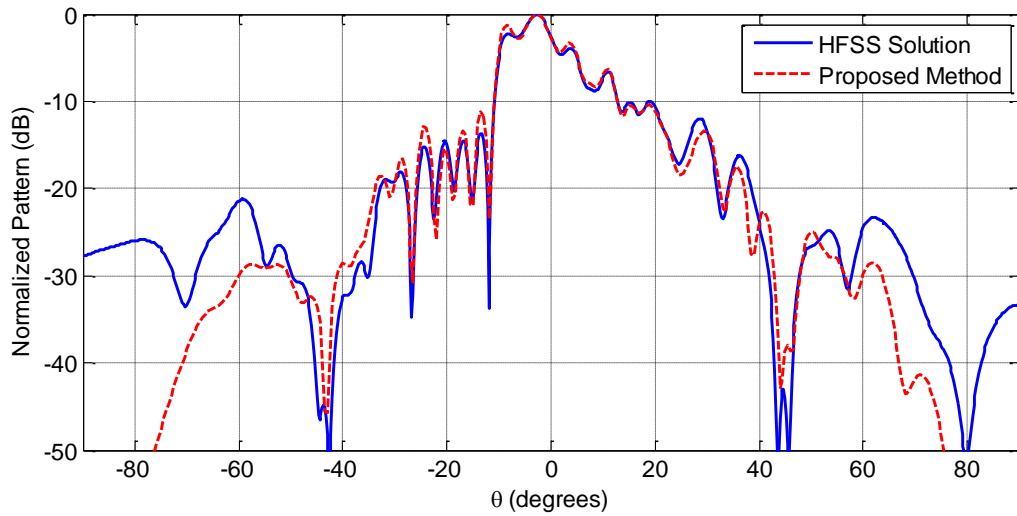


Figure 2-47 Elevation pattern ($\varphi = 90^\circ$) of the 30 x 30 reflectarray computed by HFSS and the proposed method.

In order to compare the accuracy of the method with the infinite array approach, the far fields expected by the infinite array approach is also calculated and compared to the HFSS result. For the infinite array approach, two different sub-approaches are investigated. In the first one, the variation of the reflection coefficient with incidence angle is discarded. In the second one, it is taken into account. The usual technique [35] for considering the incidence angle in literature can be summarized as follows:

- Obtain the reflection coefficients separately for transverse electric (TE) and transverse magnetic (TM) incidence, for the set of candidate element sizes.
- Decompose the incident electric field over the element centers into its TE and TM parts.
- Find the reflected field by superposing the reflected TE and reflected TM fields on each element.
- Compute the array factor using the complex reflected field data.
- It is optional to multiply the array factor with a suitable element pattern.

Figure 2-48 and Figure 2-49 are presented to compare the HFSS result with the far fields obtained by the above mentioned infinite array approaches. An element pattern proportional to the cosine of the angle from boresight is assumed and multiplied by

the array factors. The infinite array approach is actually quite successful when the incidence angle for each element is taken into consideration. However, it is observed that the proposed method is better in tracing the characteristics of the HFSS result, in spite of the dissimilar underlying numerical approaches.

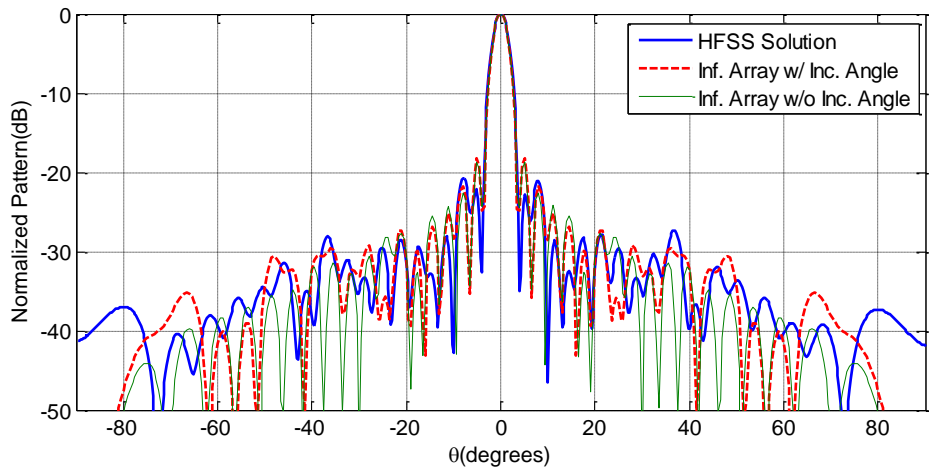


Figure 2-48 Azimuth pattern ($\varphi = 0^\circ$) of the 30 x 30 reflectarray computed by HFSS and the two infinite array approaches.

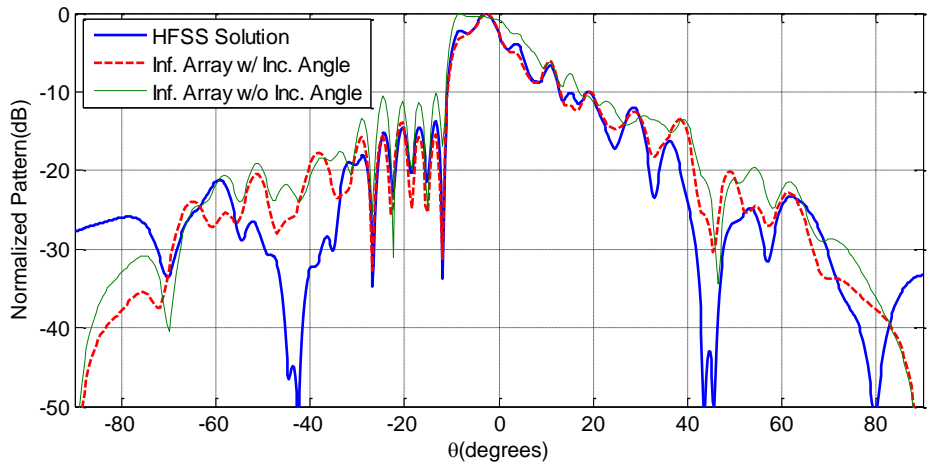


Figure 2-49 Elevation pattern ($\varphi = 90^\circ$) of the 30 x 30 reflectarray computed by HFSS and the two infinite array approaches.

2.3.5 Extension to Two Independent CMs

As offered by the observations in Section 2.2.2.1, it might be desirable to consider two characteristic modes per patch in order to enhance the accuracy of the reduced

matrix solution, or to be able to maintain accuracy under an arbitrarily polarized excitation. In this particular case $\bar{\bar{I}}$ matrix becomes:

$$\bar{\bar{I}} = \begin{bmatrix} [\bar{J}_1 \ \bar{J}_2]_{N \times 2} & [\bar{0}]_{N \times 2} & \cdot & [\bar{0}]_{N \times 2} \\ \cdot & [\bar{J}_1 \ \bar{J}_2]_{N \times 2} & \cdot & \cdot \\ \cdot & \cdot & \cdot & \cdot \\ [\bar{0}]_{N \times 2} & \cdot & \cdot & [\bar{J}_1 \ \bar{J}_2]_{N \times 2} \end{bmatrix}_{N \times 2P} \quad (2-54)$$

When $\bar{\bar{I}}$ is arranged as in (2-54), $\tilde{\bar{Z}}$ can again be visualized as composed of $\tilde{\bar{Z}}_{ij}$ s but this time it is constituted by 4 numbers:

$$\tilde{\bar{Z}}_{ij} = \begin{bmatrix} \bar{J}_1^T \bar{\bar{Z}}^{ij} \bar{J}_1 & \bar{J}_1^T \bar{\bar{Z}}^{ij} \bar{J}_2 \\ \bar{J}_2^T \bar{\bar{Z}}^{ij} \bar{J}_1 & \bar{J}_2^T \bar{\bar{Z}}^{ij} \bar{J}_2 \end{bmatrix} \quad (2-55)$$

In (2-54) and (2-55), \bar{J}_1 and \bar{J}_2 stand for the considered two CMs. The cost of taking two CMs is enlargement of the matrix $\tilde{\bar{Z}}$ by a factor of 2 in both dimensions. As far as the tabulation is concerned, the function g must be computed in the original strong coupling regions for the newly introduced terms $\bar{J}_1^T \bar{\bar{Z}}^{ij} \bar{J}_2$, $\bar{J}_2^T \bar{\bar{Z}}^{ij} \bar{J}_1$, and $\bar{J}_2^T \bar{\bar{Z}}^{ij} \bar{J}_2$. Other steps of the tabulation remain unchanged.

The first two characteristic modes for the square patch are shown in Figure 2-13. Note once again that, previously the sum of these two modes was taken as the dominant mode, \bar{J}_1 , as it would be a convenient MBF for y polarized incidence. However, Figure 2-20 and Figure 2-21 propose that taking two modes is better in terms of error in current. In spite of the fact that the two modes in Figure 2-20 and Figure 2-21 are diagonally oriented as seen in Figure 2-13, this is equivalent to taking one of the modes as y directed and the other x directed, which is preferred for simplicity. The x directed mode is created by taking the difference of the original two most significant characteristic modes of the resonant patch. With this choice of \bar{J}_1 and \bar{J}_2 , variations of $\bar{J}_1^T \bar{\bar{Z}}^{ij} \bar{J}_1$, $\bar{J}_1^T \bar{\bar{Z}}^{ij} \bar{J}_2$, $\bar{J}_2^T \bar{\bar{Z}}^{ij} \bar{J}_1$, and $\bar{J}_2^T \bar{\bar{Z}}^{ij} \bar{J}_2$ with m and n for $s_i=1$ and $s_j=1$ in Figure 2-50. The strong coupling regions for these terms can be inferred from this figure. It is also seen that $\bar{J}_1^T \bar{\bar{Z}}^{ij} \bar{J}_2$ and $\bar{J}_2^T \bar{\bar{Z}}^{ij} \bar{J}_1$ have the same characteristic, which is already expected by:

$$\bar{J}_2^T \bar{Z}^{ij} \bar{J}_1 = [\bar{J}_2^T \bar{Z}^{ij} \bar{J}_1]^T = \bar{J}_1^T \bar{Z}^{ij^T} \bar{J}_2 \cong \bar{J}_1^T \bar{Z}^{ij} \bar{J}_2 \quad (2-56)$$

The reason for the approximate equivalence (rather than exact) stems from the approximation in computation of the integrals associated with Galerkin's method, as reported in [37].

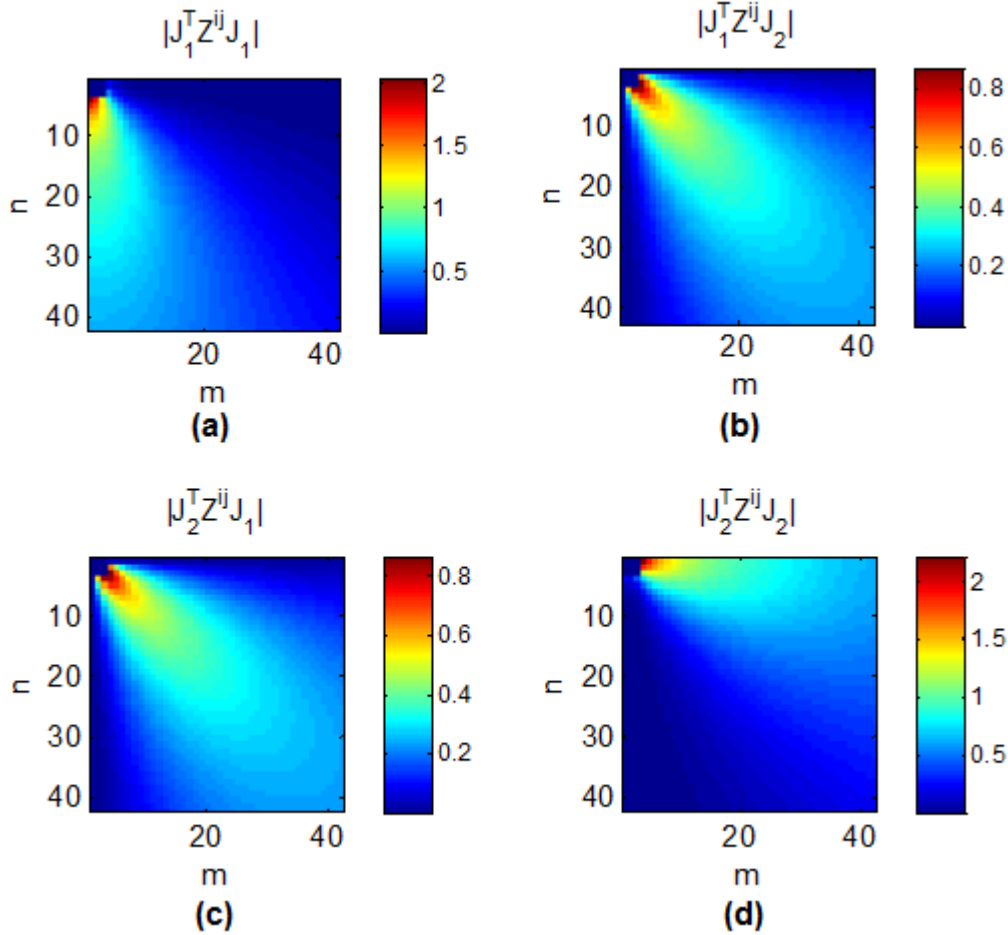


Figure 2-50 Amplitude of terms in \tilde{Z}_{ij} (a): $\bar{J}_1^T \bar{Z}^{ij} \bar{J}_1$, (b): $\bar{J}_1^T \bar{Z}^{ij} \bar{J}_2$, (c): $\bar{J}_2^T \bar{Z}^{ij} \bar{J}_1$, (d): $\bar{J}_2^T \bar{Z}^{ij} \bar{J}_2$.

In addition to Figure 2-50, it is observed that the whole separability argument of the Section 2.3.2 applies for all 4 terms defined in (2-55). The 16 x 10 array is considered once more with two modes. This time the size of the matrix \tilde{Z} is 320 x 320, where each odd column and row corresponds to the 1st mode and each even column and row corresponds to the 2nd mode. For instance, the 179th and 180th columns contain all the terms associated with 90th element as explained below:

- Every other row of 179th column starting from 1st row correspond to $\bar{J}_1^T \bar{Z}^{90} j \bar{J}_1$
- Every other row of 179th column starting from 2nd row correspond to $\bar{J}_1^T \bar{Z}^{90} j \bar{J}_2$
- Every other row of 180th column starting from 1st row correspond to $\bar{J}_2^T \bar{Z}^{90} j \bar{J}_1$
- Every other row of 180th column starting from 2nd row correspond to $\bar{J}_2^T \bar{Z}^{90} j \bar{J}_2$

The amplitudes of 179th and 180th columns are plotted in Figure 2-51 and Figure 2-52 to demonstrate the performance of separability. The terms calculated by full MoM matrix are almost indistinguishable from those calculated by separability. This agreement implies that when the reduced matrix is calculated by separability, the level of error will be lowered to the levels observed at M=2 in Figure 2-20 and Figure 2-21 just like it would when the reduced matrix is calculated by using the full MoM matrix.

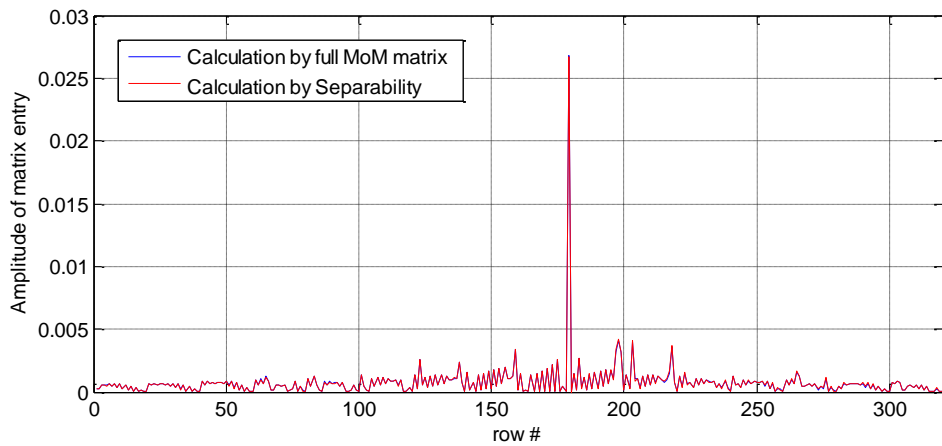


Figure 2-51 Amplitude of the 179th column of the 320x320 \bar{Z} matrix.

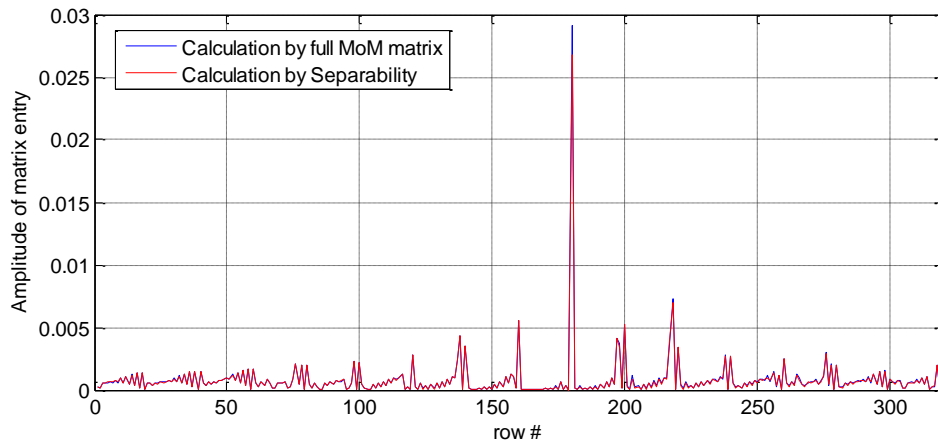


Figure 2-52 Amplitude of the 180th column of the 320x320 \tilde{Z} matrix.

CHAPTER 3

APPLICATION OF THE FAST ANALYSIS METHOD FOR VARIOUS ELEMENT TYPES

In this chapter, proposed fast analysis method is extended for patch shapes other than square. As a case study, circular patch is examined and it is seen circular patch is as amenable as the square patch to the proposed technique. On the other hand most patch shapes introduce hardly any advantage over the square patch although they are aesthetically pleasing. Therefore, the results obtained with the circular patch are not presented, but patch shapes that introduce some kind of specific advantage are investigated. For instance, square patch with an outer ring as a wideband element and split ring resonator that is used to implement element rotation method are examined in Section 3.1 and Section 3.2, respectively. Throughout this chapter, the far field patterns are those due to the patch currents only.

3.1 Square Patch with Outer Ring

Most of the practical patch shapes are basically resonant structures and therefore has a very sharp phase variation with dimensions. This results in two complications: First, the reflectarray pattern becomes sensitive to manufacturing errors. Second, the reflection phase changes very rapidly with frequency and therefore the bandwidth of the reflectarray becomes quite narrow. To alleviate these problems, structures that exhibit a linear phase behavior with respect to dimensions are proposed. These types of elements actually decrease the sensitivity of the pattern to manufacturing errors but do not fully overcome the bandwidth problem, because the phase response of the element is not the only limiting factor for the bandwidth. Even with this type of elements, the variation of the electrical distance of each element on the reflectarray to the feed antenna with frequency remains as a problem. Still, elements that provide linear phase shift offer a better bandwidth performance than resonant type elements

especially when the reflectarray surface is modified to decrease the effect of phase variation with frequency. An example of this type of element is offered in [45]. The element consists of an ordinary square patch and a square outer ring. The dimensions of the element are shown in Figure 3-1. The patch and outer ring dimensions are not independent, i.e., $L_2 = 0.75L_1$ and the thickness of the outer ring is $0.05L_1$. The substrate thickness is 3.175 mm and the relative permittivity is 2.33. The bandwidth of operation is between 11 and 13 GHz. When L_1 is swept between 4 and 8 mm, the reflection phase of this element (in infinite array environment) is observed as given in Figure 3-2.

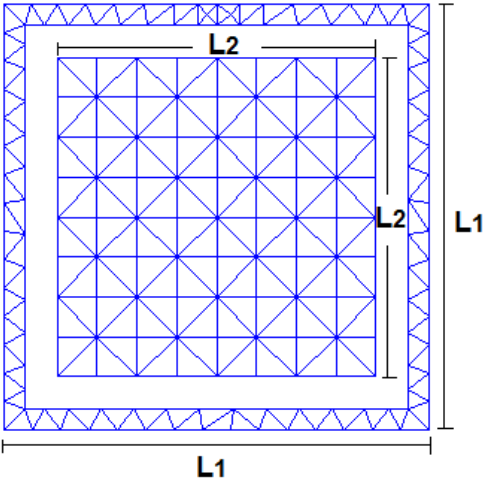


Figure 3-1 Square patch with outer ring [45].

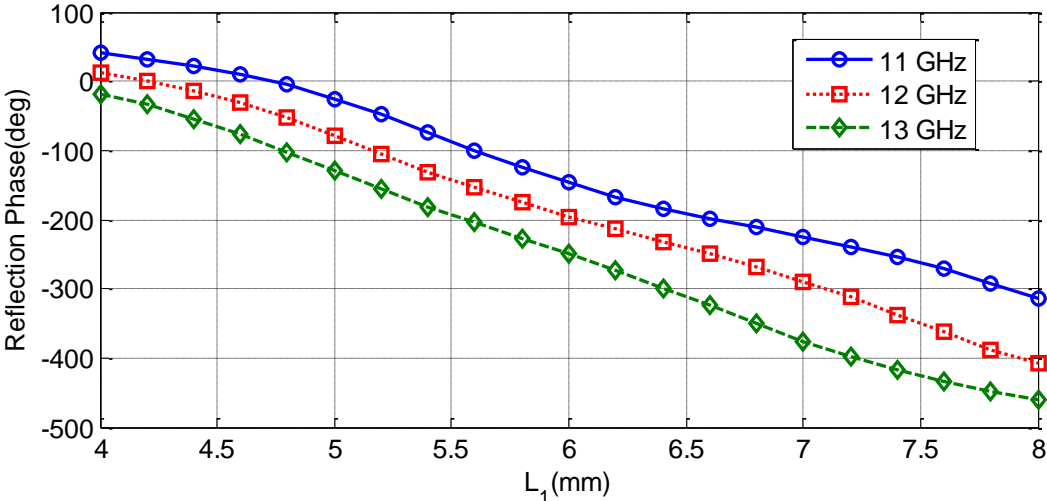


Figure 3-2 The phase characteristic of the proposed element with respect to L_1 and frequency [45].

The distinctive property of this element is that it is not a resonant one, despite it is composed of two resonant elements. Therefore the reusability concept of the previous chapter needs to be revised. The investigations on this element show that when the individual dominant characteristic modes of the two metallizations are considered for reuse, a good accuracy in the far field pattern is obtained. At 12 GHz, the resonance of the square patch occurs for $L_2=6.04$ mm, whereas the resonance for the square ring occurs for $L_1=5$ mm. The two most significant characteristic modes of the resonant square patch is similar to that given in Figure 2-13. Therefore the dominant mode is constructed as the sum of these two modes. The dominant characteristic mode of the resonant outer ring is given in Figure 3-3.

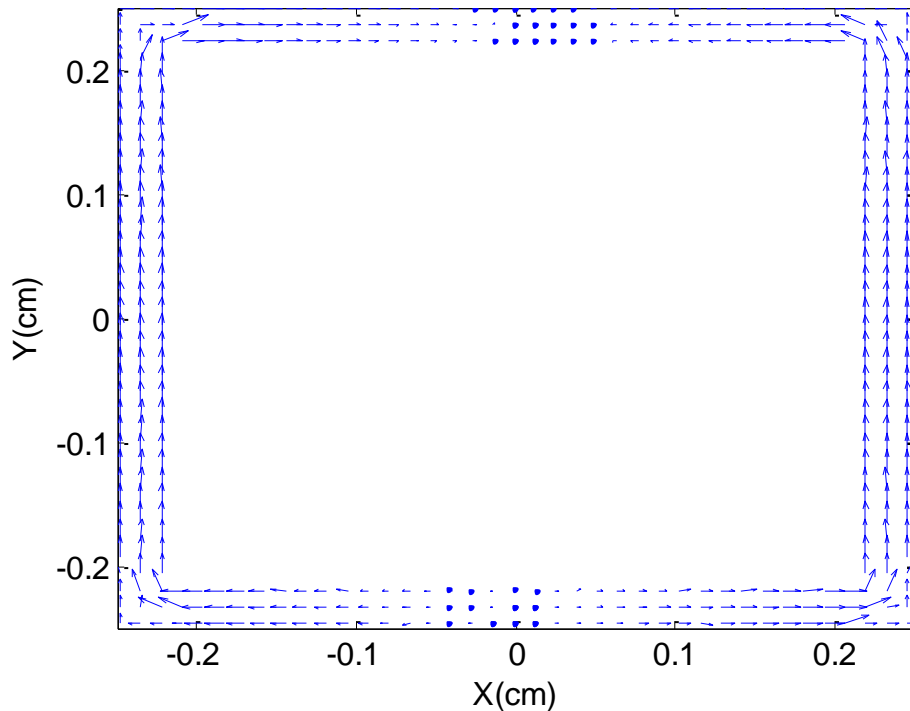


Figure 3-3 Dominant characteristic mode of the square ring.

3.1.1 Reusability of CMs

In order to investigate the feasibility of the characteristic mode reusability, a 9×9 reflectarray with random sized elements is generated. In this array, dimension L_1 of elements is varying randomly between 4 and 8 mm. Frequency of operation is assumed to be 12 GHz. A representative figure of the reflectarray is given in Figure

3-4. Each element is discretized by 287 RWG basis functions where 111 of these basis functions are defined on the square ring and the remaining 176 basis functions are defined on the square patch. This reflectarray is illuminated with plane waves of various angles with two different types of incidences defined in Section 2, and analyzed for each case with conventional MoM. Then an approximate solution is found by using (2-49). Two different macro basis functions \bar{J}_1 and \bar{J}_2 are defined, both of which extend all over the domain. The first basis function, \bar{J}_1 , is defined to be equal to the dominant CM of the resonant square ring over the corresponding part of the domain and zero over the rest of the domain (patch). Similarly, the second basis function, \bar{J}_2 , is defined to be equal to the dominant CM of the square patch over the corresponding part of the domain and zero over the rest of the domain (ring). Thus, these two MBFs are in a form suitable for use in the formulation. The numbering of the original RWG basis functions start on the ring part and therefore \bar{J}_1 and \bar{J}_2 are arranged as in (3-1), where \bar{J}^{ring} and \bar{J}^{patch} stand for the dominant CMs of the resonant ring and resonant patch respectively.

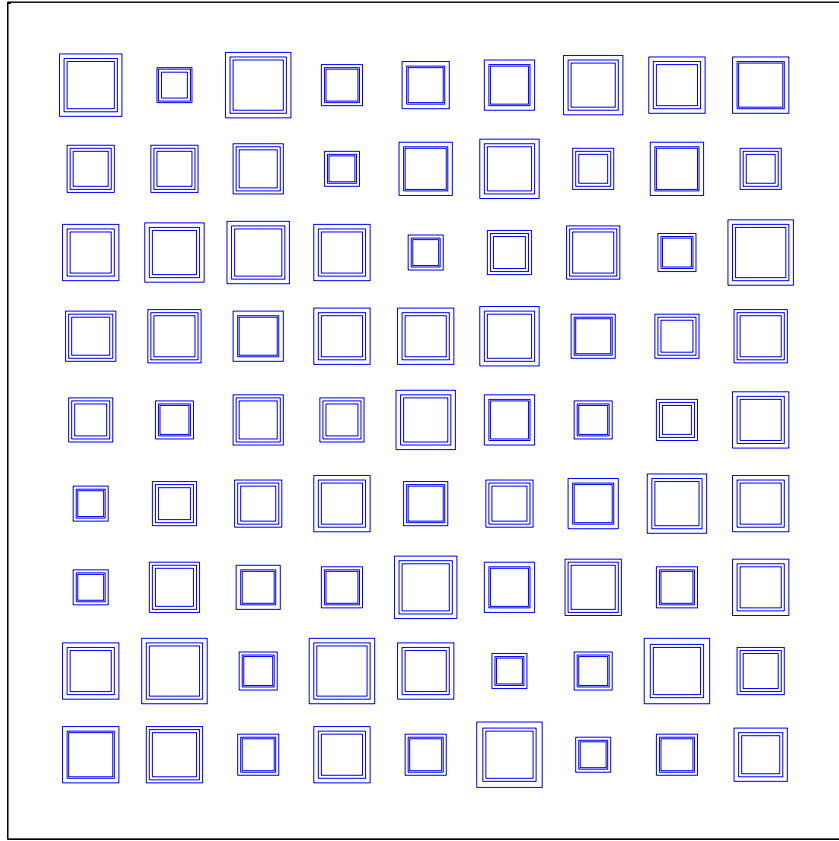


Figure 3-4 Experimental reflectarray with varying sized wideband elements.

$$\bar{J}_1 = \begin{bmatrix} [\bar{J}^{ring}]_{111 \times 1} \\ [0] \\ \vdots \\ [0]_{176 \times 1} \end{bmatrix}_{287 \times 1} \quad (3-1)$$

$$\bar{J}_2 = \begin{bmatrix} [0] \\ \vdots \\ [0]_{111 \times 1} \\ [\bar{J}^{patch}]_{176 \times 1} \end{bmatrix}_{287 \times 1}$$

\bar{J}_1 and \bar{J}_2 are used in (2-49) and error in current is computed by (2-50). The error in current is plotted as function of incidence angle for both incidence types.

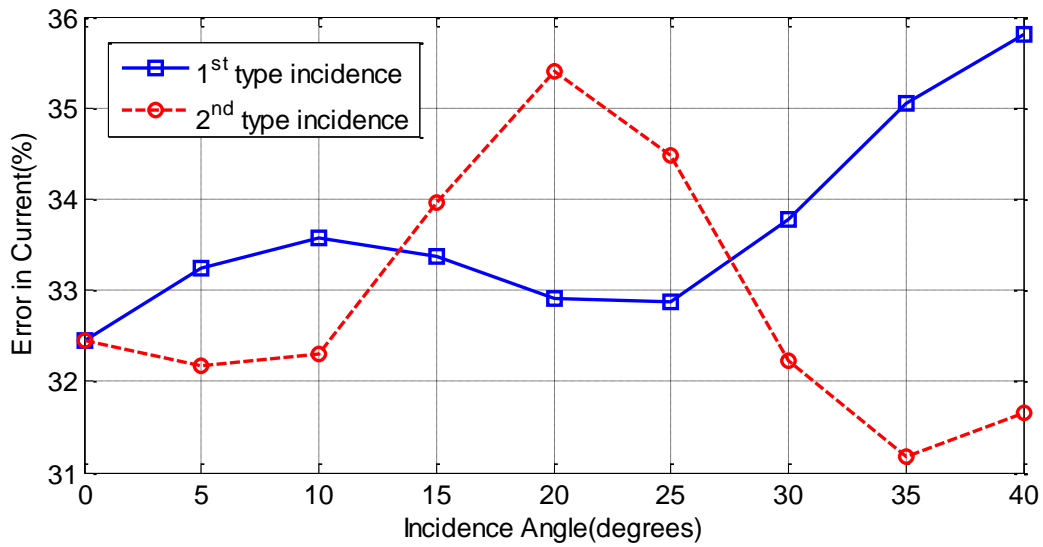


Figure 3-5 Variation of error in current with incidence angle when CMs for the separate metallizations of the wideband patch.

The far field is calculated with approximate current and compared to the far field computed by the conventional MoM current. The comparison of the two far fields for the incidence cases with largest current error can be seen in Figure 3-6 and Figure 3-7. The normalization is done with respect to the maximum of the far field computed by the conventional MoM current.

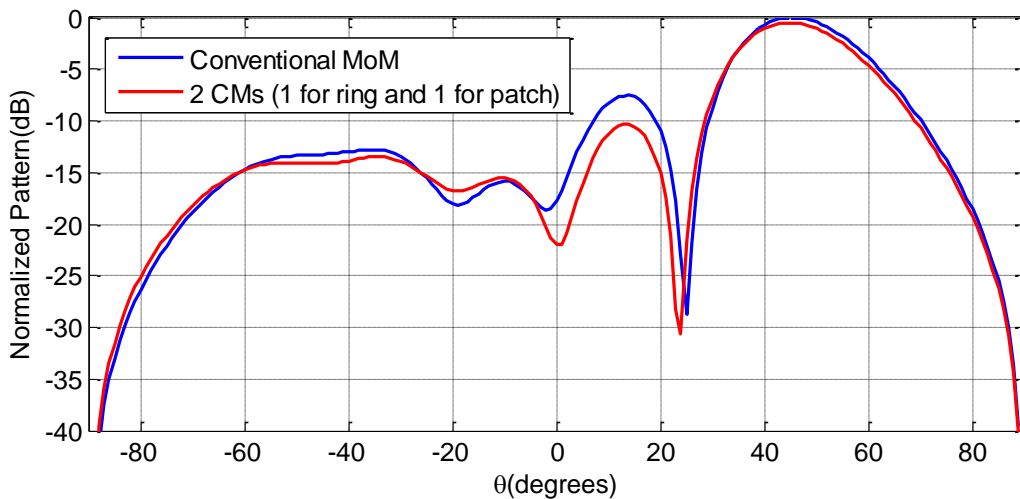


Figure 3-6 Comparison of the amplitude of the φ polarized far fields at $\varphi=0^\circ$, computed by Conventional MoM and using fundamental characteristic modes of separate metallizations (40 degrees, 1st type incidence).

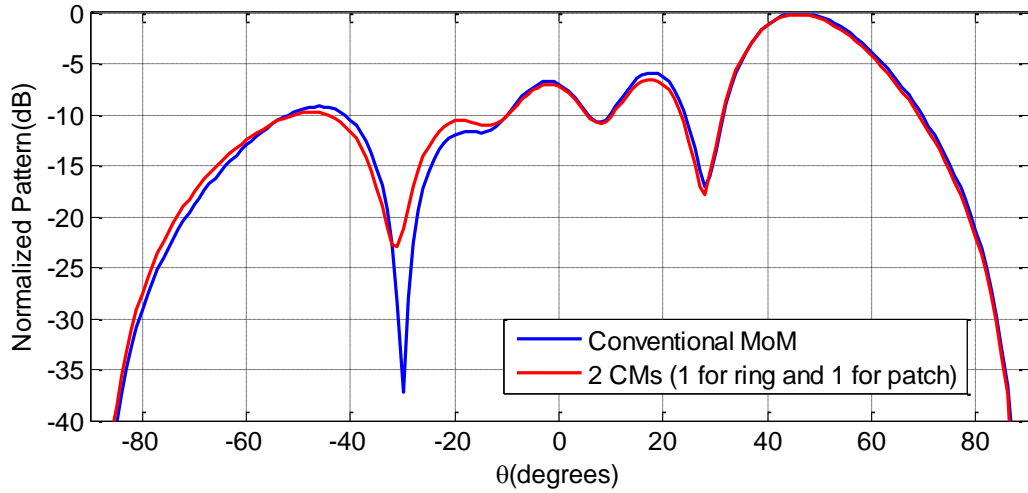


Figure 3-7 Comparison of the amplitude of the θ polarized far fields at $\varphi=90^\circ$, computed by Conventional MoM and using fundamental characteristic modes of separate metallizations (20 degrees, 2nd type incidence).

3.1.2 Separability

The results in the previous section are valuable but not useful alone. In order to be able to omit the calculation of the conventional MoM impedance matrix, tabulation should be feasible and this requires the existence of separability. It is actually observed that separability is possible for this element and it is appreciated by comparing Figure 3-8 with Figure 3-9 and Figure 3-10 with Figure 3-11. When Figure 3-8 is compared with Figure 3-9, it is seen that the reduced matrix entries associated with self and cross products of \bar{J}_1 and \bar{J}_2 are very similar functions of source and observation element sizes for different displacement types. On the other hand, when Figure 3-10 and Figure 3-11 are compared, it is seen that the reduced matrix entries associated with self and cross products of \bar{J}_1 and \bar{J}_2 are very similar functions of horizontal and vertical displacement for different size combinations. The cases that violate separability are similar to that of the resonant square patch of the previous chapter and will not be elaborated here.

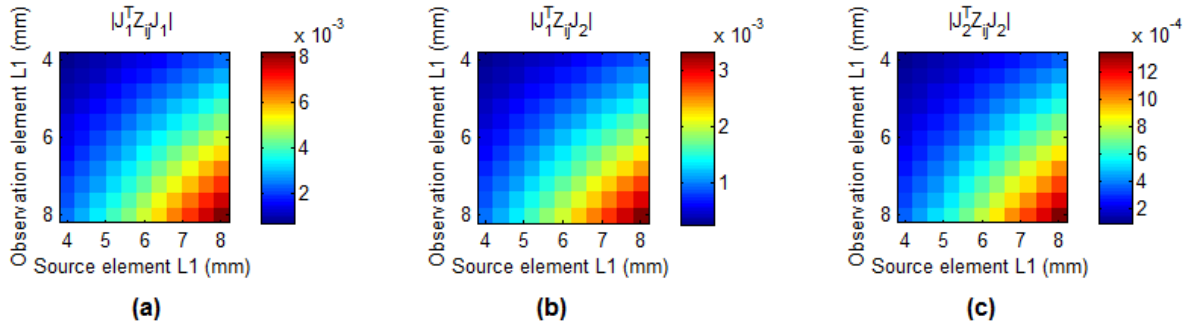


Figure 3-8 Amplitudes of reduced matrix entries for $d_x=40$ mm, $d_y=100$ mm, (a):

$$\bar{J}_1^T \bar{Z}^{ij} \bar{J}_1, \text{ (b): } \bar{J}_1^T \bar{Z}^{ij} \bar{J}_2, \text{ (c): } \bar{J}_2^T \bar{Z}^{ij} \bar{J}_2.$$

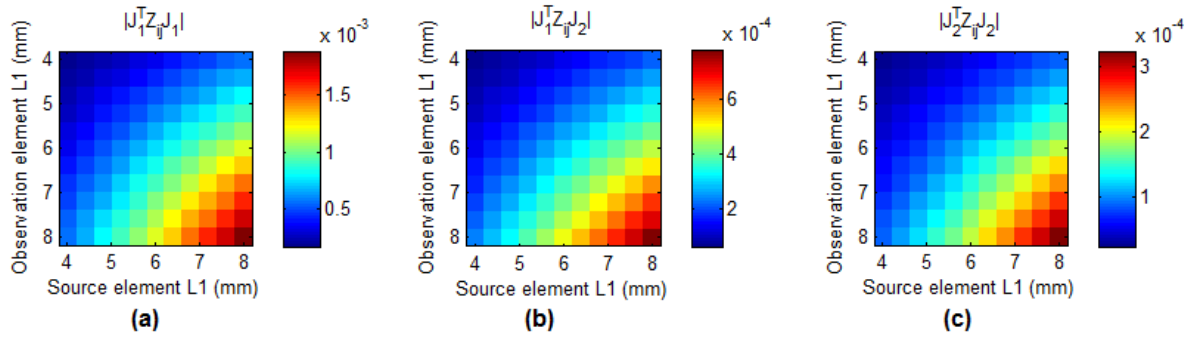


Figure 3-9 Amplitudes of reduced matrix entries for $d_x=80$ mm, $d_y=40$ mm, (a):

$$\bar{J}_1^T \bar{Z}^{ij} \bar{J}_1, \text{ (b): } \bar{J}_1^T \bar{Z}^{ij} \bar{J}_2, \text{ (c): } \bar{J}_2^T \bar{Z}^{ij} \bar{J}_2.$$

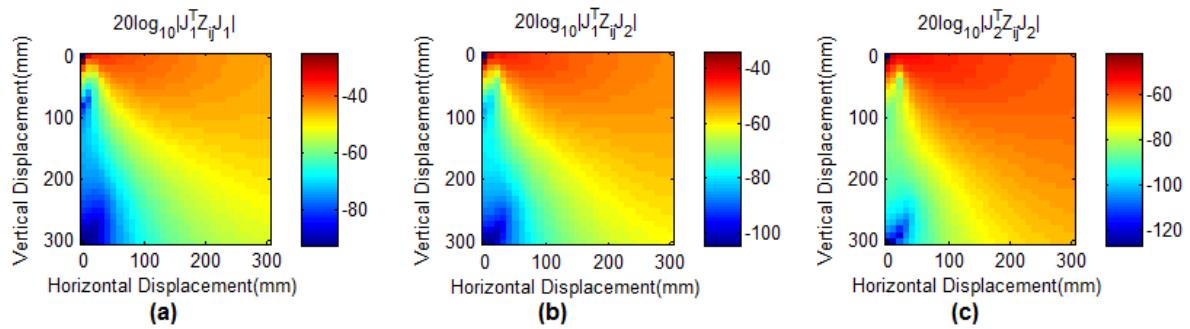


Figure 3-10 Amplitudes of reduced matrix entries for $L_1=8$ mm for source element

$$\text{and } L_1=8 \text{ mm for observation element, (a): } \bar{J}_1^T \bar{Z}^{ij} \bar{J}_1, \text{ (b): } \bar{J}_1^T \bar{Z}^{ij} \bar{J}_2, \text{ (c): } \bar{J}_2^T \bar{Z}^{ij} \bar{J}_2.$$

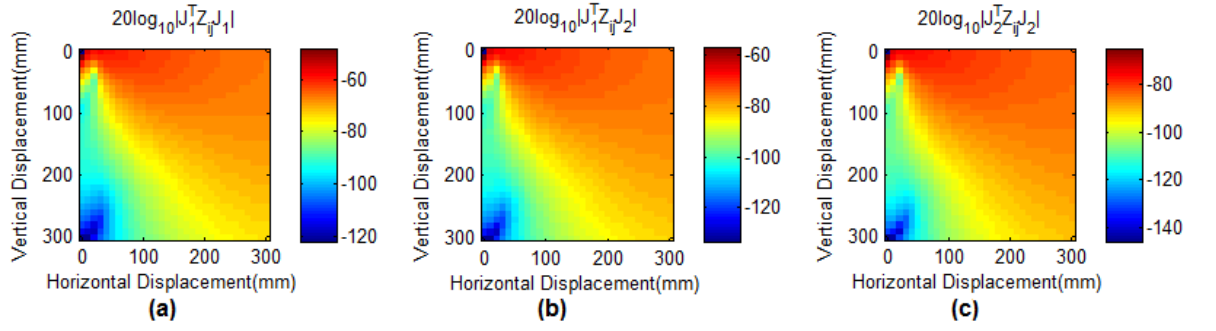


Figure 3-11 Amplitudes of reduced matrix entries for $L_1=4$ mm for source element and $L_1=4$ mm for observation element, (a): $\bar{J}_1^T \bar{Z}^{ij} \bar{J}_1$, (b): $\bar{J}_1^T \bar{Z}^{ij} \bar{J}_2$, (c): $\bar{J}_2^T \bar{Z}^{ij} \bar{J}_2$.

3.2 Reflectarray Element for Rotational Phase Variation Technique

Although the study is originally focused on the reflectarrays with variable-sizes, adaptation of the method for a different type reflectarray is investigated as well. Another common technique besides the size variation is the element rotation technique [10]. This technique is appropriate for circularly polarized reflectarrays and is based on the change of reflection phase with the rotation angle of the element. A popular element suitable for this technique is the split ring resonator shown in Figure 3-12. In the design of this element the parameters are optimized to yield good cross polarization suppression. The unit cell can be regarded as a two port network with the two fundamental Floquet Modes as the two distinct ports.

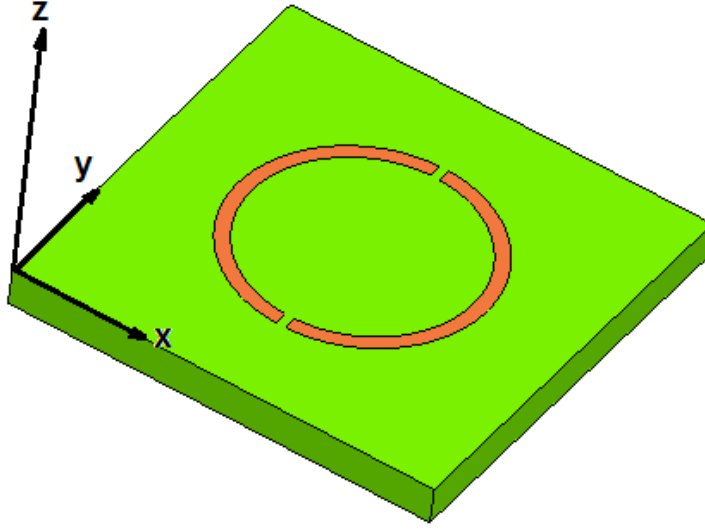


Figure 3-12 Split – ring resonator.

If a^x and a^y represent the x and y polarized components of the incident field, the x and y polarized components of the reflected fields, b^x and b^y can be found as:

$$\begin{bmatrix} b^x \\ b^y \end{bmatrix} = \begin{bmatrix} S_{xx} & S_{xy} \\ S_{yx} & S_{yy} \end{bmatrix} \begin{bmatrix} a^x \\ a^y \end{bmatrix} = \bar{\bar{S}} \bar{\bar{a}} \quad (3-2)$$

where the $\bar{\bar{S}}$ matrix is the scattering matrix associated with the two fundamental Floquet Ports. If the incident field is right hand circularly polarized and incident towards $-z$ direction,

$$\begin{bmatrix} b^x \\ b^y \end{bmatrix} = \begin{bmatrix} S_{xx} & S_{xy} \\ S_{yx} & S_{yy} \end{bmatrix} \begin{bmatrix} \frac{1}{\sqrt{2}} \\ \frac{j}{\sqrt{2}} \end{bmatrix} \quad (3-3)$$

The RHCP and LHCP components of the reflected field can be found by taking the dot product of it with the conjugate of the unit vectors for RHCP and LHCP:

$$\begin{bmatrix} b^{RHCP} \\ b^{LHCP} \end{bmatrix} = \begin{bmatrix} \frac{1}{\sqrt{2}} & \frac{j}{\sqrt{2}} \\ \frac{1}{\sqrt{2}} & \frac{-j}{\sqrt{2}} \end{bmatrix} \begin{bmatrix} b^x \\ b^y \end{bmatrix} = \begin{bmatrix} \frac{S_{xx} + jS_{xy} - jS_{yx} + S_{yy}}{2} \\ \frac{S_{xx} + jS_{xy} + jS_{yx} - S_{yy}}{2} \end{bmatrix} \quad (3-4)$$

In order to apply the method, a split ring resonator element is first designed with the following design properties:

- Frequency: 10 GHz
- Substrate thickness: 1.59 mm
- Substrate relative permittivity: 4.2
- Element spacing: 18 mm in both dimensions ($d_x=d_y=18$ mm.)
- Lattice type: Cartesian.

A good design in terms of cross polarization suppression is obtained by parametric sweep in HFSS. The parameters of this design is as follows: $r_1=4.7$ mm, $r_2=5.3$ mm, $w=0.2$ mm.

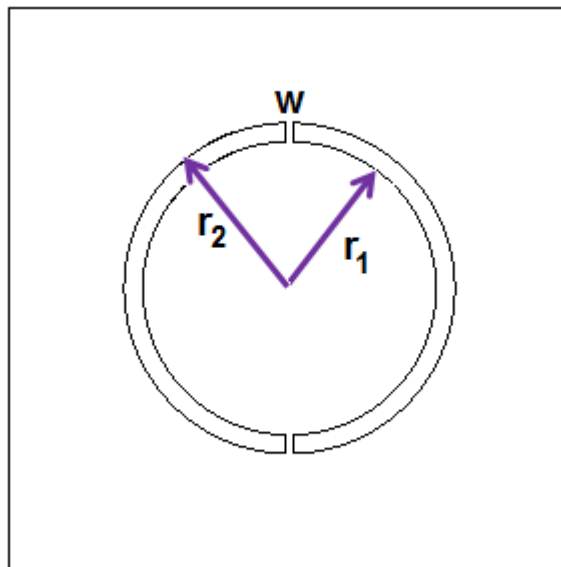


Figure 3-13 Parameters of the split – ring resonator.

When this element is rotated around z axis from 0 to 180 degrees, the reflection phase changes linearly with rotation angle and equals almost twice of it as seen in Figure 3-14.

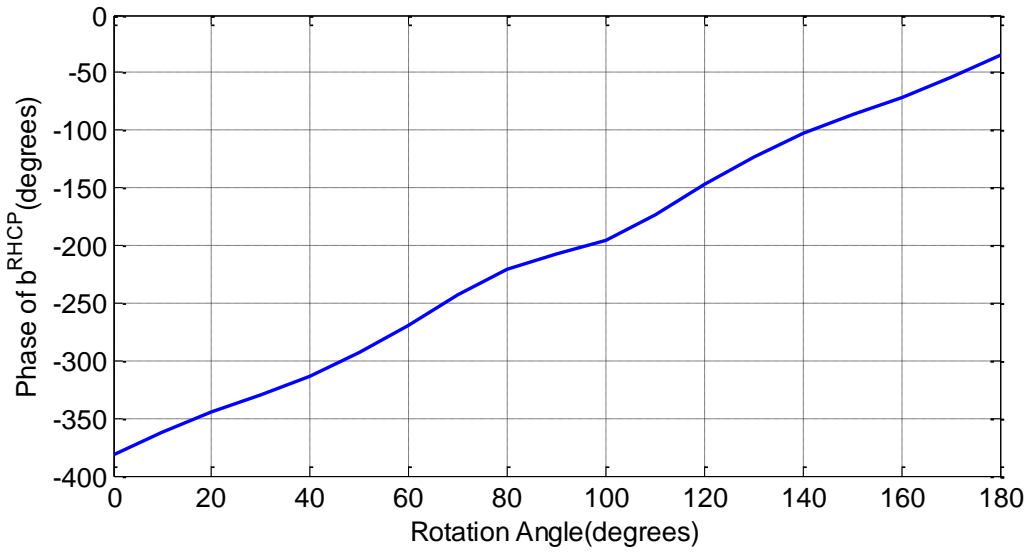


Figure 3-14 Phase of the right hand circular polarized component of the reflected field for the split ring resonator.

The variation of the magnitudes of the RHCP and LHCP components with rotation angle can be observed in Figure 3-15.

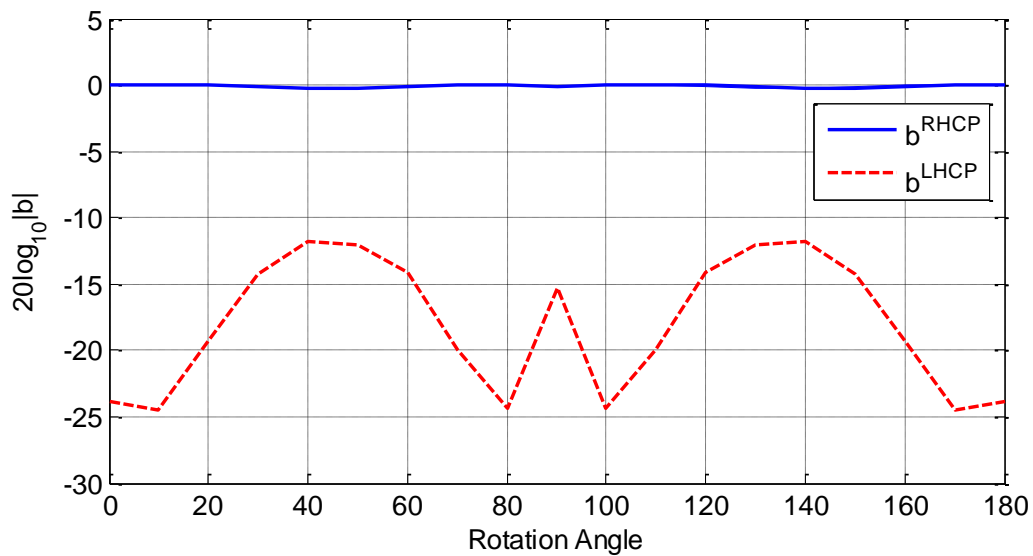


Figure 3-15 Magnitude of the right hand and left hand circularly polarized components of the reflected field for the split ring resonator.

3.2.1 Reusability of CMs

As the shape of the element is invariant, when same mesh is used and is a rotated replica of a reference mesh, the CMs are already the same for all elements because the impedance matrix does not change at all. Therefore the “reusability” in this context is trivial. However, it is worth showing that a few CMs are sufficient in terms of far field estimation. To examine this idea, an 8x8 reflectarray with randomly rotated split ring resonators is analyzed. The reflectarray is illuminated with plane waves of various incidence angles for the two different incidence types defined before. The current density on the metallization is found by conventional method of moments first, and an approximate current is calculated by using the dominant characteristic mode as in (2-41). The error in current is recorded and shown in Figure 3-16. The behavior of error in current is similar for the two incidence types because of the circular element geometry and circular polarization.

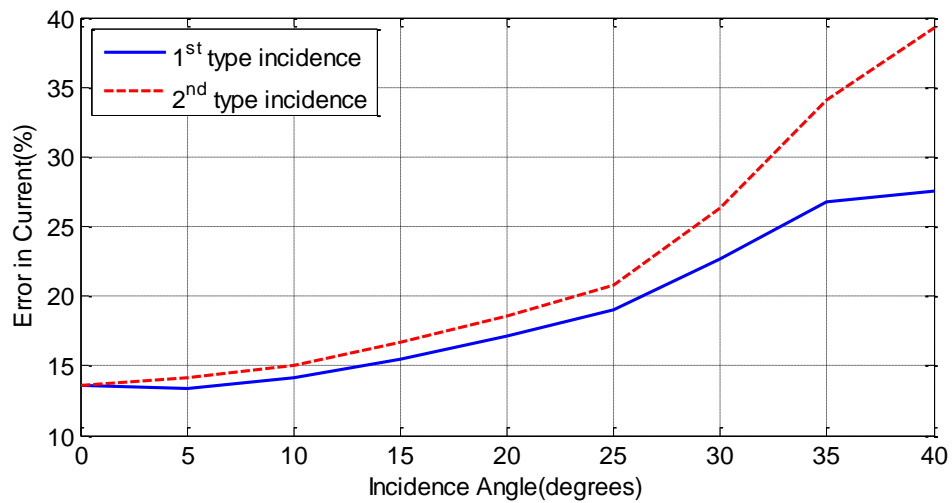


Figure 3-16 Variation of error in current with incidence angle (single mode).

When the far field patterns calculated by the conventional MoM current and approximate current are compared, it is seen that the result is not as satisfactory as the result obtained for the square patch, especially for large incidence angles. Thus it is decided to take more modes. When the 4 most significant modes are taken, the error in current is as low as seen in Figure 3-17 and the agreement with the far field

obtained by the conventional MoM current is almost perfect as seen in Figure 3-18 and Figure 3-19, for the case with the largest current error seen in Figure 3-17.

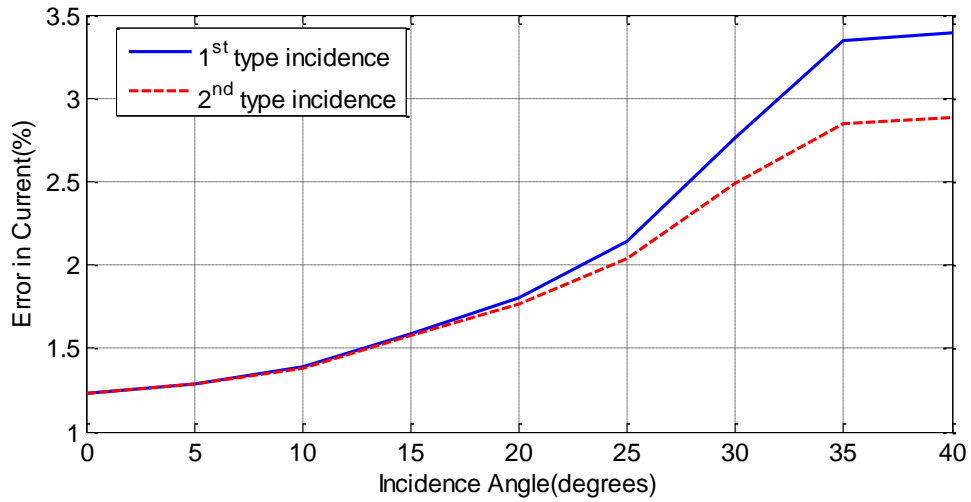


Figure 3-17 Variation of error in current with incidence angle (4 modes).

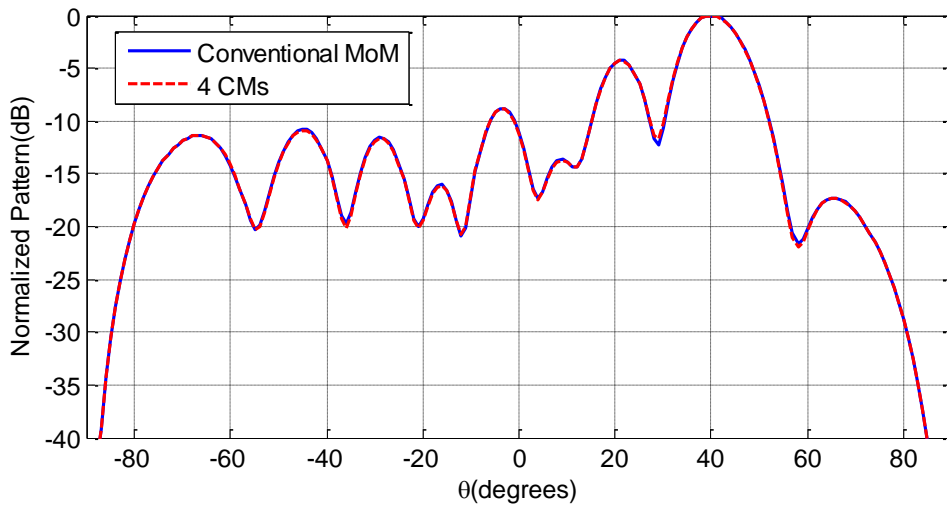


Figure 3-18 Amplitude of \hat{x} polarized E field on the H plane.

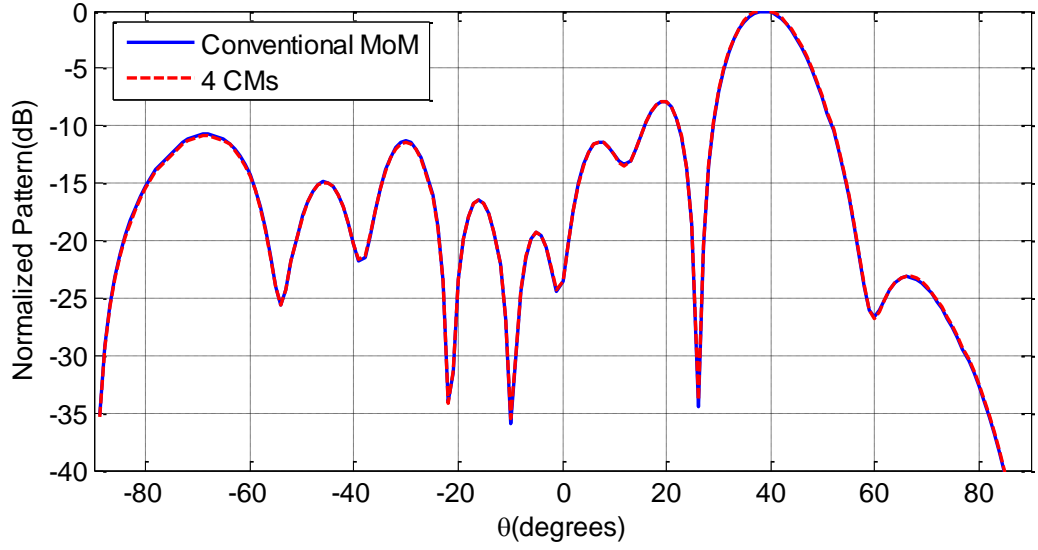


Figure 3-19 Amplitude of \hat{y} polarized E field on the H plane.

3.2.2 Separability

It was shown that a few modes are sufficient to estimate the far field but in order to avoid matrix filling and making the tabulation feasible, it is necessary to have the separability. In this case the variables that alter the reduced matrix term are the distance of the split rings, R , the relative polar angle, θ , and the rotation angle, γ , of the observation split ring. These variables are explained in Figure 3-20. There are certainly too many combinations of these three variables for a large reflectarray. Thus it would be convenient to have:

$$f^{p,q}(R, \theta, \gamma) \cong g^{p,q}(R)h^{p,q}(\theta)k^{p,q}(\gamma) \quad (3-5)$$

or at least

$$f^{p,q}(R, \theta, \gamma) \cong g^{p,q}(R)h^{p,q}(\theta, \gamma) \quad (3-6)$$

or other separable forms with a function of one of the variable and a function of the two remaining variables. In (3-5) and (3-6) $f^{i,j}(R, \theta, \gamma)$ stand for the reduced matrix term that is associated with the characteristic modes J_p and J_q . As there are 4 modes to be considered, there exist 10 different types of matrix entries. Note that 6 of the possible 16 combinations correspond to cross-coupling between modes and have reciprocal pairs.

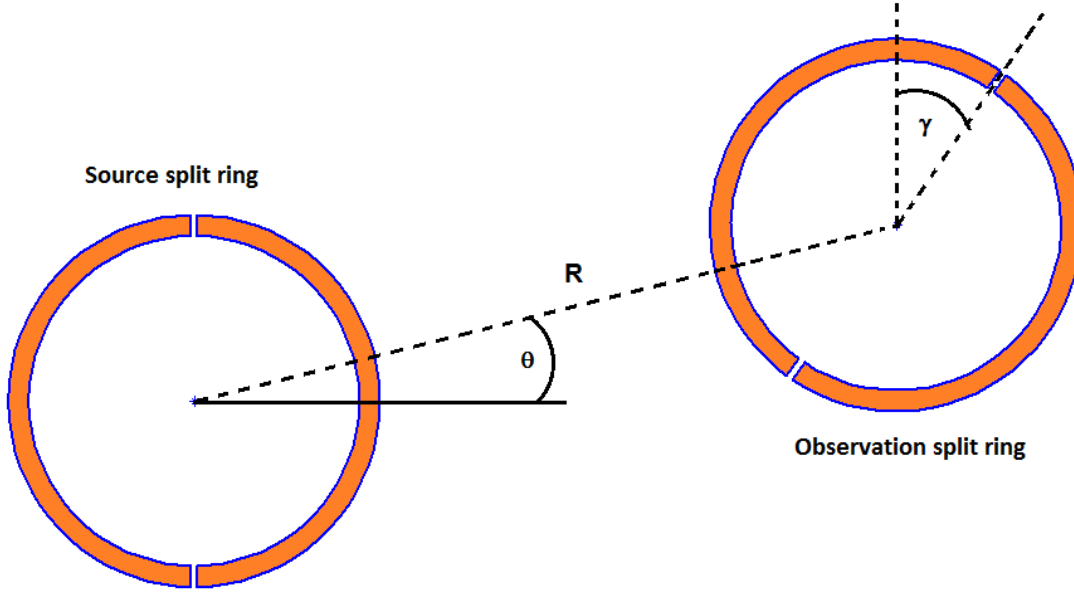


Figure 3-20 Parameters that influence the reduced matrix entries.

Unfortunately, observations showed that the separability forms in either (3-5) or (3-6) does not exist. Nevertheless, an alternative approximating approach is proposed. In this approach, the three dimensional function $f^{p,q}(R, \theta, \gamma)$ is sampled at three planes, as shown in Figure 3-21, instead of three lines (as proposed in (3-5)), or a plane plus a line (as proposed in (3-6)). For a general point P_1 , where the data is missing, three different approximations can be done:

$$f^{p,q^1}(R_1, \theta_1, \gamma_1) \cong \frac{f^{p,q}(R_0, \theta_1, \gamma_1)}{f^{p,q}(R_0, 0, \gamma_1)} f^{p,q}(R_1, 0, \gamma_1) \quad (3-7)$$

$$f^{p,q^2}(R_1, \theta_1, \gamma_1) \cong \frac{f^{p,q}(R_0, \theta_1, \gamma_1)}{f^{p,q}(R_0, \theta_1, 0)} f^{p,q}(R_1, \theta_1, 0) \quad (3-8)$$

$$f^{p,q^3}(R_1, \theta_1, \gamma_1) \cong \frac{f^{p,q}(R_1, 0, \gamma_1)}{f^{p,q}(R_1, 0, 0)} f^{p,q}(R_1, \theta_1, 0) \quad (3-9)$$

These approximations correspond to reaching the unknown point P_1 via the known points A,B and E; A, C and D; B, C and F respectively. The coordinates of the points in Figure 3-21 are listed in

Table 3-1. The approximations given in (3-7), (3-8) and (3-9) are equivalent to assuming:

$$1^{st} \text{ approximation} \rightarrow \frac{f^{p,q}(R_0, \theta_1, \gamma_1)}{f^{p,q}(R_0, 0, \gamma_1)} = \frac{f^{p,q}(R_1, \theta_1, \gamma_1)}{f^{p,q}(R_1, 0, \gamma_1)} \quad (3-10)$$

$$2^{nd} \text{ approximation} \rightarrow \frac{f^{p,q}(R_0, \theta_1, \gamma_1)}{f^{p,q}(R_0, \theta_1, 0)} = \frac{f^{p,q}(R_1, \theta_1, \gamma_1)}{f^{p,q}(R_1, \theta_1, 0)} \quad (3-11)$$

$$3^{rd} \text{ approximation} \rightarrow \frac{f^{p,q}(R_1, \theta_1, 0)}{f^{p,q}(R_1, 0, 0)} = \frac{f^{p,q}(R_1, \theta_1, \gamma_1)}{f^{p,q}(R_1, 0, \gamma_1)} \quad (3-12)$$

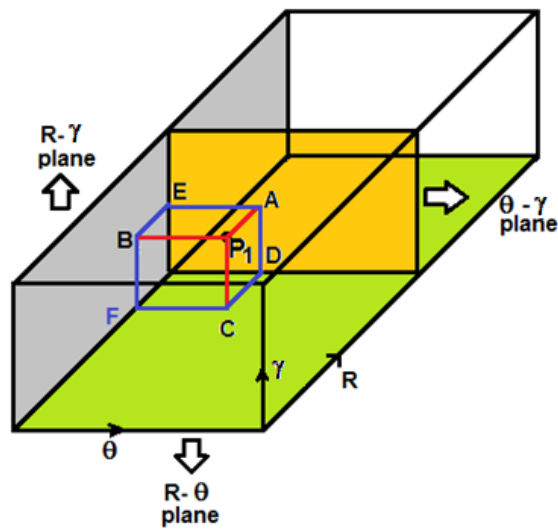


Figure 3-21 Representative picture showing the available tabulations and useful points in approximating the reduced matrix term for an arbitrary $(R_1, \theta_1, \gamma_1)$.

Table 3-1 The coordinates of the points of interest in Figure 3-21.

Point	Coordinates
A	$(R_0, \theta_1, \gamma_1)$
B	$(R_1, 0, \gamma_1)$
C	$(R_1, \theta_1, 0)$
D	$(R_0, \theta_1, 0)$
E	$(R_0, 0, \gamma_1)$
F	$(R_1, 0, 0)$

In order to check the accuracy offered by the approximations, the functions $f^{p,q}(R, \theta, \gamma)$ are sampled at $R=18$ mm, $\theta=0$ degrees, and $\gamma=0$ degrees planes. Next; using (3-7), (3-8), and (3-9) the functions are approximated at $R=10.8$ mm for all θ and γ . Afterwards, the functions are calculated rigorously by the exact $\bar{\bar{Z}}^{ij}$ values at $R=10.8$ mm. It was seen that the second approximation given in (3-8) is the most successful one in terms of accuracy. This should be expected because this approximation assumes that the rotation of the observation split ring, γ , has an effect on the function value irrespective of the distance, which is a more reasonable assumption as compared to those made in the other approximations. Note that if it was also assumed that the effect of rotation is independent of the polar angle θ , it would correspond to the usual separability condition. Two examples, namely $f^{1,1}(R, \theta, \gamma)$ and $f^{3,4}(R, \theta, \gamma)$, of the 10 different approximate $f^{p,q}(R, \theta, \gamma)$, are compared with their exact counterparts in Figure 3-22 and Figure 3-23. Remaining 8 functions and phase characteristics are not presented here for space considerations, but those approximations are observed to be in good agreement with their respective exact forms as well.

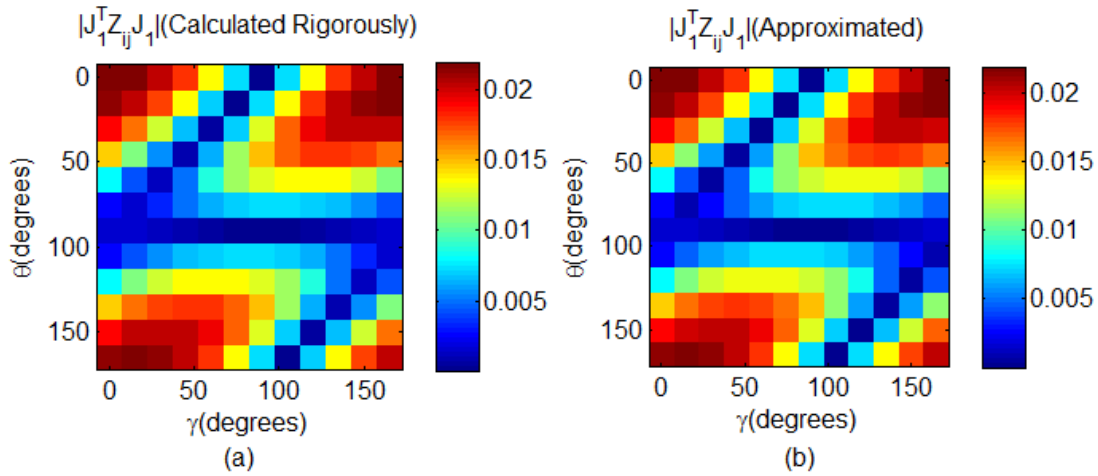


Figure 3-22 Amplitude of $J_1^T \bar{\bar{Z}}^{ij} J_1$ for $R=10.8$ mm, (a): Calculated by the actual impedance matrix $\bar{\bar{Z}}^{ij}$, (b): Approximated by (3-8).

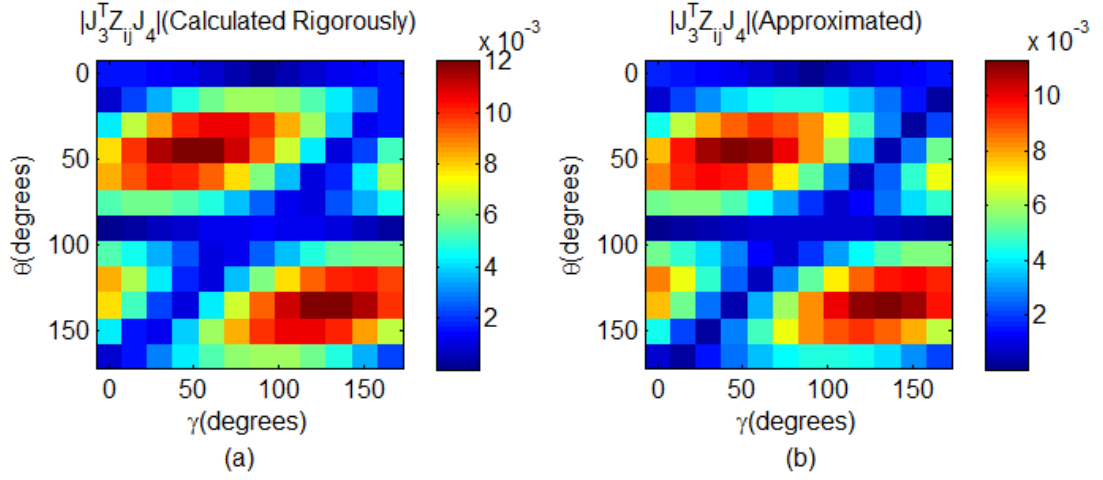


Figure 3-23 Amplitude of $\bar{J}_3^T \bar{Z}^{ij} \bar{J}_4$ for $R=10.8$ mm, (a): Calculated by the actual impedance matrix \bar{Z}^{ij} , (b): Approximated by (3-8).

3.3 Conclusions

In this chapter, it was shown that the fast solution method is also feasible for different patch types, with minor modifications. For the wideband patch which is composed of a square patch and an outer ring, it is required to use the individual characteristic modes of the resonant square patch and the resonant outer ring to have a fair accuracy in the far field. This method also satisfies the separability of the function that yields the reduced matrix entries, which is critical for the acceleration of the computation of the reduced matrix. As a second example, the split ring resonator is studied as a circularly polarized reflectarray element. Although the reusability is already available due to rotation technique, it is mandatory to modify the concept of separability to obtain a reasonable approximation for the reduced matrix entries. The approximation assumes that the effect of the rotation of the observation split ring on the reduced matrix entries is independent of its distance to the source split ring, but not independent of the polar angle with respect to the source split ring.

CHAPTER 4

UTILIZATION OF THE EFFICIENT ANALYSIS METHOD IN DESIGN PROBLEMS

In the previous chapters it was shown that the developed analysis method is accurate and the solution time it offers is promising, if it is to be used in the optimization of a reflectarray. In this chapter, this idea is tested and proven by practical examples. The reflectarray optimization problem is defined as finding the reflectarray configuration that yields the closest pattern to a desired pattern given the following:

- frequency,
- spacing between elements,
- substrate properties (height and permittivity),
- feed antenna and its position/orientation with respect to the array,
- horizontal and vertical dimensions of the array.

The variables to be optimized are the sizes of each element on the reflectarray since given the variables listed above; the far field is a function of the element sizes only. To initiate the optimization procedure, in addition to the tabulations mentioned in Chapter 2, the following quantities should be computed beforehand:

- The incident electric field value by (2-2) at the element centers,
- The far field scattered by the dielectric coated ground plane in the absence of patches,
- The far fields of the patch candidates that carry the modal current \bar{J}_1 (and \bar{J}_2 if two modes are to be used)

The computations listed above are carried out only once and they are constant during the optimization process. In order to be able to compute these quantities, the feed is modeled and simulated in HFSS. The electric and magnetic fields are sampled on the 6 faces of the radiation boundary (Figure 4-1) and exported as text files. The electric and magnetic fields on each surface are used to define the equivalent currents:

$$\begin{aligned}\bar{M}_s &= -\hat{n} \times \bar{E} \\ \bar{J}_s &= \hat{n} \times \bar{H}\end{aligned}\tag{4-1}$$

where \hat{n} represents the respective unit outward normal of each surface. Then, free space Green's function for magnetic and electric currents are used to obtain the field anywhere outside the radiation boundary. To validate the computations, the \hat{y} polarized electric field at a horizontal line of 540 mm long at distance of 360 mm from the feed antenna aperture is computed by equivalent currents and compared to HFSS result. Figure 4-2 and Figure 4-3 demonstrate the amplitude and phase of the \bar{E} field given by HFSS and computed by using field equivalence.

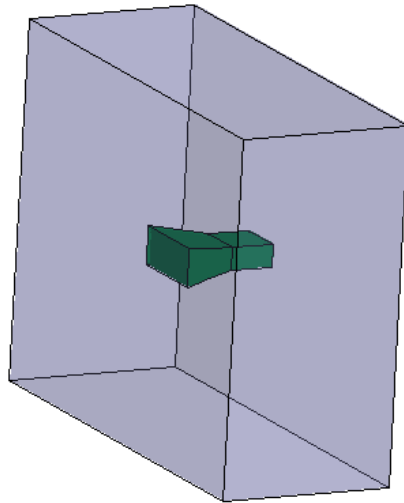


Figure 4-1 Radiation boundary around the feed antenna.

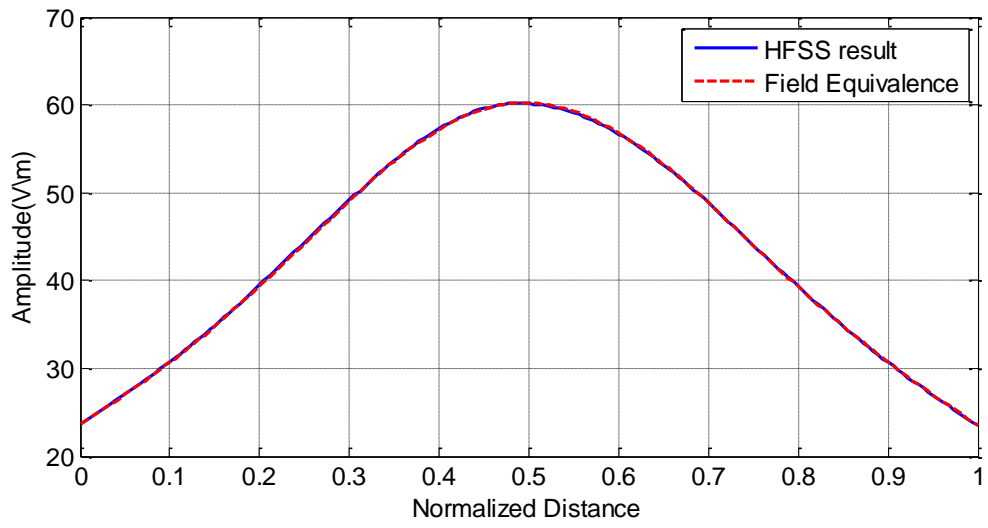


Figure 4-2 Amplitude of \hat{y} polarized E field on a 540 mm long line, 360 mm away from the feed antenna.

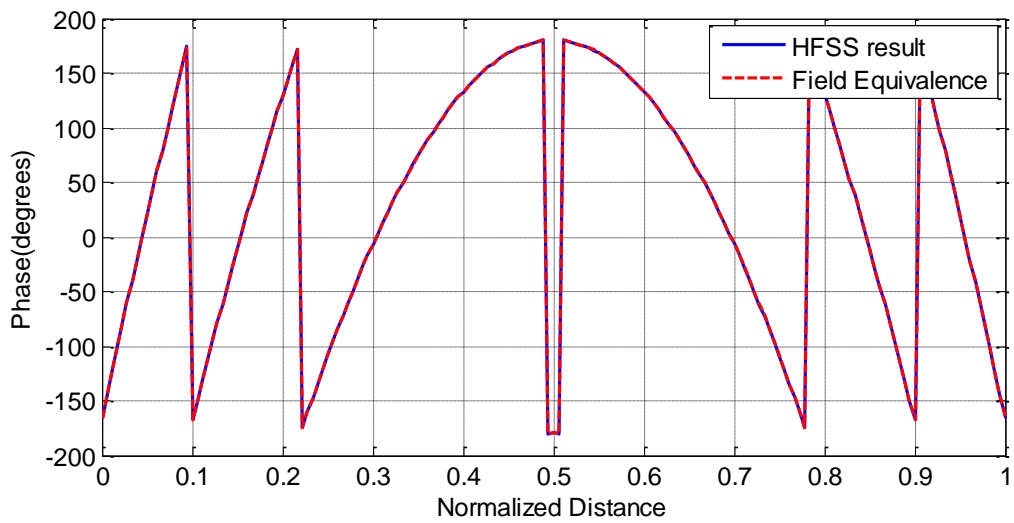


Figure 4-3 Phase of \hat{y} polarized E field on a 540 mm long line, 360 mm away from the feed antenna.

4.1 Preliminary Computations

4.1.1 Incident Field at Element Centers

As mentioned in Chapter 2, it is possible to approximate the value of \bar{V} by assuming that the incident field is constant over the patch. Therefore it is sufficient to find the incident field at the element centers because in a periodic array, the element is always centered on the same point regardless of its dimension. With this assumption, (2-20) proposes that the value of vector \bar{V} is proportional to the square of the element size, due to linear dependence of l_m , $\bar{\rho}_m^{c+}$ and $\bar{\rho}_m^{c-}$ on size. Hence the value of \tilde{V} belonging to a particular element is proportional to the square of its size. If \tilde{V}_i^{ref} stands for the value of \tilde{V}_i computed for a reference size, s_i^{ref} , then \tilde{V}_i' for s_i' can be approximated as:

$$\tilde{V}_i' = \left(\frac{s_i'}{s_i^{ref}} \right)^2 \tilde{V}_i^{ref} \quad (4-2)$$

Equation (4-2) can be exploited for fast computation of \tilde{V} during optimization.

As the incident field to be used in MoM is the sum of the free space field of the feed antenna and the field reflected by the dielectric coated ground plane, the reflected field should be calculated. For this purpose, the free space field, \bar{E}_0^{inc} should be decomposed into its parallel and perpendicular polarized components. This requires that \bar{E}_0^{inc} be a locally plane wave. The Rayleigh distance for the feed antenna used in this study is computed as 120 mm at 10 GHz. The F/D ratio of the reflectarray antennas in this study is between 0.5 and 0.67. While satisfying this F/D range, the Rayleigh distance is maintained by a safety factor of 1.5 to 4 to guarantee the locally plane wave assumption.

When the incident electric field, \bar{E}_0^{inc} , is decomposed into parallel and perpendicular polarized components, it becomes possible to find the reflected field, \bar{E}^{ref} , by:

$$\bar{E}^{ref} = R^{\perp,\perp} \{\bar{E}_0^{inc}\}^{\perp} + R^{//,//} \{\bar{E}_0^{inc}\}^{//} \quad (4-3)$$

where $R^{\perp,\perp}$ and $R^{//,//}$ stand for the reflection coefficients for perpendicular and parallel polarizations respectively.

4.1.2 The Far Field Due To Ground Scattering

The far field of the reflectarray is modeled as being composed of two components: The field radiated by the patches and the field reflected by the ground backed dielectric. In the optimization, the field radiated by the patches can be altered but the field reflected by the ground backed dielectric is fixed provided that the antenna size and feed antenna geometry is not changed. Therefore it is convenient to calculate and store the far field due to ground scattering beforehand. The far field can be approximately calculated by field equivalence, again considering both magnetic and electric equivalent currents radiating in free space (Figure 4-4). This time the equivalent current densities are given by (4-4). \bar{M}_s and \bar{J}_s generate the total field in the upper part of the reflectarray.



Figure 4-4 Equivalent electric and magnetic currents.

$$\begin{aligned} \bar{M}_s &= -\hat{n} \times (\bar{E}_0^{inc} + \bar{E}^{ref}) \\ \bar{J}_s &= \hat{n} \times (\bar{H}_0^{inc} + \bar{H}^{ref}) \end{aligned} \quad (4-4)$$

To validate the accuracy of the approach, the 16x10 element reflectarray problem in Chapter 2 is considered. The far field field reflected by the ground backed dielectric is calculated by using equivalent currents of (4-4) and compared to Finite Element Method solution provided by HFSS. The field is computed at a finite but large distance in order to be able to compare the phase as well, because phase is also

critical in the superposition of the patch fields and the far field of the ground backed dielectric. Figure 4-5 and Figure 4-6 depicts the amplitude and phase comparisons respectively in $\varphi = 0^\circ$ plane. The discrepancy in the off-boresight angles is due to approximations in calculating \bar{E}^{ref} and \bar{H}^{ref} . It should be noted that the far field due to ground scattering is not a faithful replica of the feed pattern, because the ground plane intercepts incident feed field partially.

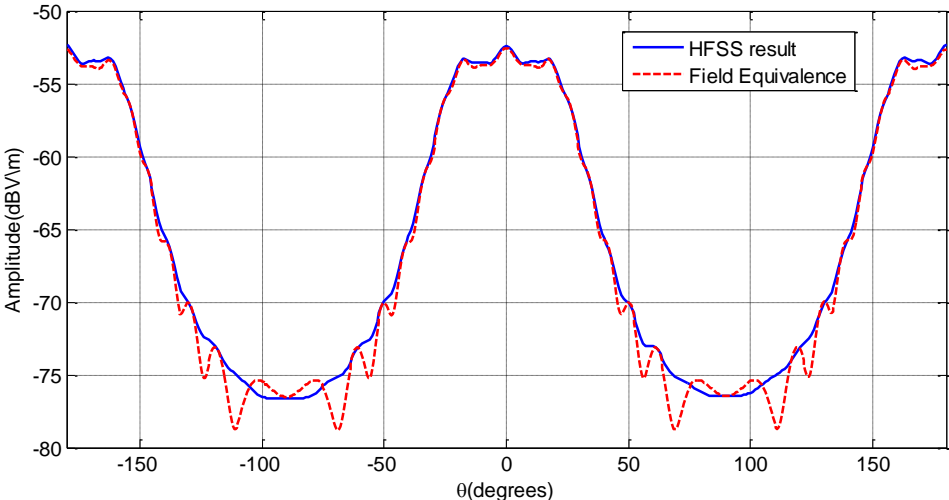


Figure 4-5 Log amplitude of the φ polarized electric field at $R=10^4$ m, at $\varphi = 0^\circ$.

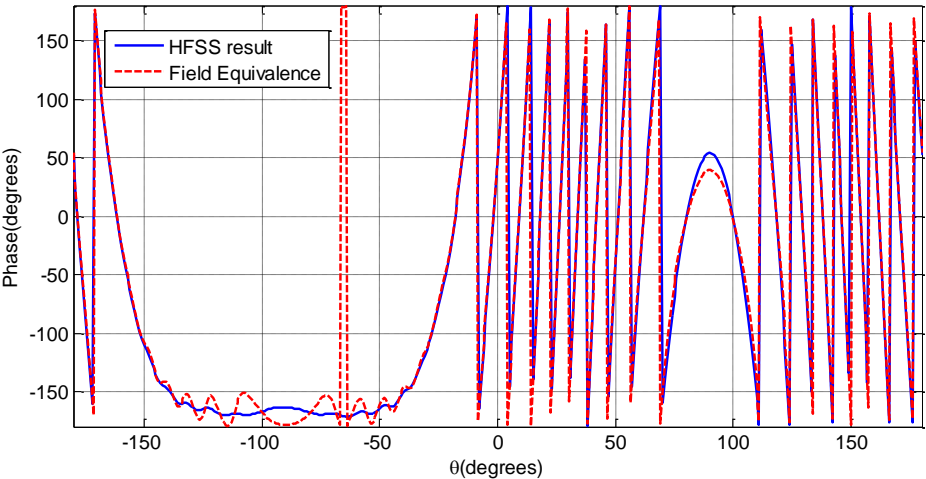


Figure 4-6 Phase of the φ polarized electric field at $R=10^4$ m, at $\varphi = 0^\circ$.

4.1.3 The Far Field Patterns of Candidate Elements

The solution of the reduced equation results in a weighted version of the dominant characteristic mode (or modes) on each patch. Hence, it is not obligatory to find the far field of the patches at each reflectarray configuration considered in optimization. For a given patch size, the far field pattern is directly scaled by the mode coefficient. On the other hand, the effect of the positions of the elements can be incorporated in the pattern by using the translation property of the far field integral. When the element is shifted in space by \bar{r}_s , the new pattern in the original coordinate system can be found by:

$$\begin{aligned}\bar{E}^{new}(\bar{r}) &= \frac{1}{R} \int_S \bar{J}(\bar{r}' + \bar{r}_s) e^{-jk(R - \hat{a}_r \cdot (\bar{r}' + \bar{r}_s))} ds \\ &= e^{jk\hat{a}_r \cdot \bar{r}_s} \frac{1}{R} \int_S \bar{J}(\bar{r}') e^{-jk(R - \hat{a}_r \cdot \bar{r}')} ds \\ &= e^{jk\hat{a}_r \cdot \bar{r}_s} \bar{E}^{original}(\bar{r})\end{aligned}\tag{4-5}$$

since,

$$\bar{J}(\bar{r}') = \bar{J}(\bar{r}' + \bar{r}_s)\tag{4-6}$$

However, the patch size affects the *shape* of the far field radiation pattern as seen in Figure 4-7. Thus, the far field should be characterized for patch size only. As the patch is an electrically small structure, the far field can be tabulated with relatively large angular steps (2 degrees for instance). However, it should be interpolated later for use in the entire array, with smaller step size depending on the array size because the larger the array, the more rapidly the pattern is likely to change with angle.

In summary, after the characteristic mode coefficients for all patches are found using Eq. (2-43),

- 1) The far field pattern of each patch is scaled with their respective modal coefficients,
- 2) The far field pattern of each patch is referred to the common coordinate system,

- 3) The far field patterns of all patches are superposed,
- 4) The far field of the reflectarray is found by adding the far field pattern due to ground backed dielectric layer and the far field pattern of all patches found in 3rd step.

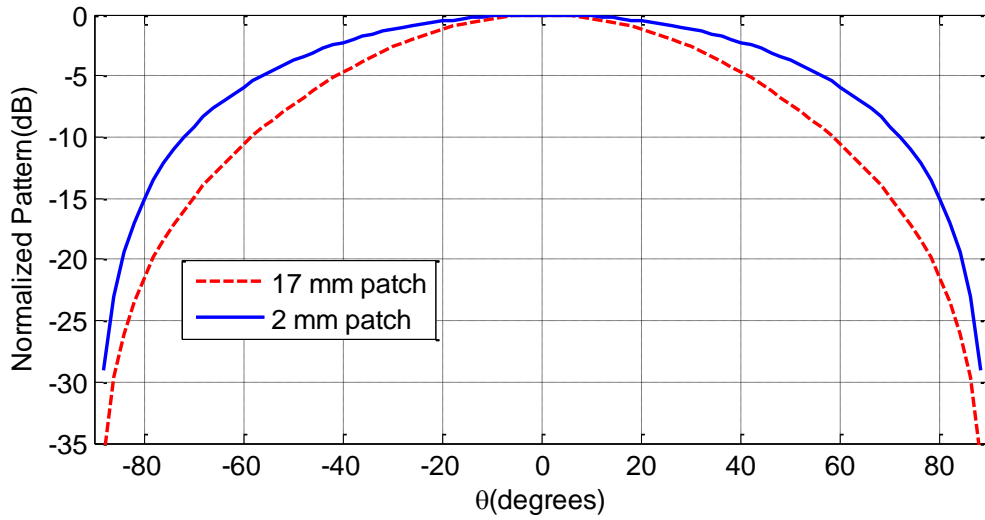


Figure 4-7 Comparisons of the normalized far field patterns of 17 mm patch and 2 mm patch, each carrying the dominant mode current, J_1 . Observation plane: $\varphi = 0^\circ$, polarization: $\hat{\varphi}$.

4.1.3.1 2D Pattern Definition

The 2 dimensional far field patterns in the forthcoming parts are defined on the azimuth-over-elevation grid system shown in Figure 4-8. This is actually equivalent to a theta-phi grid in conventional spherical coordinates but the antenna lies in the y-z plane and its boresight is along the x direction. This grid is preferred due to its convenience in 2D pattern visualization. The main polarization for \hat{z} polarized current is defined to be along $\hat{\theta}$.

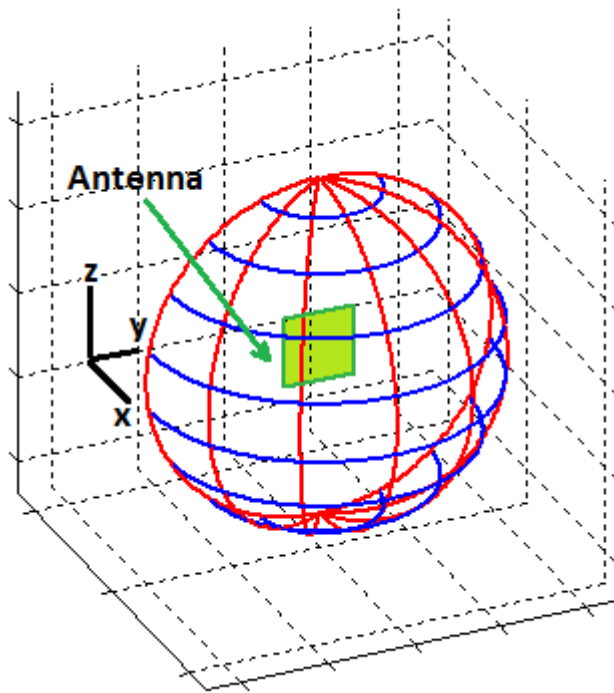


Figure 4-8 Azimuth-over-elevation grid.

4.2 Reflectarray Design as an Optimization Problem

The reflectarray design process can be regarded as an optimization problem, irrespective of the design method applied. In any case, the designer seeks for an array configuration that results in the desired properties of the far field pattern. When the infinite array approach is applied, the reflection phase of each element is optimized to yield the required phase distribution across the array, which eventually should generate the desired far field pattern. This technique is criticized in [46] due to involving a preliminary step for synthesizing the aperture phase and thus carrying an indirect link between element geometry and the far field. Instead, a method is proposed so that the element sizes can be directly optimized by observing the far field pattern.

In this dissertation, although the design philosophy is similar to that of [46], it diverts from [46] by the analysis method applied. In [46], the local periodicity approach is employed in predicting the response of an element. In this study on the other hand, the analysis method in each step of optimization is the one explained in Chapter 2.

Single characteristic mode is used, but it is straightforward to extend to two characteristic modes. In either case number of design parameters is equal to the number of array elements, though the number of unknowns is doubled.

It is the right place to mention that the nature inspired algorithms, i.e. Genetic Algorithm, Particle Swarm Optimization, Ant Colony Optimization etc., are not preferred even though it becomes possible to use them with the proposed solution approach. These methods require a great number of candidate solutions and a great number of iterations to find a reasonable solution. On the other hand, directional search algorithms focus on a single candidate solution and are generally more robust. Their drawback is that they require a good starting point. Yet, in reflectarray design, the starting point can be provided by the conventional infinite array approach. For reflectarrays of variable element sizes, the optimum design can be defined to be the one that minimizes the cost function C given in (4-7).

$$C(\bar{x}) = \|\bar{P}_s(\bar{x}, \theta, \varphi) - \bar{P}_d(\bar{x}, \theta, \varphi)\|^2 \quad (4-7)$$

where $\bar{P}_s(\bar{x}, \theta, \varphi)$ represents the synthesized pattern magnitude and $\bar{P}_d(\bar{x}, \theta, \varphi)$ represents the desired pattern magnitude, observed at angles θ and φ defined in 4.1.3.1. The sizes of the elements is a vector symbolized as \bar{x} . Although many different forms of cost function are possible, the form in (4-7) is usually chosen in pattern synthesis problems. In practice, $\bar{P}_s(\bar{x}, \theta, \varphi)$ and $\bar{P}_d(\bar{x}, \theta, \varphi)$ are sampled at discrete points in order to carry out the synthesis procedure with numerical methods. The sampling intervals in θ and φ should be chosen so as to satisfy the Nyquist criterion. Otherwise, the synthesized pattern may exhibit unexpected behavior between the consecutive sampling points. If a total of N far field points are considered, $C(\bar{x})$ is defined as:

$$C(\bar{x}) = \left\| \begin{array}{c} P_s^1(\bar{x}) - P_d^1(\bar{x}) \\ P_s^2(\bar{x}) - P_d^2(\bar{x}) \\ \vdots \\ P_s^N(\bar{x}) - P_d^N(\bar{x}) \end{array} \right\|^2 \quad (4-8)$$

For future use, $\bar{e}(\bar{x})$ is defined:

$$\bar{e}(\bar{x}) = \begin{bmatrix} e^1(\bar{x}) \\ e^2(\bar{x}) \\ \vdots \\ e^N(\bar{x}) \end{bmatrix} = \begin{bmatrix} P_s^1(\bar{x}) - P_d^1(\bar{x}) \\ P_s^2(\bar{x}) - P_d^2(\bar{x}) \\ \vdots \\ P_s^N(\bar{x}) - P_d^N(\bar{x}) \end{bmatrix} \quad (4-9)$$

The cost function can be modeled as locally quadratic by taking the first two terms in the Taylor series expansion as in (4-10).

$$C(\bar{x}_k + \bar{p}_k) \cong C(\bar{x}_k) + \bar{g}^T(\bar{x}_k)\bar{p}_k + \frac{1}{2}\bar{p}_k^T\bar{H}_k(\bar{x}_k)\bar{p}_k \quad (4-10)$$

In (4-10), the variables are defined as in Table 4-1:

Table 4-1 Definition of variables in (4-10).

\bar{x}_k	Unknown vector at k th iteration
\bar{p}_k	Perturbation vector at k th iteration
$\bar{g}_k(\bar{x}) = \nabla C(\bar{x})$	Gradient of C w.r.t. \bar{x} k th iteration
$\bar{H}_k(\bar{x}) = \nabla\nabla C(\bar{x})$	Hessian of C at k th iteration

The perturbation vector, \bar{p}_k is by definition:

$$\bar{p}_k = \bar{x}_{k+1} - \bar{x}_k \quad (4-11)$$

Since,

$$C(\bar{x}) = \bar{e}^T \bar{e} \quad (4-12)$$

$$\nabla C(\bar{x}) = 2\bar{J}^T \bar{e} \quad (4-13)$$

where \bar{J} is the $N \times M$ Jacobian matrix explicitly given in (4-14). Number of elements is assumed to be M .

$$\bar{J} = \begin{bmatrix} \frac{\partial e^1}{\partial x_1} & \frac{\partial e^1}{\partial x_2} & \cdots & \frac{\partial e^1}{\partial x_M} \\ \frac{\partial e^2}{\partial x_1} & \frac{\partial e^2}{\partial x_2} & \cdots & \frac{\partial e^2}{\partial x_M} \\ \vdots & \vdots & \ddots & \vdots \\ \frac{\partial e^N}{\partial x_1} & \frac{\partial e^N}{\partial x_2} & \cdots & \frac{\partial e^N}{\partial x_M} \end{bmatrix} \quad (4-14)$$

On the other hand, the Hessian matrix is calculated by:

$$\bar{H}(\bar{x}) = \nabla \nabla C(\bar{x}) = \begin{bmatrix} \frac{\partial^2 C}{\partial x_1 \partial x_1} & \frac{\partial^2 C}{\partial x_1 \partial x_2} & \cdots & \frac{\partial^2 C}{\partial x_1 \partial x_M} \\ \frac{\partial^2 C}{\partial x_2 \partial x_1} & \frac{\partial^2 C}{\partial x_2 \partial x_2} & \cdots & \frac{\partial^2 C}{\partial x_2 \partial x_M} \\ \vdots & \vdots & \ddots & \vdots \\ \frac{\partial^2 C}{\partial x_M \partial x_1} & \frac{\partial^2 C}{\partial x_M \partial x_2} & \cdots & \frac{\partial^2 C}{\partial x_M \partial x_M} \end{bmatrix} \quad (4-15)$$

When the m^{th} row of the Hessian is considered:

$$\begin{aligned} \left[\frac{\partial^2 C}{\partial x_m \partial x_1} \quad \frac{\partial^2 C}{\partial x_m \partial x_2} \quad \cdots \quad \frac{\partial^2 C}{\partial x_m \partial x_M} \right] &= \frac{\partial}{\partial x_m} \left[\frac{\partial C}{\partial x_1} \quad \frac{\partial C}{\partial x_2} \quad \cdots \quad \frac{\partial C}{\partial x_M} \right] \\ &= \frac{\partial}{\partial x_m} \{ \nabla C \}^T = \frac{\partial}{\partial x_m} \{ 2\bar{e}^T \bar{J} \} = 2 \frac{\partial \bar{e}^T}{\partial x_m} \bar{J} + 2\bar{e}^T \frac{\partial \bar{J}}{\partial x_m} \end{aligned} \quad (4-16)$$

Thus the Hessian becomes:

$$\bar{H}(\bar{x}) = 2\bar{J}^T \bar{J} + 2\bar{R} \quad (4-17)$$

where \bar{R} is an $M \times M$ matrix given as in (4-18).

$$\bar{R}(\bar{x}) = \sum_{m=1}^M e^m(\bar{x}) \bar{D}^m(\bar{x}) \quad (4-18)$$

$$\bar{D}^m(\bar{x}) = \begin{bmatrix} \frac{\partial^2 e^m}{\partial x_1 \partial x_1} & \frac{\partial^2 e^m}{\partial x_1 \partial x_2} & \cdots & \frac{\partial^2 e^m}{\partial x_1 \partial x_M} \\ \frac{\partial^2 e^m}{\partial x_2 \partial x_1} & \frac{\partial^2 e^m}{\partial x_2 \partial x_2} & \cdots & \frac{\partial^2 e^m}{\partial x_2 \partial x_M} \\ \vdots & \vdots & \ddots & \vdots \\ \frac{\partial^2 e^m}{\partial x_M \partial x_1} & \frac{\partial^2 e^m}{\partial x_M \partial x_2} & \cdots & \frac{\partial^2 e^m}{\partial x_M \partial x_M} \end{bmatrix}$$

The numerical computation of $\bar{D}^m(\bar{x})$ is very expensive and sensitive to finite precision errors. Besides, the relatively small magnitude of the second derivatives and the possible random (with zero mean) nature of \bar{e} encourage discarding this matrix. Thus the Hessian can be approximated as:

$$\bar{H}(\bar{x}) \cong 2\bar{J}^T \bar{J} \quad (4-19)$$

4.2.1 Newton Minimization

The cost function given in (4-10) is minimized when \bar{p}_k is the minimum of the quadratic form:

$$Q(\bar{p}_k) = \bar{g}^T(\bar{x}_k) \bar{p}_k + \frac{1}{2} \bar{p}_k^T \bar{H}_k(\bar{x}_k) \bar{p}_k \quad (4-20)$$

As the Hessian is approximated as in (4-19), positive definiteness is guaranteed and $Q(\bar{p}_k)$ and therefore the cost function is convex. To find the \bar{p}_k vector that minimizes the cost function, the gradient of $Q(\bar{p}_k)$ is calculated and equated to zero. When this is done, \bar{p}_k^{min} is found as:

$$\bar{p}_k^{min} = -\{\bar{H}_k(\bar{x}_k)\}^{-1} \bar{g}(\bar{x}_k) \quad (4-21)$$

This approach requires the invertibility and the inversion of the Hessian matrix. When the number of unknowns is large, this method is avoided. In reflectarray optimization, the number of unknowns is moderate but it is observed that the Hessian matrix has a very large condition number. Largeness of the condition number results in unreasonable perturbations.

Note that when Hessian matrix is approximated as in (4-19), (4-21) is equal to:

$$\bar{p}_k^{min} = -[\bar{J}^T \bar{J}]^{-1} \bar{J}^T \bar{e} \quad (4-22)$$

Thus, Newton minimization is equivalent to solving the system:

$$\bar{e}(\bar{x}) = \bar{0} \quad (4-23)$$

by the multivariate Newton – Raphson scheme:

$$\bar{x}_k = \bar{x}_{k-1} - [\bar{J}^T \bar{J}]^{-1} \bar{J}^T \bar{e}(\bar{x}_{k-1}) \quad (4-24)$$

4.2.2 The Method of Steepest Descent

In the method of steepest descent, it is not necessary to invert the Hessian matrix. Instead the search direction is chosen to be along the opposite of the gradient direction and the solution vector is modified at each iteration along this direction as:

$$\bar{x}_{k+1} = \bar{x}_k - \gamma_k \bar{g}(\bar{x}_k) \quad (4-25)$$

The factor γ_k can be chosen with two different approaches:

- A line search that minimizes $C(\bar{x})$, along $\bar{g}(\bar{x}_k)$.
- By using the quadratic approximation in (4-10):

$$C(\bar{x}_{k+1}) \cong C(\bar{x}_k) - \gamma_k \|\bar{g}(\bar{x}_k)\|^2 + \frac{\gamma_k^2}{2} \bar{g}^T(\bar{x}_k) \bar{H}_k(\bar{x}_k) \bar{g}(\bar{x}_k) \quad (4-26)$$

The minimum value of (4-26) occurs for:

$$\gamma_k = \frac{\|\bar{g}(\bar{x}_k)\|^2}{\bar{g}^T(\bar{x}_k) \bar{H}_k(\bar{x}_k) \bar{g}(\bar{x}_k)} \quad (4-27)$$

4.2.3 The Conjugate Gradient Method

The conjugate gradient method, originally derived for solution of linear equation systems, was adapted for non-linear systems by Fletcher and Reeves [47]. In this

method the search direction is a linear combination of the current gradient and the previous search direction. With \bar{s}_k representing the search direction in k^{th} iteration,

$$\bar{s}_k = -\bar{g}(\bar{x}_k) + \beta_k \bar{s}_{k-1}, \quad \bar{s}_0 = -\bar{g}(\bar{x}_0) \quad (4-28)$$

Different versions of the parameter β_k have been a research topic since the work of Fletcher and Reeves. For a detailed review on different forms of β_k , [48] can be referred, but in this study original β_k proposed by Fletcher and Reeves given in (4-29) is used.

$$\beta_k = \frac{\|\bar{g}(\bar{x}_k)\|^2}{\|\bar{g}(\bar{x}_{k-1})\|^2} \quad (4-29)$$

Again the coefficient of \bar{s}_k is found by replacing $g(\bar{x}_k)$ by \bar{s}_k .

$$\gamma_k = \frac{\|\bar{s}_k\|^2}{\bar{s}_k^T \bar{H}_k(\bar{x}_k) \bar{s}_k} \quad (4-30)$$

4.2.4 Application of the Optimization Methods to Reflectarray Design

Above mentioned three methods are attempted to use for reflectarray design. Actually, the reflectarray optimization problem has the following handicaps in terms of its suitability to application of directional search based optimization algorithms:

- The problem is not globally convex within the entire domain of input variables, \bar{x} . This results in a great likelihood of trapping in local minima.
- The input variables, \bar{x} , are bounded by lower and upper limits due to physical restrictions. Nevertheless, updates demanded by the directional search algorithms are not bounded.
- The cost function given in (4-7) is not ideal for most cases, because it does not make a practically reasonable treatment of the sidelobe region where a level lower than the desired upper sidelobe bound is actually not harmful at all. However, minimizing (4-7) could deliberately rise the sidelobe level to the desired upper limit.

Ad-hoc remedies are produced to alleviate these problems:

- The initial points in optimization are not selected arbitrarily. Instead, the design provided by the infinite array approach is chosen as a starting point, which can be assumed close enough to the desired solution.
- Whenever a lower or upper bound is encountered for the size of an element, the element size is hard-limited to the maximum or minimum allowed value. If this precaution does not turn out to be suitable, following transformation can be tried in order to map the allowable size values to the interval $(-\infty, +\infty)$.

$$x = \frac{(x_{max}+x_{min})}{2} + \frac{(x_{max}-x_{min})}{2} \sin(y), y \in (-\infty, +\infty) \quad (4-31)$$

- The sidelobe levels in desired patterns are set to a reasonable level such that the error contribution in sidelobe region does not jeopardize the synthesis by attempting to attain a very low sidelobe level.

To make a concept demonstration, a sample and relatively small reflectarray problem is considered:

- Substrate thickness: 1.59 mm, Substrate $\epsilon_r=4.2$.
- Frequency: 10 GHz.
- Reflectarray size: 20 elements \times 20 elements.
- Spacing between elements: 0.6λ in both dimensions.
- Distance to feed antenna: 6.67λ .
- Feed antenna: Horn antenna with aperture dimensions of $1.3\lambda_0 \times 0.58\lambda_0$.
- Desired patterns:
 - Cosecant squared beam in elevation and Gaussian beam in azimuth.
 - A non – separable constant illumination pattern.

The starting point is either provided by the infinite array approach, discarding the effect of incidence angles or chosen as a uniform sized array. The derivatives required by the Jacobian matrix are approximated by the central differences with the exception for size values at upper and lower limits. For the minimum possible size

the derivative is approximated by forward difference whereas the derivative for the maximum possible size is approximated by backward difference. In the computation of the Jacobian matrix, only the rows and columns of the \tilde{Z} matrix associated with the considered element is updated and filling the entire \tilde{Z} matrix is avoided. In the far field calculation required for the Jacobian matrix, only the pattern of the considered element is updated. With these precautions, a significant acceleration in calculation of Jacobian matrix is achieved, compared to evaluation of $\bar{e}(\bar{x})$. In this particular example, the far field pattern is sampled at principal planes only since the pattern is separable in these planes and the initial design is to be perturbed by a little amount.

The relative scaling between the desired and the synthesized far field patterns is very important in terms of the optimization. It is not useful to normalize both patterns so that their peak level is zero dB, because this spoils the correct derivative information. To have the correct derivative information, the classical approach is to normalize both desired and synthesized patterns to their respective directivities. But this would involve computing the directivity of the synthesized pattern at each iteration, including Jacobian matrix computation. To avoid the computational cost of directivity computation, an alternative method is adopted. In equations (4-7), (4-8) and (4-9), the electric field intensity in the far field that would be generated by the desired pattern is subtracted from the electric field intensity of the synthesized pattern in the far field, which is readily available in each iteration. This technique results in a correct relative scaling of the desired and synthesized patterns. The electric field intensity that would be generated by the desired pattern is found by:

$$P_d(R_0, \theta, \varphi) = \frac{P_T D_d}{4\pi R_0^2} \quad (4-32)$$

where P_T , D_d , and R_0 stand for the radiated power, directivity of the desired pattern and the observation distance respectively. The patterns that will be presented correspond to main-polarization, and cross polarization patterns will not be examined, because cross polarization is neither the concern of this study, nor it is expected to suffer a high cross polarization level.

4.2.4.1 Newton Minimization

Newton Minimization is not possible because the condition number of Hessian matrix at the first iteration is about 10^{20} . The perturbation provided by Newton minimization approach resulted in excessively large positive and even negative patch sizes.

4.2.4.2 The Method of Steepest Descent

For the method of steepest descent, two alternatives for the selection of parameter γ_k is tried. The starting point in both cases is the draft design provided by the infinite array approach.

4.2.4.2.1 The Method of Steepest Descent with Line Search

In this scheme, the parameter γ_k is chosen according to the reduction in the cost function. For this purpose, a fine scan followed by a rough one is executed. That is, γ_k is swept by large steps in a reasonable interval and then it is swept by fine steps about the point where the current cost function is minimum. The final value of γ_k is determined by the minimum cost function that can be obtained in this step.

The iterations are terminated by visually inspecting the synthesized patterns. It takes 10 iterations to obtain a satisfactory pattern in both principal planes. The azimuth and elevation patterns at the beginning of the iterations are given in Figure 4-9 and Figure 4-10.

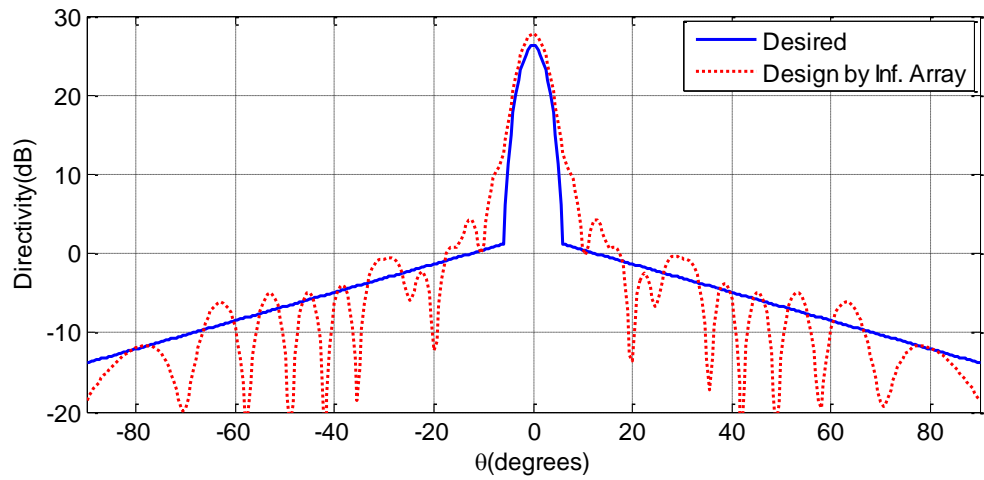


Figure 4-9 Desired azimuth pattern and the azimuth far field result of the design made by infinite array approach.

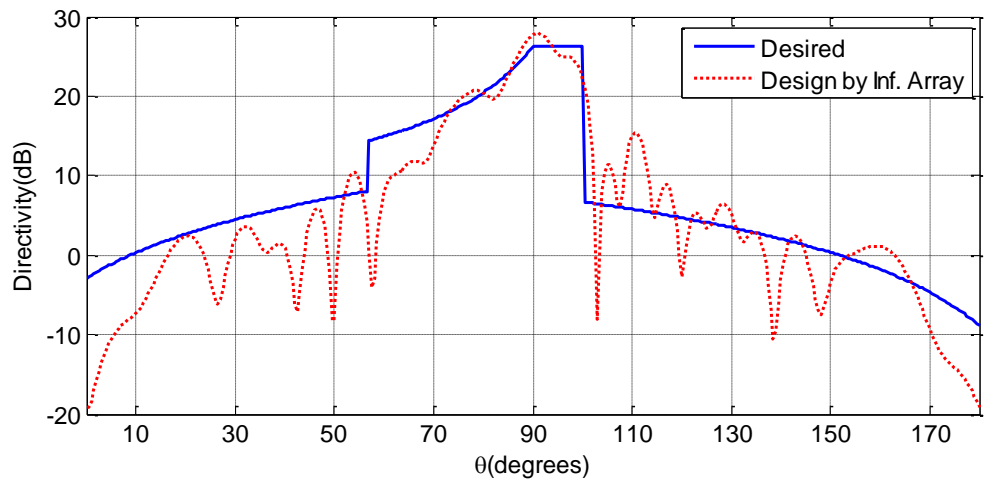


Figure 4-10 Desired elevation pattern and the elevation far field result of the design made by infinite array approach.

The patterns after ten iterations made with line search are given in Figure 4-11 and Figure 4-12. Comparisons with the initial patterns can also be observed on these figures. It is recognized that the optimization improves the initial patterns to a great extent in terms of agreement with the desired patterns.

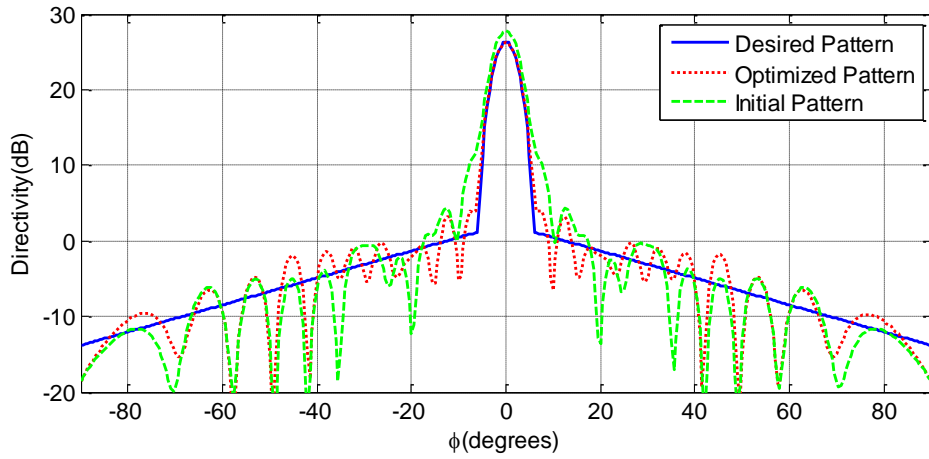


Figure 4-11 Desired azimuth pattern and the azimuth far field result of the design after steepest descent optimization with line search.

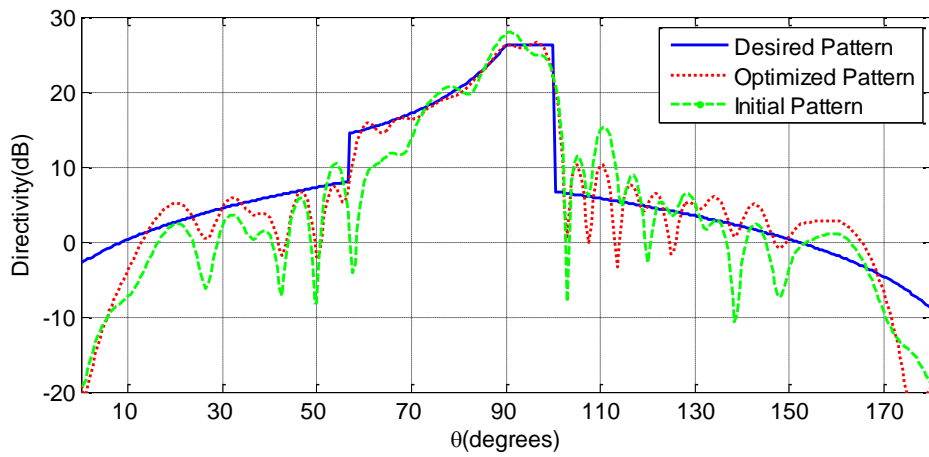


Figure 4-12 Desired elevation pattern and the elevation far field result of the design after steepest descent optimization with line search.

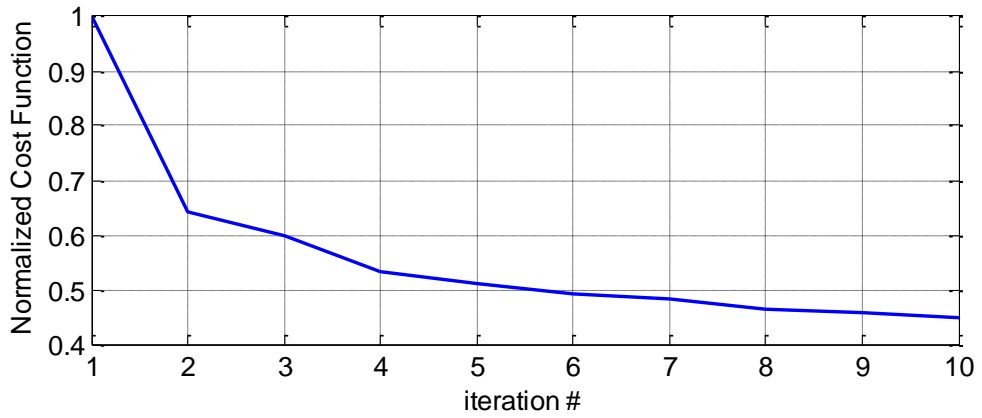


Figure 4-13 Variation of cost function with iterations, normalized to initial cost function.

Although the cost function is defined such that it accumulates the pattern errors in principal planes only, the pattern in the entire half sphere in front of the reflectarray is satisfactory, as seen in Figure 4-14.

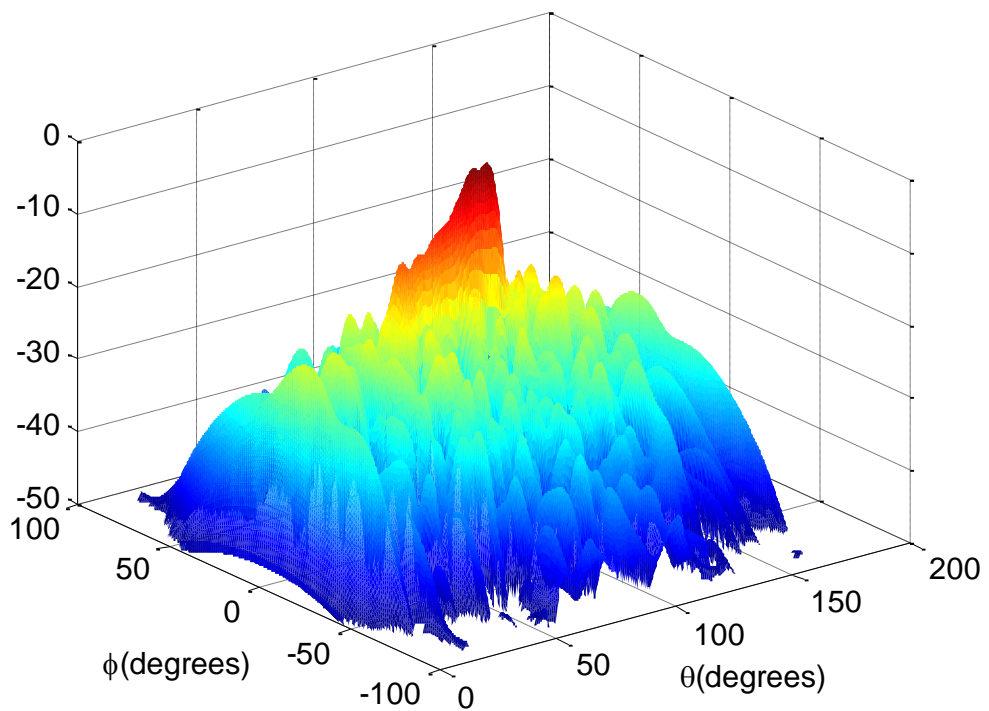


Figure 4-14 3-dimensional view of the optimized reflectarray pattern.

The difference between the optimized patch dimensions and initial patch dimensions can be observed in Figure 4-15.

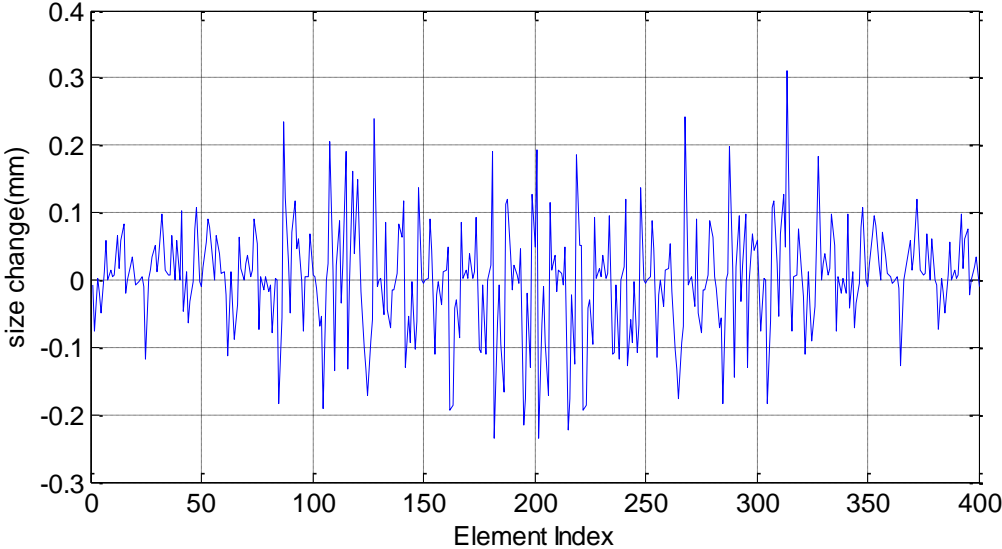


Figure 4-15 Difference of optimized and initial patch sizes in mm.

This optimization takes an overall duration of 990 seconds, with an average duration of 99 seconds per iteration. In each iteration, approximately 46 seconds is spent for line search and 53 seconds is spent for cost function and Jacobian matrix evaluation.

4.2.4.2.2 The Method of Steepest Descent with Equation (4-27)

Although the line search takes very few iterations to obtain a good design, the duration of line search at each iteration is quite long. Therefore, it is worth trying (4-27) because in that case, line search is not executed and number of cost function evaluations is reduced. The expected drawback is slow convergence and therefore increased number of iterations. When this approach is implemented, it is observed that the same value of the cost function with previous case is achieved after 111 iterations as seen in Figure 4-16. As the computation of the Jacobian matrix and the cost function takes 46 seconds, the total time spent is about 5106 seconds, which is far longer than that spent in the previous experiment.

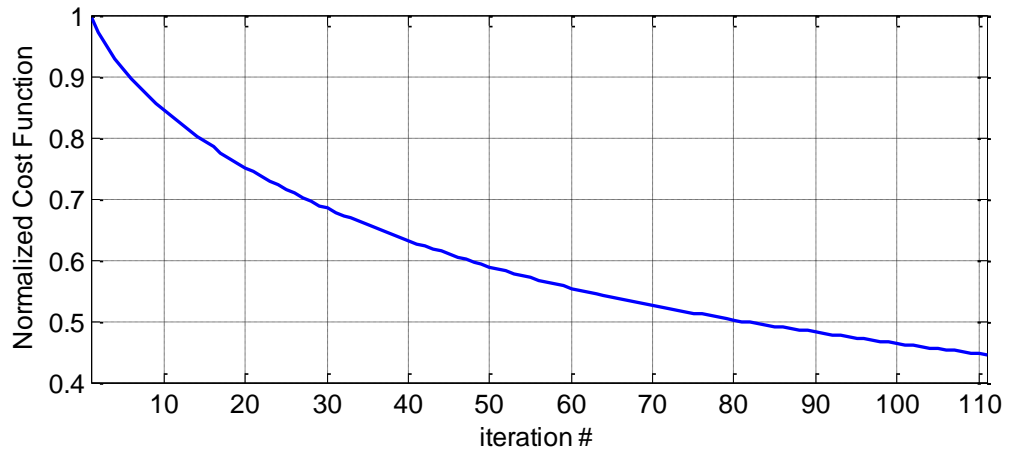


Figure 4-16 Variation of cost function with iterations, normalized to initial cost function.

4.2.4.3 The Conjugate Gradient Method

The conjugate gradient method is known to be providing faster convergence than the steepest descent Method. Thus conjugate gradient method is also applied to the solution of the same problem with the same initial sizes. It takes 13 iterations and $13 \times 46 = 198$ seconds to achieve a similar cost level. However, the algorithm starts to diverge after the 13th iteration.

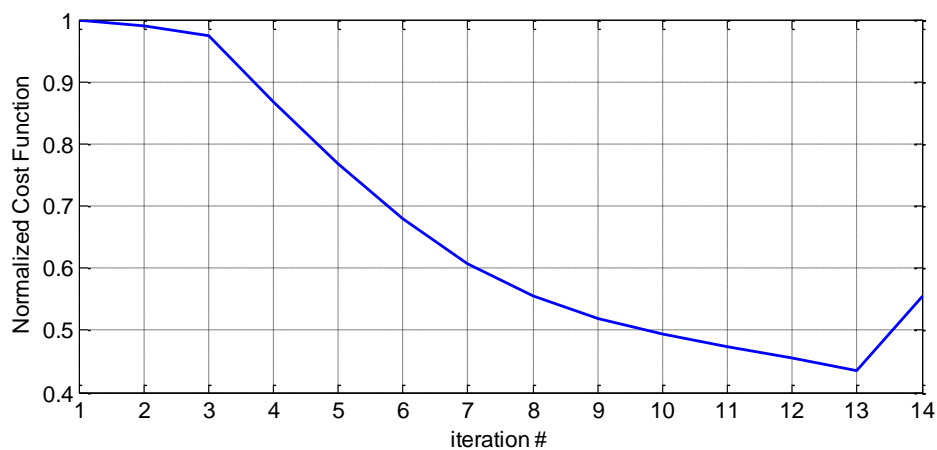


Figure 4-17 Variation of cost function with iterations, normalized to initial cost function.

4.2.4.4 Non Separable Pattern Synthesis

In many satellite antenna applications, desired antenna patterns are not separable into desired elevation and desired azimuth patterns because of specific regional coverage requirements. This case is studied for the optimization. The desired pattern is postulated as a constant illumination in a triangular sector as shown in Figure 4-18.

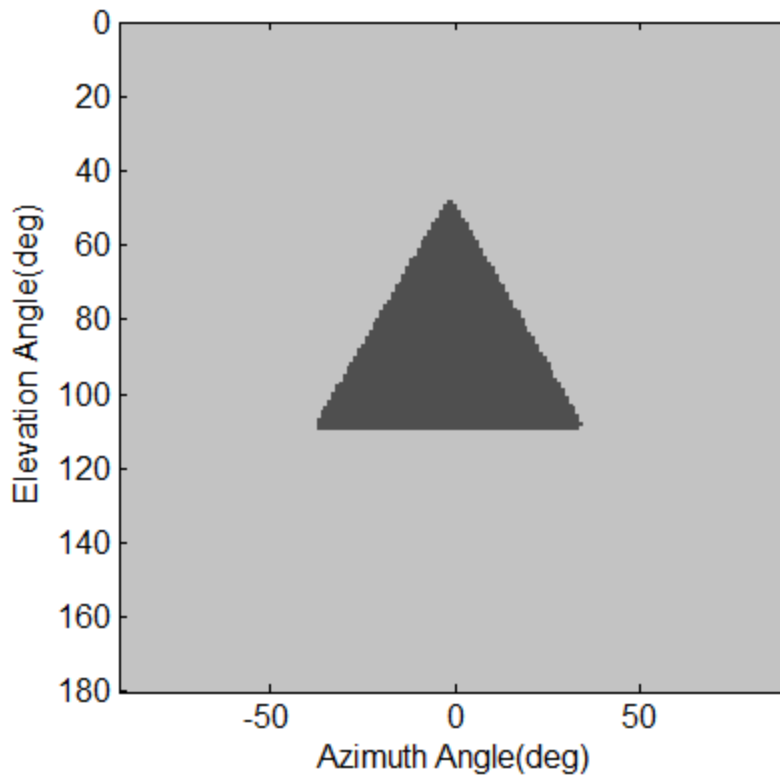


Figure 4-18 Desired pattern for the non-separable pattern synthesis.

The starting point is chosen as a uniform array with resonant patch sizes. Steepest descent with line search is applied. The descent of the cost function with iterations is given in Figure 4-19. The optimized pattern can be inspected in Figure 4-20. The peak to peak ripple level in the illumination sector is about 3 dB. The general sidelobe level is around 15 dB with a few exceptions of 10 dB.

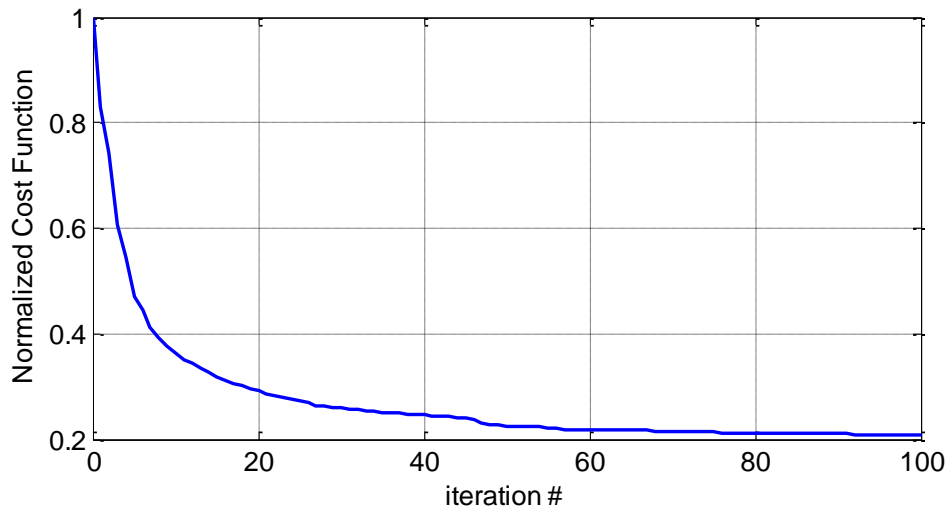


Figure 4-19 Variation of cost function with iterations, normalized to initial cost function.

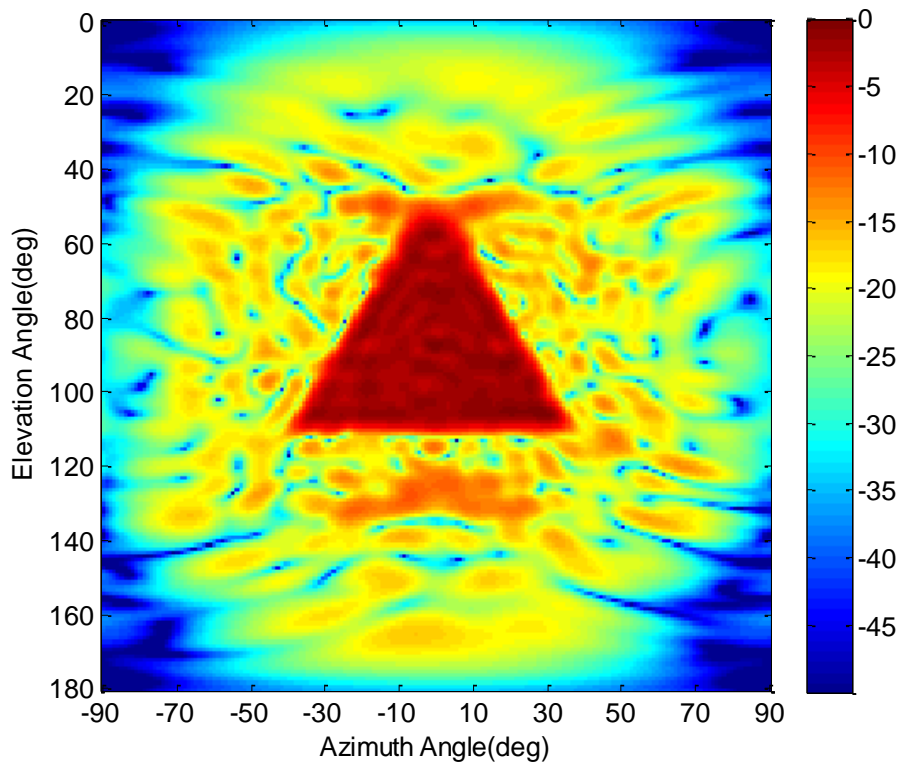


Figure 4-20 Optimized pattern after 100 iterations.

4.3 Verification of the Designs

In this part, the designs made above are verified by analyzing the associated reflectarray problems in HFSS.

4.3.1 Separable Pattern

The reflectarray optimized in Section 4.2.4.2 is analyzed by HFSS Finite Element Solver on a PC with 12 CPUs and 72 Gbytes RAM. In the final pass, HFSS uses 52.9 Gbytes RAM and 2132522 tetrahedral elements. The solution time is 2 hours and 17 minutes. Final delta energy (change of total energy w.r.t. the previous pass) is 2.5%. The result obtained in HFSS is compared to the result obtained in the optimization phase in principal planes in Figure 4-21 and Figure 4-22. Good agreement between the fast analysis and HFSS result is observed. The disagreement at the end – fire angles are probably due to the difference of the computational approach in HFSS and developed MoM technique, but these angular regions are usually of little practical importance. If the reference solution was able to be obtained by MoM, the agreement could be as good as those in Figure 2-32 and Figure 2-33.

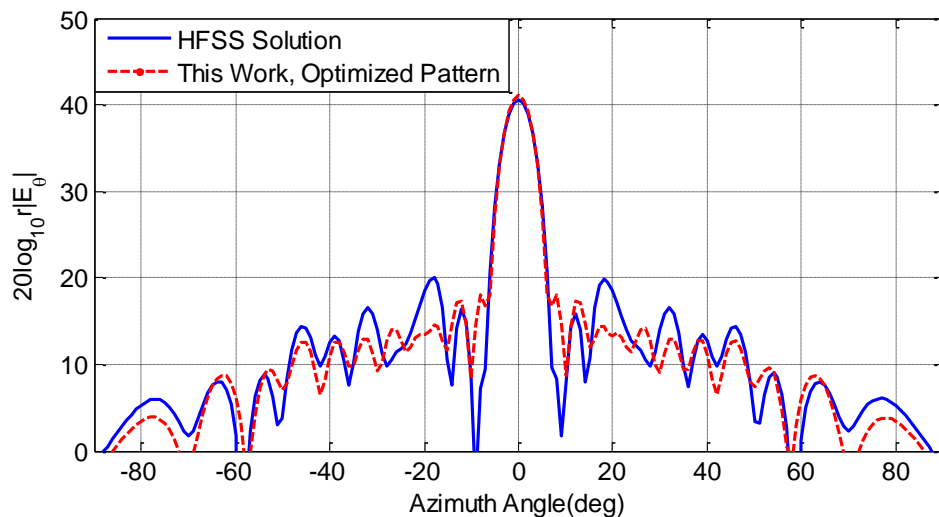


Figure 4-21 Comparison of the HFSS solution with the pattern synthesized during optimization in H plane.

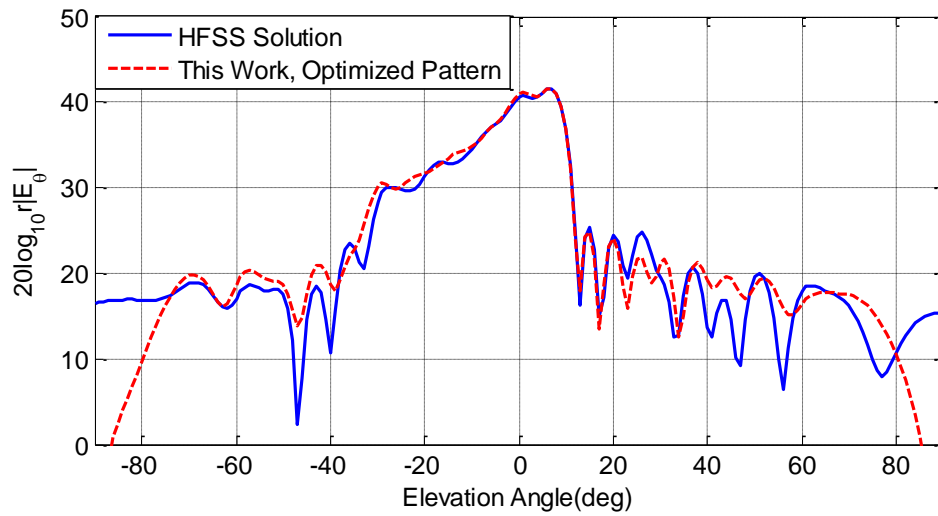


Figure 4-22 Comparison of the HFSS solution with the pattern synthesized during optimization in E plane.

4.3.2 Non-Separable Pattern

The reflectarray that is supposed to generate the pattern given in Figure 4-20 is analyzed in HFSS and the result is plotted in Figure 4-23. For better visualization for comparison, the patterns in principal planes are plotted on top of each other in Figure 4-24 and Figure 4-25. In HFSS the solution time is 2 hours and 2 minutes. Total number of tetrahedral elements is 2574001. With the available 72 Gbytes RAM, it was possible to make 16 adaptive passes where the RAM usage in the last adaptive pass is 60.4 Gbytes. Final delta energy (change of total energy w.r.t. the previous pass) is 3.5%, which means that the solution may need to be improved further.

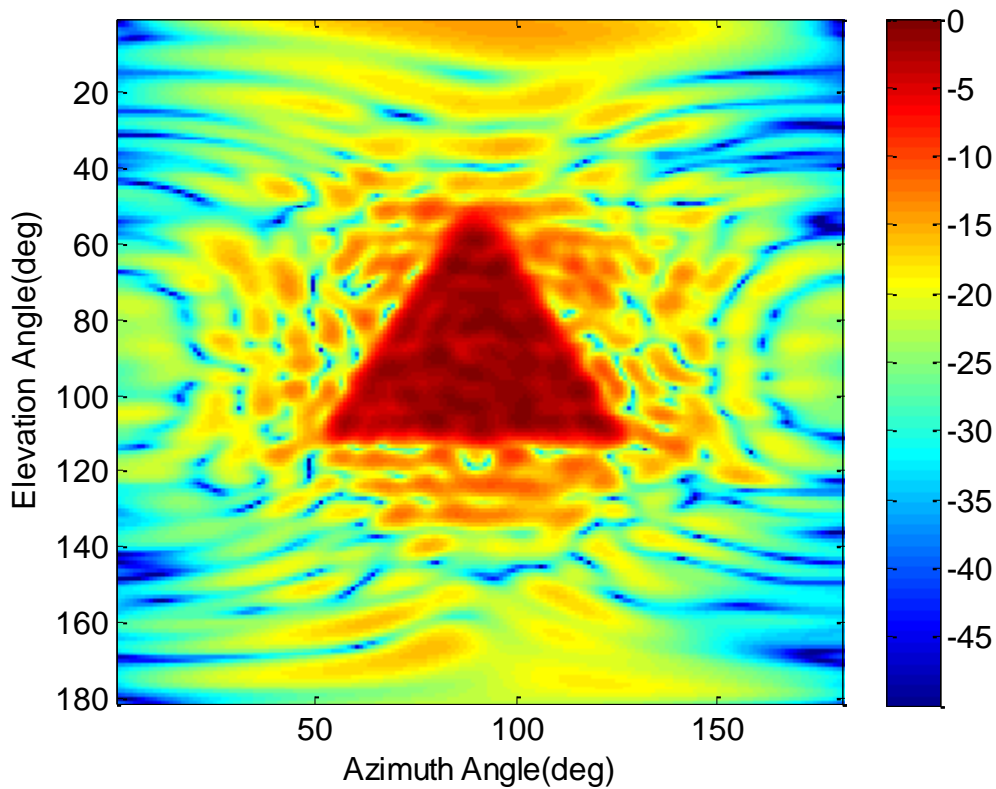


Figure 4-23 HFSS result of the reflectarray optimized to yield the non-separable pattern.

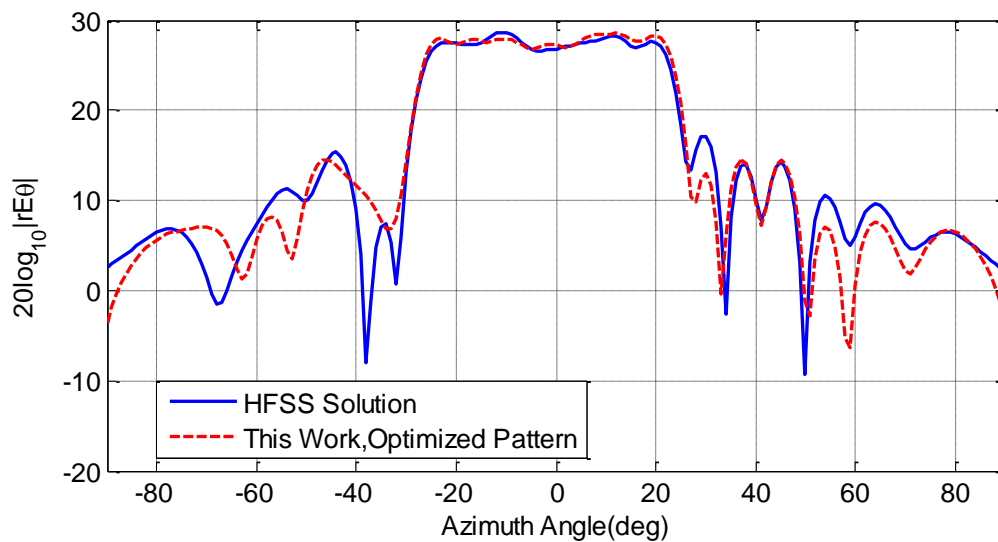


Figure 4-24 Comparison of the HFSS solution with the pattern synthesized during optimization in H plane.

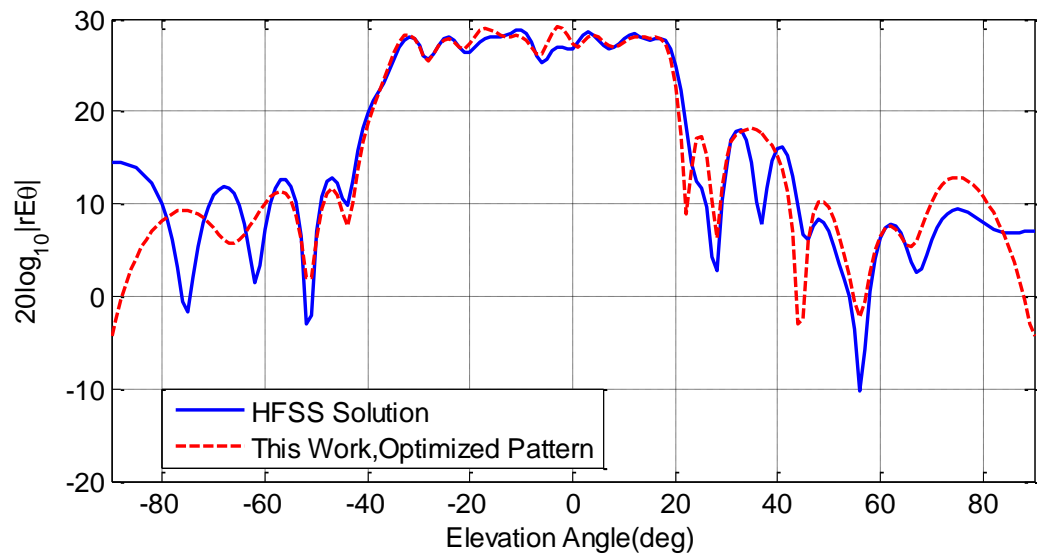


Figure 4-25 Comparison of the HFSS solution with the pattern synthesized during optimization in E plane.

4.4 Conclusions

In this chapter, it is shown that the fast solution method developed in Chapter 2 can be used as a design tool with the help of directional search algorithms. Various types of optimization methods are investigated and compared. It is observed that the conjugate gradient method and the steepest descent method are both successful in terms of obtaining a satisfactory match to the desired pattern. Although it is observed that the conjugate gradient method requires less optimization time, this result is specific to the analyzed problem and should not be generalized. The reflectarray designs made by optimization are analyzed and verified in a different full wave solver, which can be regarded as a reference tool in academic studies and an industry standard in engineering applications.

CHAPTER 5

CONCLUSIONS

In this thesis, an efficient and very fast analysis technique for reflectarrays of variable element sizes is established. As compared to acceleration methods like MLFMA, it is quite simpler to implement the technique with legacy MoM codes. The method is more accurate than the local periodicity, or infinite array approach, because it takes the real electromagnetic environment around all elements into account. Owing to the drastic reduction in computation times offered by the method, it becomes possible to employ directional search based optimization algorithms for design. The efficiency of the technique relies on usage of characteristic modes as macro basis functions and reducing the number of unknowns by using only a few of the characteristic modes. The technique is first applied to reflectarrays composed of variable-size square patches. It is observed that, as far as the far field is concerned, a single characteristic mode yields sufficient accuracy. It is further observed that, when the mesh on each patch is a scaled replica of a reference mesh, the dominant characteristic mode of the resonant patch can be used for all differently sized patches on the array. As the formulation that enables usage of characteristic modes and leads to the matrix reduction still requires the computation of the conventional MoM matrix, the ways of efficiently computing the reduced matrix is sought. As a remedy, tabulation of the reduced matrix entries is proposed. Considering that a particular term of the reduced matrix is a function of the mutual impedance matrix of two patches in the array, the number of possible combinations of patch sizes and displacements for a practical reflectarray is very huge, if not infinite. To resolve this problem, the reduced matrix term is studied in detail. It is realized that the reduced matrix term, which depends on the relative displacement of patches and sizes of source and observation patches, can be approximated as the product of a function of patch sizes and a function of two dimensional displacements. The exceptions to this

rule are the close neighboring patches and are of manageable count. For a substrate with a thickness of 1.59 mm and a relative permittivity of 4.2, the number of close neighbors that needs to be considered without separability is 24. For all these displacement types, sizes of observation and source patches are to be swept. For all further displacements, only two tabulations are required. One of these tabulations is done with fixed source and observation patch sizes for every possible neighboring types of the largest size reflectarray to be designed. The other tabulation is done at a fixed displacement for all possible combinations of source and observation patch sizes. When these three tabulations are at hand, the whole reduced matrix for any given reflectarray can be found and inverted in a matter of seconds. For instance, it takes 0.38 seconds to fill and invert the reduced matrix of a 1000 element reflectarray on a personal computer with 3.3 GHz CPU clock speed.

Even though the method was developed for reflectarrays with square patches, it was customized for reflectarrays comprised of different element types. One other element type that was attempted is a wideband element consisting of a square patch and an outer ring surrounding this patch. For this element, resonance does not exist, but the distinct metal parts are resonant. Therefore it is proposed to use the dominant characteristic modes of the resonant square patch and resonant outer ring as macro basis functions and reuse them for all elements on the reflectarray. This proposition is tested on a medium size reflectarray for plane waves with various incidence angles and it was observed that a fair approximation of the far field is achievable. The separability was investigated and seen to be valid for distant self and mutual interactions of proposed basis functions.

The method is extended for another element type, the split ring resonator which is used in circularly polarized reflectarrays. The reflection phase of this element is altered by rotating it. Thus the element geometry remains invariant throughout the reflectarray and its characteristic modes do not depend on the rotation unless each element is meshed differently. Having the reusability of the characteristic modes already, the accuracy of using a few characteristic modes and separability are investigated. It was recognized that a single mode does not provide sufficient

accuracy even in the far field. On the other hand when 4 modes are taken, the error in the current density was as low as 4% even for a very large incidence angle and perfect agreement between the far fields of conventional MoM and the reduced matrix solution was possible. It was observed that the reduced matrix terms are not exactly separable into the functions of two or three sets of the associated variables, but they can be estimated accurately by considering the samples of the entire function on two orthogonal planes of the domain of the variables (distance, polar angle, and rotation). These two examples demonstrate that the proposed method that is readily applicable for reflectarrays of square patches can be customized for reflectarrays of different element types, but each element type considered may require special attention and specific adaptation. The fast solution method therefore can be perceived to be proposing a general philosophy for the efficient analysis of different types of reflectarrays. The critical requirement of the proposed method is the availability of a practical means of estimating or computing the reduced matrix entries, which can be the interaction of a single type of CM or two different types of CMs on two elements. This availability may manifest itself by:

- The separability of the function that yields the reduced matrix term, in terms of subgroups of variables,
- The possibility of estimating the reduced matrix terms by means of the projections of the function yielding the reduced matrix term onto subdomains,
- The possibility of ignoring interactions beyond some specific distance,
- The possibility of fitting the reduced matrix terms to an explicit function, etc.

There is certainly no guarantee of having any of these conditions for an arbitrary reflectarray configuration, given the frequency and substrate properties. However, it is worth studying the applicability of the fast solution due to the accuracy and speed it might offer.

As the proposed method is very promising in terms of solution times, it is possible to employ it as an analysis tool for the optimization algorithms such as the Method of Steepest Descent or the Conjugate Gradient Method. These methods require changing one of the input variables while keeping others same and measuring the effect in the output for Jacobian matrix evaluation. For the computation of the

Jacobian matrix, as a large part of the reduced matrix remains unchanged, the matrix fill time is minimized by modifying only the terms associated with the element under consideration. The function evaluation time is also minimized by precomputing the element patterns and constructing the far field by superposition. It is shown by an example that using the proposed fast analysis technique and the method of steepest descent, a 400 element reflectarray is optimized by making 10 iterations within 990 seconds, when the initial point of optimization is chosen as the design provided by the infinite array approach. For another example problem where the initial point is chosen as a uniform array of resonant patches, it took 100 iterations and 9900 seconds to achieve the desired non-separable pattern. It can be concluded that the infinite array approach yields a good starting point in terms of closeness to the local minimum. In order to verify the designs, the problems are modeled and analyzed in HFSS. It was seen that the far field patterns calculated by fast analysis are in good agreement with those calculated by HFSS.

A probable extension of the proposed method is the fast analysis of aperiodic and variable element size reflectarrays. These structures, being both aperiodic and non-uniform, are even more unsuitable for the local periodicity approach and thus cannot be analyzed accurately with it. For the periodic problems analyzed in this study, the reduced matrix terms are tabulated for discrete and periodic samples of horizontal and vertical displacements. However, as the reduced matrix terms should most of the time vary smoothly by distance, intermediate positioning of elements can be handled by the help of interpolation. A problematic issue that can be expected due to aperiodicity could be the interactions involving close neighbors, but it can be projected that those interactions can also be interpolated for intermediate displacements by special attention.

Another valuable extension of the proposed method could be the application to multilayer reflectarrays. This is a big challenge because it would require computation of the coupling of the CMs of patches closely stacked in the same unit cell, which has quite a different nature than the coupling of elements distributed over the same substrate.

REFERENCES

- [1] J. A. Encinar, "Design of two-layer printed reflectarrays using patches of variable-size," *IEEE Trans. Antennas Propag.*, vol. 49, no. 10, pp. 1403–1410, 2001.
- [2] J. Huang, "Bandwidth study of microstrip reflectarray and a novel phased reflectarray concept," in *IEEE Antennas and Propagation Society International Symposium Digest*, vol. 1, pp. 582–585, 1995.
- [3] S. R. Rengarajan, "Design and analysis of microstrip reflectarray antennas," in *2009 Applied Electromagnetics Conference (AEMC)*, 2009.
- [4] M. Zhou, S. B. Sorensen, O. S. Kim, E. Jorgensen, P. Meincke, and O. Breinbjerg, "Direct optimization of printed reflectarrays for contoured beam satellite antenna applications," *IEEE Trans. Antennas Propag.*, vol. 61, no. 4, pp. 1995–2004, Apr. 2013.
- [5] S. V. Hum, M. Okoniewski, and R. J. Davies, "Realizing an electronically tunable reflectarray using varactor diode-tuned elements," *IEEE Microw. Wirel. Components Lett.*, vol. 15, no. 6, pp. 422–424, Jun. 2005.
- [6] R. Sorrentino, "MEMS-based reconfigurable reflectarrays," *The 2nd European Conference on Antennas and Propagation*, Edinburgh, UK, 11-16 November 2007.
- [7] O. Bayraktar, O. A. Civi, and T. Akin, "Beam switching reflectarray monolithically integrated with RF-MEMS switches," *IEEE Trans. Antennas Propag.*, vol. 60, no. 2, pp. 854–862, Feb. 2012.
- [8] T. A. Metzler, "Stub loaded microstrip reflectarrays," in *IEEE Antennas and Propagation Society International Symposium Digest*, vol. 1, pp. 574–577, 1995.
- [9] D. M. Pozar and T. A. Metzler, "Analysis of a reflectarray antenna using microstrip patches of variable-size," *Electronics Letters*, pp. 657-658, Apr. 1993.
- [10] J. Huang and R. J. Pogorzelski, "A Ka-band microstrip reflectarray with elements having variable rotation angles," *IEEE Trans. Antennas Propag.*, vol. 46, no. 5, pp. 650–656, May 1998.

- [11] J. Huang and J. A. Encinar, *Reflectarray Antennas*, Hoboken, NJ, USA: John Wiley & Sons, Inc., 2007.
- [12] W. Chew, J. Jin, E. Michielssen, and J. M. Song, *Fast and Efficient Algorithms in Computational Electromagnetics*, Artech House, Norwood, 2001.
- [13] E. Michielssen and A. Boag, "A multilevel matrix decomposition algorithm for analyzing scattering from large structures," *IEEE Trans. Antennas Propag.*, vol. 44, no. 8, pp. 1086–1093, 1996.
- [14] K. Zhao, M. N. Vouvakis, and J.-F. Lee, "The adaptive cross approximation algorithm for accelerated method of moments computations of EMC problems," *IEEE Trans. Electromagn. Compat.*, vol. 47, no. 4, pp. 763–773, Nov. 2005.
- [15] M. Bercigli, M. Bandinelli, P. De Vita, A. Freni, G. Vecchi, "Acceleration methods for full-wave modelling of reflectarrays," *The 2nd European Conference on Antennas and Propagation*, Edinburgh, UK, 11-16 November 2007.
- [16] L. Matekovits, V. A. Laza, and G. Vecchi, "Analysis of large complex structures with the synthetic-functions approach," *IEEE Trans. Antennas Propag.*, vol. 55, no. 9, pp. 2509–2521, Sep. 2007.
- [17] P. De Vita, A. Freni, F. Vipiana, P. Pirinoli, and G. Vecchi, "Fast analysis of large finite arrays with a combined multiresolution – SM/AIM approach," *IEEE Trans. Antennas Propag.*, vol. 54, no. 12, pp. 3827–3832, Dec. 2006.
- [18] I. Gonzalez, A. Tayebi, J. Gomez, C. Delgado, F. Catedra, "Fast analysis of a dual-band reflectarray using two different numerical approaches based on the moment method," *IEEE Trans. Antennas Propag.*, vol. 61, no. 4, pp. 2333–2336, April 2013.
- [19] J. A. Encinar, "Recent advances in reflectarray antennas," *The 4th European Conference on Antennas and Propagation*, Barcelona, Spain, 12-16 April 2010.
- [20] M. Arrebola, R. Cahill, J. A. Encinar, V. Fusco, H. S. Gamble, Y. Alvarez, and F. Las-Heras, "94 GHz dual-reflector antenna with reflectarray subreflector," *IEEE Trans. Antennas Propag.*, vol. 57, no. 10, pp. 3043–3050, Oct. 2009.

- [21] H. Rajagopalan, S. Xu, and Y. Rahmat-Samii, “Experimental demonstration of reflectarrays acting as conic section subreflectors in a dual reflector system,” *IEEE Trans. Antennas Propag.*, vol. 61, no. 11, pp. 5475–5484, Nov. 2013.
- [22] F. Venneri, G. Angiulli, and G. Di Massa, “Design of microstrip reflect array using data from isolated patch analysis,” *Microw. Opt. Technol. Lett.*, vol. 34, no. 6, pp. 411–414, Sep. 2002.
- [23] F. Venneri, S. Costanzo, G. DiMassa, and G. Angiulli, “An improved synthesis algorithm for reflectarrays design,” *Antennas Wirel. Propag. Lett.*, vol. 4, no. 1, pp. 258–261, 2005.
- [24] M.-A. Milon, D. Cadoret, R. Gillard, and H. Legay, “‘Surrounded-element’ approach for the simulation of reflectarray radiating cells,” *IET Microwaves, Antennas Propag.*, vol. 1, no. 2, p. 289, Apr. 2007.
- [25] P. Nayeri, A. Z. Elsherbeni, and F. Yang, “Radiation analysis approaches for reflectarray antennas [Antenna Designer’s Notebook],” *IEEE Antennas Propag. Mag.*, vol. 55, no. 1, pp. 127–134, Feb. 2013.
- [26] E. Carrasco, M. Barba, J. A. Encinar, M. Arrebola, F. Rossi, and A. Freni, “Design, manufacture and test of a low-cost shaped-beam reflectarray using a single layer of varying-sized printed dipoles,” *IEEE Trans. Antennas Propag.*, vol. 61, no. 6, pp. 3077–3085, Jun. 2013.
- [27] F.-C. E. Tsai and M. E. Bialkowski, “Designing a 161-element Ku-band microstrip reflectarray of variable-size patches using an equivalent unit cell waveguide approach,” *IEEE Trans. Antennas Propag.*, vol. 51, no. 10, pp. 2953–2962, Oct. 2003.
- [28] P. Nayeri, “Advanced design methodologies and novel applications of reflectarray antennas,” PhD Dissertation, The University of Mississippi, July 2012.
- [29] R. F. Harrington, *Field Computation by Moment Methods*, Piscataway, NJ: IEEE Press, 1993.
- [30] V. V. S. Prakash and R. Mittra, “Characteristic basis function method: A new technique for efficient solution of method of moments matrix equations,” *Microw. Opt. Technol. Lett.*, vol. 36, no. 2, pp. 95–100, Jan. 2003.

- [31] R. Harrington and J. Mautz, "Theory of characteristic modes for conducting bodies," *IEEE Trans. Antennas Propag.*, vol. 19, no. 5, pp. 622–628, Sep. 1971.
- [32] M. Cabedo-Fabres, E. Antonino-Daviu, A. Valero-Nogueira, and M. Bataller, "The theory of characteristic modes revisited: A contribution to the design of antennas for modern applications," *IEEE Antennas Propag. Mag.*, vol. 49, no. 5, pp. 52–68, Oct. 2007.
- [33] G. Angiulli, G. Amendola, G. Di Massa, "Application of characteristic modes to the analysis of scattering from microstrip antennas," *Journal of Electromagnetic Waves and Applications*, Vol. 14, Iss. 8, 2000.
- [34] HFSS: High Frequency Structure Simulator Based on the Finite Element Method, v.15, Ansys Inc., 2014.
- [35] D. M. Pozar, S. D. Targonski, and H. D. Syrigos, "Design of millimeter wave microstrip reflectarrays," *IEEE Trans. Antennas Propag.*, vol. 45, no. 2, pp. 287–296, 1997.
- [36] A. Alparslan, M. I. Aksun, and K. A. Michalski, "Closed-form green's functions in planar layered media for all ranges and materials," *IEEE Trans. Microw. Theory Tech.*, vol. 58, no. 3, pp. 602–613, Mar. 2010.
- [37] S. Rao, D. Wilton, and A. Glisson, "Electromagnetic scattering by surfaces of arbitrary shape," *IEEE Trans. Antennas Propag.*, vol. 30, no. 3, pp. 409–418, May 1982.
- [38] D. Pozar, "Microstrip reflectarrays: Myths and realities," in *Proc. JINA Int. Symp. on Antennas*, pp. 175–179, Nice, France, Nov. 8–10 2004.
- [39] A. Capozzoli, C. Curcio, A. Liseno, and G. Toso, "Phase only synthesis of aperiodic reflectarrays," *Prog. Electromagn. Res.*, vol. 133, pp. 53–89, 2013.
- [40] C. A. Balanis, *Advanced Engineering Electromagnetics*, John Wiley and Sons, 1989.
- [41] D. Pozar, "Radiation and scattering from a microstrip patch on a uniaxial substrate," *IEEE Trans. Antennas Propag.*, vol. 35, no. 6, pp. 613–621, Jun. 1987.
- [42] W. C. Gibson, *The Method of Moments in Electromagnetics*, Taylor and Francis Group, 2008.

- [43] D. Wilton, S. Rao, A. Glisson, D. Schaubert, O. Al-Bundak, and C. Butler, "Potential integrals for uniform and linear source distributions on polygonal and polyhedral domains," *IEEE Trans. Antennas Propag.*, vol. 32, no. 3, pp. 276–281, Mar. 1984.
- [44] E. Erçil, L. Alatan, Ö. A. Çivi, "Sadece faz ile dizi anteni örüntü sentezi probleminin Newton-Raphson metodu ile çözümü," *URSI Türkiye Bilimsel Kongresi*, Elazığ, Türkiye, 28-30 Ağustos 2014.
- [45] M. Zhou, S. B. Sorensen, P. Meincke, and E. Jorgensen, "Design and optimization of multi-faceted reflectarrays for satellite applications," *The 8th European Conference on Antennas and Propagation*, Hague, Netherlands, 2014.
- [46] M. Zhou, S. B. Sorensen, O. S. Kim, E. Jorgensen, P. Meincke, and O. Breinbjerg, "Direct optimization of printed reflectarrays for contoured beam satellite antenna applications," *IEEE Trans. Antennas Propag.*, vol. 61, no. 4, pp. 1995–2004, Apr. 2013.
- [47] R. Fletcher, "Function minimization by conjugate gradients," *Comput. J.*, vol. 7, no. 2, pp. 149–154, Feb. 1964.
- [48] W. Hagger, H. Zhang, "A survey of nonlinear conjugate gradient methods," *Pacific Journal of Optimization*, vol. 2, pp.35-58, 2006.

CURRICULUM VITAE

PERSONAL INFORMATION

Surname, Name: Erçil, Erdinç

Nationality: Turkish

Date and Place of Birth: 1 February 1981, Ceyhan

Marital Status: Married

Phone: +90 531 7707168

email: eercil@aselsan.com.tr

EDUCATION:

Degree	Institution	Year of Graduation
MS	METU Electrical and Electronics Eng.	2006
BS	METU Electrical and Electronics Eng.	2003

WORK EXPERIENCE:

Year	Place	Enrollment
February 2005-present	ASELSAN Inc.	RF, Microwave and Antenna Design Engineer
September 2003-January 2005	TÜBİTAK UEKAE	Research Engineer

FOREIGN LANGUAGES:

Advanced English, Basic German

PUBLICATIONS

Journal Articles

1. E, Erçil, L. Alatan, Ö. A. Çivi, "An efficient numerical solution method for reflectarrays of varying element sizes," submitted to *IEEE Transactions on Antennas and Propagation* on October 2014.

Conference Papers

1. E. Erçil, L. Alatan, Ö. A. Çivi, "Efficient analysis of reflectarrays through the use of characteristic modes," *9th European Conference on Antennas and Propagation*, Lisbon, Portugal, 12-17 April 2015.
2. E. Erçil, L. Alatan, Ö. A. Çivi, "Fast construction of the MoM matrix for reflectarrays through a smart tabulation," *IEEE International Symposium on Antennas and Propagation and North American Radio Science Meeting*, Vancouver, Canada, 19-25 July 2015.
3. A. Dalkılıç, C. Bayram, C. B. Top, E. Erçil, "Slotted waveguide array beamformer characterization using integrated calibration channel," *Antenna Measurement Techniques Association 36th Annual Meeting and Symposium*, Tuscon, Arizona, 12-17 Oct 2014.
4. E. Erçil, L. Alatan, Ö. A. Çivi, "Sadece faz ile sentez probleminin Newton-Raphson methodu ile çözümü," *URSI Türkiye VII. Bilimsel Kongresi*, Elazığ, Türkiye, 28-30 Ağustos 2014.
5. E. Erçil, L. Alatan, Ö. A. Çivi, "Farkli tip karakteristik modların büyük anten dizilerinin nümerik çözümünde kullanımının karşılaştırılması," *URSI Türkiye VI. Bilimsel Kongresi*, İstanbul, Türkiye, 2-5 Eylül 2012.
6. K. Tap, D. Tekbaş, E. Erçil, S. Köksoy, "Uzay uygulaması için geliştirilen aktif fazlı dizi beslemeli reflektör antenin tasarım, entegrasyon ve doğrulama yaklaşımı," *URSI Türkiye VI. Bilimsel Kongresi*, İstanbul, Türkiye, 2-5 Eylül 2012.
7. E. Yıldırım, E. Erçil, D. Doğan, "L-Bant silindirik dizi anten çalışmaları," *URSI Türkiye VI. Bilimsel Kongresi*, İstanbul, Türkiye, 2-5 Eylül 2012.
8. A. Dalkılıç, E. Erçil, "Fazlı Anten Dizilerinde Sadece Faz ile Sentez Uygulamaları," *URSI Türkiye VI. Bilimsel Kongresi*, İstanbul, Türkiye, 2-5 Eylül 2012.
9. E. Erçil, "An alternative method for phase-only array pattern synthesis," *IEEE International Symposium on Antennas and Propagation*, Chicago, Illinois, 8-14 July 2012.

10. E. Erçil, E. Yıldırım, and M. E. İnal, "Array antenna pattern synthesis using measured active element patterns and Gram-Schmidt orthogonalization," *Phased Array Syst. Technol. (ARRAY), 2010 IEEE Int. Symp.*, 2010.
11. Erçil, E., "Fazlı anten dizilerinde sadece faz ile sentez problemine yeni bir bakış," *URSI TÜRKİYE V. Bilimsel Kongresi 2010*, Güzelyurt, KKTC, 25-27 Ağustos 2010.
12. E, Erçil, Ş. Demir, M. E. İnal, "X – bant tek tabanlı mikrodalga entege devre (MMIC) 7 bit faz kaydırıcı tasarımı," *URSI Türkiye III. Bilimsel Kongresi*, Ankara, Türkiye, 6-8 Eylül 2006.